Droplet spreading and imbibition on microporous membranes

by

Debanik Bhattacharjee

A thesis submitted in partial fulfillment of the requirements for the degree of

Master of Science

Department of Mechanical Engineering
University of Alberta

Abstract

The phenomena of droplet spreading and imbibition has widespread application in membrane science. It is widely believed that the membrane flux increases with greater hydrophilicity. In porous membranes, the spreading and permeation occur at the same time, and these separate but competitive phenomena must be considered when reporting the contact angle results. In the first phase, the role of characteristic parameters (radius and height of droplet) is investigated by considering an existing mathematical model formulated on the basis of lubrication approximation. Under partial wetting conditions, the contact line singularity prevails which is relieved using precursor film assumption and disjoining pressure. Based on two main stages of spreading (initial and equilibrium), characteristic radius and height were first evaluated. The model predictions were then compared with experimental results in literature for both impermeable and permeable substrates. It was found that the choice of characteristic length scales based on either stage enables accurate prediction of the droplet base radius and contact angle. A new scaling relation for the prediction of the numerical disjoining pressure for both impermeable and permeable wetting systems, with an error of $\pm 5\%$, is proposed.

In the second part, experimental and numerical study of water droplet spread-

ing and imbition on lab-fabricated and commercial polyethersulfone (PES) membranes is performed. The characterization technique used for permeability is filtration test, for cross-section thickness is FESEM images, for surface roughness is AFM data, and for hydrophilicity is dynamic contact angle experiments. The theoretical disjoining pressure calculated in the case of apolar and polar interactions is found to be related to the numerical disjoining pressure parameter obtained after good agreement with experiments. The pinning observed in the contact angle experiments is well predicted by the mathematical model used in the first phase of the study. The hydrodynamic permeability of a membrane as a function of its cross-section thickness and resistance is compared to the effective permeability which is calculated after validating numerical predictions with contact angle experiments. An attempt has been made to correlate the local property realized through droplet dynamics to its global property interpreted through resistance of the membrane.

Preface

This thesis highlights the numerical and experimental investigation of droplet spreading and imbibition on microporous membranes.

Chapter 2 of the thesis titled "Droplet spreading and imbibition: Role of characteristic length scales and modified disjoining pressure" served as the topic of an oral presentation at the *70th Annual Meeting of the APS Division of Fluid Dynamics, 2017*.

Chapter 3 titled "An experimental and numerical study of droplet spreading and imbibition on microporous membranes" has been prepared for submission to *Physical Review Fluids*. Part of this chapter was also presented as a poster at the *Complex Motion in Fluids Summer School, DAMTP, University of Cambridge, 2017* and as an oral presentation at the *70th Annual Meeting of the APS Division of Fluid Dynamics, 2017*.

To my parents and grandparents
for their unconditional support

Acknowledgements

Contents

List of Tables

List of Figures

Nomenclature

V Droplet volume

r Droplet radius at later time

R Initial droplet radius

W Work of adhesion

S Spreading coefficient

Ca Capillary Number

B Bond Number

R_m Intrinsic resistance of membrane

d Thickness of substrate

h Droplet height

F Young's forces

p Pressure

$r-$ Radial direction in cylindrical coordinates

$z-$ Vertical direction in cylindrical coordinates

u Velocity in the r-direction

w Velocity in the z-direction

$\hat{\mathbf{n}}$ Unit vector normal to the liquid-vapor interface

$\hat{\mathbf{t}}$ Unit vector tangential to the liquid-vapor interface

H Curvature

A Disjoining pressure parameter

b Precursor film thickness

J Flux

Greek Letters

σ Interfacial tension

θ Contact angle

μ Dynamic viscosity

κ Effective permeability

ϵ Lubrication ratio

ϕ Energy per unit volume

Π Disjoining pressure

Subscript

0 Initial value

S Solid

L Liquid

V Vapor

cap Capillary

app Apparent

CB Cassie-Baxter

W Wenzel

adv Advancing

rec Receding

eq Equilibrium

sc Scale

Abbreviations

DAE   Differential Algebraic Equation

SLATEC Sandia, Los Alamos, Air Force Weapons Laboratory Technical Exchange Committee

FESEM Field Emission Scanning Electron Microscope

AFM   Atomic Force Microscope

PES   Polyethersulfone

PVP   Polyvinylpyrrolidone

LW   Lifshitz-van der Waals'

P   Polar

Chapter 1

Introduction

1.1 Overview

Wettability lies at the heart of many industrial processes like spray technology, inkjet printing, soldering of alloys and membrane filtration. A droplet spreading on a solid substrate is a well defined characteristic of wettability. For permeable substrates, the phenomenon is more complex because of interaction of the invading fluid with the pores at different length scales. The extent of spreading is usually characterized by the contact angle. The degree to which a substrate is wettable depends on the nature of the liquid, the surface energetics and physico-chemical heterogeneities. A liquid-substrate combination may be either completely or partially wetting. For a completely wetting system, the contact angle is 0° and a thin film of liquid is formed on the substrate. However, for partially wetting systems, the liquid is in a metastable state with a finite contact angle ranging between 0° and 180°. The tri-phase contact line arising because of partial wetting conditions is commonly studied using hydrodynamical approach. The transition from partial to complete wetting is categorized into first, second, third and infinite order, with a functional defined on the principle of free surface energy minimization. The wetting transition is beyond the scope of the present thesis. The focus of the thesis is the numerical and experimental investigation of droplet dynamics (spreading and imbibition) on permeable substrates with partial wettability.

1.2 Motivation

Membranes are permeable substrates which find application in separation of micro-organisms, suspended matter, desalination and wastewater treatment.

Membrane processes can be categorized on the basis of driving force of transport into: (i) pressure-driven, (ii) concentration-driven, (iii) electrical-driven, and (iv) temperature-driven processes. Pressure-driven membrane filtration can be further classified on the basis of average pore size of the applied membranes membranes into: (i) Nanofiltration (NF) which involves membranes with average pore size between 0.001 μm and 0.01 μm, (ii) Ultrafiltration (UF) includes membranes with average pore size between 0.01 μm and 0.1 μm, and (iii) Microfiltration (MF) includes membranes with average pore size between 0.1 μm and 10 μm. Membranes are usually characterized for permeability by flux test, hydrophilicity by contact angle measurement, surface and cross-sectional morphology by scanning electron microscopy (SEM), and roughness by atomic force microscopy (AFM). The primary goal of the membrane development process is to maximize flux without compromising separation of targeted contaminants like salt, organic matter, and biological substances. To achieve this goal, flux tests are performed either using cross-flow setup or dead-end filtration systems. These setups require huge monetary investment and the flux tests are very time consuming as well. Flux tests are performed by applying varying amounts of transmembrane pressure. The obtained flux is plotted as a function of transmembrane pressures and the slope of this curve yields the hydrodynamic resistance of the membrane. The present thesis is aimed at understanding the hydrodynamics of membrane filtration by droplet dynamics. An attempt is made to relate the intrinsic properties of MF membranes (both lab-fabricated and commercial) such as resistance and roughness to the macroscopic phenomenon of droplet spreading and imbibition on a permeable substrate. This will provide insight regarding the correlation of global quantity (hydrodynamic permeability by means of membrane hydrodynamic resistance and thickness) to that of a local one (effective permeability by means of droplet imbibition).

1.3   Theory

1.3.1   Wettability

The phenomenon of wetting has widespread applications in our lives and in the technology that shapes our lives. The everyday experience of washing hands and taking bath with water is the simplest example of wetting. Our skin does not seem to prefer water but instead, likes to repel it [5]. This repulsive be-

haviour of a surface with respect to water is termed as hydrophobicity. If the surface is fond of liquid, it would allow the liquid to occupy greater surface area for longer time. This attractive behaviour is termed as hydrophilicity. The importance of wetting can be understood in different size regimes. The application of spray technology in design of efficient solar cells [6], the printing technology which will help us to have a hard copy of this thesis [7], the advent of superhydrophobic coatings for anti-icing during extreme cold [8] and oil versus water preference in oil recovery [9] are some of the well known technologies which utilise the fundamentals of wetting.

Wetting can be classified into two categories: non-reactive and reactive wetting systems. A non-reactive wetting system is described by a liquid on a solid with no reaction/absorption. A reactive wetting system includes reaction/absorption of the liquid by the substrate at many length scales. Wetting is usually characterized by contact angle which is formed at the interface between the solid and the liquid.

Consider a liquid droplet spreading on a ideally smooth, chemically homogeneous solid substrate (Fig. 1.2). . At thermodynamic equilibrium, the interfacial tensions balance each other and this gives rise to the well known Young's equation [10].

$$\sigma_{SV} - \sigma_{SL} = \sigma_{LV} cos\theta_{eq} \qquad (1.1)$$

where the σ_{xy} denotes the interfacial tension of state 'x' with respect to state 'y'. The letters S, L, and V refers to solid, liquid, and vapor, respectively. The equilibrium contact angle between the solid and the liquid interface is given by θ_{eq}. The work of adhesion between a solid and a liquid is given by:

$$W_{SL} = \sigma_{SV} + \sigma_{LV} - \sigma_{SL} \qquad (1.2)$$

Substituting eqn. (1.1) in (1.2), we get

$$W_{SL} = \sigma_{LV}(1 + cos\theta_{eq}) \qquad (1.3)$$

This is the classical Young-Dupré equation [11].
For small contact angles, Young's equation is not valid. As a result, wettability

is defined by the spreading coefficient, S arising out of imbalance of surface energies.

$$S = \sigma_{SV} - (\sigma_{SL} + \sigma_{LV}) = \sigma_{LV}(cos\theta_{eq} - 1) \qquad (1.4)$$

A liquid droplet placed on a solid substrate has two possibilities (Fig. 1.1).
(i) The droplet may spread completely on the solid to form a macroscopically thick wetting layer. The equilibrium contact angle is $0°(S < 0)$ and the liquid-solid combination is described as a completely wetting system.
(ii) The droplet may not spread completely on the solid. Instead a thin microscopic wetting layer is adsorbed on the substrate. Such liquid-solid combination is a characteristic of partially wetting systems with equilibrium contact angle between $0°$ and $180°$ $(S \geq 0)$.

The extent of wetting of the solid depends on its nature [12]. For the same liquid, a high-energy solid surface will have greater affinity for the liquid than a low-energy surface. A high-energy surface includes hard solids held together by metallic, covalent or ionic bonds. On the other hand, a low-energy surface is described by molecular solids bound by van der Waals' forces and hydrogen bonds.

1.3.2   Spreading

The phenomenon of spreading on solid substrates is the fundamental characteristic of wettability which can be broadly classified into two categories: spontaneous and forced spreading. Spontaneous spreading is initiated by the action of capillary forces and does not involve the action of gravity. A droplet deposited with a needle on a substrate under the influence of surface interaction is a classic example of spontaneous spreading. The wetting front propagation of a spontaneously spreading macroscopic droplet is preceded by a precursor film [13] (thickness of the film between 10 nm and 1 μm). The characteristics of the precursor film are discussed in later section. On the other hand, forced spreading is often defined by the significant role gravity plays in the process. When a droplet impacts a surface with a very high Weber number, it is difficult to decouple the effect of gravity from capillarity. The driving force of forced spreading is a combined action of gravitational and capillary forces.

Spreading is characterized by the contact angle which is the slope of the solid-liquid interface on the solid. Equilibrium contact angle is defined by Young's condition (eqn. 1.1) which is applicable when the droplet ceases to spread. Young's condition is valid for smooth, isotropic, physically and chemically inert and non-deformable substrates. For real substrates, the equilibrium condition is defined by the apparent contact angle. Almost all the contact angle calculated experimentally can be deemed to be quasi-equilibrium in nature.

A small viscous droplet spreads on a surface and wets it completely. If the droplet radius is smaller than the capillary length, l_{cap} $(=\sqrt{\frac{\sigma}{\rho g}})$, the effect of gravity is negligible. In this case, the droplet assumes a spherical cap on the surface. The capillary number, Ca which is defined as the ratio of viscous to surface tension forces, is of the order of $10^{-5}-10^{-3}$. For thin droplets, the droplet height $h(r,t)$ is given by

$$h(r) = \frac{2V}{\pi R^2}\left[1 - (\frac{r}{R})^2\right] \tag{1.5}$$

The apparent contact angle, θ_{app} is described by

$$\theta_{app} = \frac{4V}{\pi R^3} \tag{1.6}$$

The universal Tanner's law [4] predicts the viscous droplet radius as a function of time.

$$R(t) \propto t^n \tag{1.7}$$

The power n has been found to be approximately 0.1 and this result has been confirmed previously through many experiments [4, 14].

1.3.3 Imbibition

Imbibition of liquid by a porous substrate results in the increase of its volume because the pores get saturated with the liquid. This phenomenon falls in the category of reactive wetting which can be classified into drainage and imbibition. The nature of these processes depends on the wettability of the systems. Drainage refers to the case where the invading fluid is less wetting to the solid

surface than the defending fluid. Imbibition is opposite, in the sense that it is more wetting to the solid surface than the defending fluid [15].

For a droplet on a porous substrate, little attention is paid to the physics of imbibition. In general, droplet imbibition is assumed to be the case. However, the phenomenon involves complex interplay of both the processes, beginning with the slow drainage of the precursor film, followed by the rupture of the film due to strong curvature effect and the formation of the neck leading to imbibition. For the sake of brevity, droplet imbibition is considered in the present thesis.

The process of droplet imbibition on a saturated porous substrate can be understood as a two-stage process [16]: (i) the spreading of the droplet over the saturated porous layer. This involves expansion of the droplet base until a maximum followed by (ii) imbibition which causes the droplet to entrain into the porous substrate. This is characterized by the complete shrinkage of the droplet base.

1.3.4 Contact Angle Hysteresis

In reality, all solids are heterogeneous in nature. The heterogeneities which might be physical (roughness) or chemical (contaminants) in nature, causes the contact line to behave asymmetrically. This asymmetric behaviour of the contact line is manifested in the contact angle prediction termed as advancing (θ_{adv}) and receding angles (θ_{rec}). The existence of multiple contact angles is called hysteresis. The focus of the present thesis is the hysteresis as a result of physical effects i.e. surface defects or roughness. The size of the defects (micrometric or nanometric) causes the macroscopic pinning behaviour which is characterized by constant radius regime.

Young's relation may still hold for small defects, provided S is replaced by its average value, $\bar{S}$. This results in the Cassie-Baxter relation [17]:

$$\sigma(1 - cos\theta_{CB}) = -\bar{S} \tag{1.8}$$

Such a relation only holds at the thermodynamic equilibrium. A surface is considered relatively homogeneous if the contact angle hysteresis, $\Delta\theta$ (=

$\theta_{adv} - \theta_{rec}$) is less than 5° [18]. Hysteresis can be interpreted on the basis of forces acting at the tri-phase contact line. The threshold force per unit length necessary to make the contact line advance or recede follows from the unbalanced Young's forces:

$$F_{adv} = \sigma(cos\theta_{eq} - cos\theta_{adv}); F_{rec} = \sigma(cos\theta_{rec} - cos\theta_{eq}) \qquad (1.9)$$

The hysteresis force per unit length may be defined as

$$F = \sigma(cos\theta_{rec} - cos\theta_{adv}) \qquad (1.10)$$

For most wetting systems, $\frac{F}{\sigma} \geq 0.1$ which implies that the receding contact angle is zero and the contact line cannot recede until the advancing contact angle is less than 20°.

For structured surfaces, energy minimization leads to an effective equilibrium contact angle, θ_W. This is the well known Wenzel relation [19].

$$cos\theta_W = rcos\theta_{eq} \qquad (1.11)$$

where r is the ratio of the real to the projected area covered by the drop. This relation is valid when the hysteresis is small.

In the case of complete wetting, the mechanism of the spreading droplet in the presence of roughness can be described as a two-stage process [20]. The first stage involves natural spreading without the effect of roughness. This is because the contact angle is high for the roughness to play a significant role. The second stage is realized when the contact angle decreases to a small value and the spatial impact of roughness is perceived by the droplet. The propagation of the macroscopic droplet wetting front is preceded by a thin precursor film which fills the surface defects. Some authors have argued the simultaneous spreading of the droplet and thin film formation causing the defects to be smoothened [21, 22].

In the case of partial wetting, the spreading mechanism significantly depends on the nature of defects which might be mesoscopic (micrometric) or microscopic (nanometric). In the presence of mesoscopic heterogeneities, the contact line is distorted which is governed by the balance between surface tension forces

and pinning forces due to defect strength. The energy dissipation mechanism due to surface defects has been interpreted to be viscous dissipation due to shear flow near the wedge [18]. Many authors have tackled the depinning dynamics in the presence of a single defect by calculating the deformation of the contact line as a function of depinning and external force [23, 24]. In addition, attempts have been made to understand the dynamics due to weak and strong interacting defects but there is still debate in the community regarding the dissipation mechanisms [25–28].

For microscopic heterogeneities, the pinning effect is often attributed to the liquid surface fluctuations arising out of thermal noise [29]. In some studies, the maximum contact line velocity has been found to be independent of fluid viscosity. This indicates that viscous dissipation is not the only mechanism at play but the molecular motions at the contact line have an important role [25, 30]. Several studies have focused on the contact line dynamics close to the depinning threshold using molecular kinetic theory [31, 32]. These report the pinning energies to be of the same order of magnitude as the thermal energy.

1.3.5   Huh and Scriven's paradox

"Not even Herakles could sink a solid if the physical model (no-slip) were entirely valid."

This aphorism in the seminal work of Huh et al. [33] succinctly stated the failure of classical hydrodynamics in predicting the moving tri-phase contact line problem. The well known 'no-slip' condition at the interface between solid and liquid is given by:

$$u_L.\mathbf{t} = u_S.\mathbf{t} \tag{1.12}$$

where $\mathbf{t}$, u_L, and u_S represents the tangent vector at the solid, velocity in the fluid, and velocity at the solid, respectively. The classical perception is that if slippage happens between two media, this will give rise to stress. This stress will cause the two velocities to equilibrate which was understood by the concept of momentum dissipation. The classical continuum theory invokes the no-slip condition.

The creeping flow model in the lubrication limit was proven to have singular solutions at the moving contact line [33]. The singularity influenced shear stresses, pressure, and viscous dissipation rate wherein these quantities di-

verged in the neighborhood of the contact line. The possible flaws in the assumption which led to singularity were no-slip condition, cavitation arising out of pressure plunge and viscous dissipation, steep gradients of viscosity and density as well as compressibility effects. The corner flow in the fluid led to the interpretation that the long-range intermolecular forces might be responsible for this divergent behavior. The breakdown of continuum model was due to the existence of molecular dimensions which the classical theory failed to account for. Later, Hervet et al. [13] proposed a mathematical approach to account for the contribution of intermolecular forces. This was realized by the notion of precursor film with the interactions governed by competing mechanisms of repulsive, stabilizing, short-ranged and attractive, destabilizing, long-ranged forces (Fig. 1.3).

1.4   Modelling the contact line problem

The moving contact problem has received considerable attention since the 1970s. The field of droplet dynamics and capillarity rely solely on the behavior at interfaces which is governed by the contact line dynamics. As discussed in the previous section, the imbalance of capillary and viscous forces leads to singularity which makes it difficult to study the dynamic nature of these physical problems. The classical hydrodynamics in the neighborhood of the contact line makes strange predictions which is not grounded in real observations.

Table 1.1 summarizes a number of physical mechanisms which have been proposed in order to relieve the stress singularity at the contact line. In this thesis, the contact line physics is understood by assuming the existence of a precursor film ahead of the macroscopic droplet edge [13]. This is essentially a mesoscopic approach which bridges the macroscopic region of the droplet (where classical hydrodynamics is still valid) to the microscopic contact line region through short and long-range intermolecular forces.

Mechanism	Reference
Navier slip	Huh et al. [33]
Nonlinear slip	Thompson et al. [34]
Generalized Navier slip	Shikhmurzaev [35]
Surface roughness	Hocking [36]
Evaporation and condensation	Wayner [37]
Precursor film	Hervet et al. [13]
Shear thinning	Gorodtsov [38]
Diffuse interface	Seppecher [39]
Molecular film	Eres et al. [40]
Normal stresses	Boudaoud [41]

Table 1.1: The different physical mechanisms which have been employed to relieve the stress singularity at the contact line.

1.4.1 Precursor film

The focus in this section is the occurrence of precursor films for non-volatile droplets spreading at mesoscopic scales. The mesoscopic approach ensures the validity of classical hydrodynamics and also considers the effect of intermolecular forces.

A mesoscopic precursor film of thickness between 10 nm and 1 μm protrudes out of the macroscopic droplet edge. The necessary and sufficient conditions for the origin of such films is debated to this day [42]. The first reported obervation of the existence of an "invisible film" was done by Hardy [43] when he studied the behavior of drops of water, acetic acid and other polar organic liquids on clean surfaces of glass and steel. Due to the primitive optical techniques of the time, Hardy could not photograph the formation of the film but instead observed the drop in static friction of the surface near the tri-phase contact line. He explained the occurrence of the film on the basis of steady condensation of vapor. Later, the existence of the film was found even in the absence of vapor while studying spreading behavior of polar and apolar liquids on freshly cleaved mica [44].

The revolution in optical technology further strengthened the possibility of experimental detection of a precursor film. The first quantitative study using ellipsiometry and interferometry was performed by Bascom et al. [45] in which the spreading behavior of various hydrocarbons on clean, horizontal and ver-

tical metal surfaces was investigated. The existence of the film in the presence of either vapor saturated or unsaturated with air cemented the previous idea that surface diffusion of molecules was responsible. Using Scanning Electron microscopy to study the spreading of an inorganic molten glass on Fe-Ni-Co alloy quantified the thickness of the film of the order of one micron [46].

At mesoscale, the hydrodynamics is important along with the effect of intermolecular forces. The idea of free energy to account for the interactions between interfaces was first proposed by Derjaguin et al. [47]. This was introduced in the form of effective interface potential, $\omega(h)$ which has a pressure term, usually referred as the disjoining pressure $\Pi(h) = \frac{\partial \omega}{\partial h}$. When considering the spreading of a thin, non-evaporating liquid film on a solid surface, the theoretical analysis predicts the emergence of a an "adiabatic film" from the liquid wedge which is moving at a constant velocity [48]. With van der Waals' disjoining pressure $\Pi(h) = -\frac{A}{6\pi h^3}$, the thickness of the adiabatic film was found to be directly proportional to S. Thus, the macroscopic region of the droplet is independent of the spreading coefficient but the mesoscopic region is dependent. The adiabatic film is valid only for a few micrometers. The gradient of the disjoining pressure causes a non-stationary film termed "diffusive film" to propagate ahead of the adiabatic film. When the diffusive length becomes much larger than the adiabatic length, the diffusive length was found to be proportional to square root of time. The structure of the precursor film is depicted in Fig. 1.4.

1.5   Literature Review

Cazabat [49] reviewed the theoretical and experimental studies in support of the macroscopic and microscopic mechanisms involved in the spreading of a droplet. The macroscopic description describes partial wetting which corresponds to a finite contact angle and complete wetting when the contact angle goes to zero at equilibrium. In 'moist' wetting, the droplet is in equilibrium with the vapor of the liquid. In some cases, a film is adsorbed on the solid surface which can lead to complete wetting. In 'dry' wetting, the vapor pressure of the liquid is negligible which does not cause the molecules to condense on the solid surface. As a result, there is no occurrence of a liquid film which indicates partial wetting. The inconsistencies arising in different wetting sce-

narios especially the universal laws paved way for microscopic description. The microscopic description is understood by the presence of a thin film preceding a spreading droplet (precursor film). These films are governed by van der Waals' forces. In moist conditions, the thickness of the adsorbed film is much larger than precursor film thickness. However, in dry conditions, a thin film is squeezed out of the balance between capillary forces and disjoining pressure. The dynamics of dry wetting is explored in detail in this section.

Ausserre et al. [50] conducted first systematic study to establish the existence of precursor film and the spreading coefficient, S independence of the spreading kinetics by aid of optical techniques. The authors picked high molecular weight nonvolatile polydimethylsiloxane (PDMS) droplets which was deposited on high-energy (ultraclean wafer) and low-energy surface (chemical grafting of octadecyltrichlorosilane). A nonvolatile liquid does not allow the molecules to be transported efficiently from the liquid to the solid through the vapor phase. As a result, the liquid molecules do not condense on the surface. This ensures a finite S across all times. For the macroscopic region of the droplet, the size and apparent contact angle was found to obey Tanner's law which is independent of S. In the microscopic region which was characterized by the direct visualization of the precursor film, the growth kinetics and the structure was found to strongly depend on S. Later, Leger et al. [51] undertook precursor film profile determination using spatially resolved ellipsiometry for large S. The film thickness was found to increase for smaller apparent contact angle and decayed to zero. The film evolved under the action of Laplace and disjoining pressure gradients. However, the formulated model in this case failed to accurately predict the experimental profiles. The authors hypothesized inappropriate modelling of driving forces and the improper choice of viscosity. The growth kinetics of the film was observed to be much faster than the model prediction for larger molecular weight of PDMS. Kavehpour et al. [52] studied the spreading of viscous nonvolatile liquids on smooth horizontal substrates using interference microscopy. The goal was to understand the structure of the macroscopic outer region and microscopic inner region in the precursor film as suggested by the inflection point in the solution of the governing equation. The apparent contact angle was obtained from experimental fit as a function of the capillary number and logarithmic dependence of the matching length between the inner microscopic and outer macroscopic region. The macroscopic dynamic (or apparent) contact angle is usually defined as the maximum slope

of the interface.

Ruijter et al. [53] studied the sessile liquid droplet spreading on an ideal solid surface under partial wetting conditions. The problem was studied from the standpoint of dissipation due to viscous flows and due to friction in the vicinity of the contact line. The standard approach is to equate the gradient of the system's Lagrangian function to the rate of total dissipation. The driving force is the loss of free energy of the droplet due to increasing base radius. The dominant effect of one dissipation channel over the other was explained by the evolution of the droplet radius in three different regimes. The early-time stage was characterized by linear time-dependence of the base radius, an intermediate-time stage where the nonhydrodynamic dissipation prevailed and the base radius was found to be in close agreement with the prediction of molecular kinetic theory, and lastly, long-time stage where the hydrodynamic dissipation was dominant and the base radius evolved exponentially over time. The authors also reported the cross-over time between the two modes of dissipation and found it to be large for liquids with low viscosity or solids with high friction coefficients. This provides insight on the role of hydrodynamics at longer time scales.

Eggers et al. [54] performed theoretical and experimental investigation to quantify the characteristic length scales near the contact line for perfectly wetting fluid. The authors explained the logarithmic correction in capillary number to the Tanner's law using models based on precursor film and slip in the lubrication limit. The conclusion was drawn that the cut-off length scale for relieving contact line singularity was dependent on the contact line speed. The authors fail to provide explanation of the different length scale as a function of finite contact angle obtained using slip and precursor film model where van der Waals' forces are dominant. For partially wetting fluids, the prediction of cut-off length is comparatively easier for each model.

Savva et al. [55] performed a comparative study between slip and precursor film models for the contact line motion of spreading of a thin two-dimensional, partially wetting droplet. A nonlinear PDE was obtained for both slip conditions and precursor film assumption. The authors investigated the quasistatic limit of the spreading dynamics via matched asymptotics. The standard procedure is to compare the solution in the bulk of the droplet (outer region) to the solution in the vicinity of the contact line (inner region). An equivalence relation was successfully established between the two models in the quasistatic

limit. Later, the nonlinear PDEs were solved numerically using pseudospectral method. The dynamics of the contact line was indistinguishable on a flat substrate using both solution techniques for slip and precursor film models. On a heterogeneous substrate, the significant differences between the two models were explained by phase plane analysis where the droplet attained different equilibria. In the absence of quasistatic limit which was achieved by considering a vibrating flat horizontal substrate, the authors observed indistingushable dynamics for both the models using full PDEs. Thus, the only advantage precursor film model has is that the contact line need not be tracked each step of the way, instead the apparent contact line is defined by the thickness of the film.

Glasner [56] investigated the spreading of two-dimensional and axi-symmetric droplets under the influence of short and long range intermolecular forces. In the quasistatic regime, the scaling law was found to coincide with Tanner's prediction [4] with weak dependence on the geometry of the droplet. The numerical solution of the governing thin film equation was found to be in agreement with the asymptotic prediction of global energy minimization functional at the equilibrium stage. However, the author does not consider the effect of substrate heterogeneity in the scaling law. The nature of surface roughness can influence the contact line motion.

Davis et al. [57, 58] analyzed model problems pertaining to two-dimensional droplet spreading and imbibition on a permeable substrate. The authors considered a number of scenarios: completely wetting, dry, saturated and partially wetted porous layer. In each case, a nonlinear evolution equation was obtained by using lubrication approximation. The evolution equations were solved by asymptotic approach and self-similarity. For the dry porous layer, the authors included an effective slip condition at the contact line to relieve the stress singularity. Darcy's law governed imbibition in unconnected vertical pores of fixed thickness on the permeable substrate. The authors reported the non-existence of a universal behavior of the contact line velocity as a function of the apparent contact angle for permeable substrates, similar to Tanner's law [4]. The models considered in this study present an ideal case of porous nature of substrates far from reality. Permeable substrates have a diverse porous structure which makes the flow behavior complicated to study.

Alleborn et al. [59] considered the two- and three-dimensional spreading and imbibition of droplets and thin films into an infinitely thick porous substrate.

The lubrication approximation enabled the derivation of an evolution equation for the droplet profile above the porous substrate and the profile of the wetting front inside the porous substrate. The contact line region was described by the precursor film and disjoining pressure in the frame of Frumkin-Deryaguin model. The flow in the saturated part of the porous substrate was governed by Darcy's law. For the imbibition of a sessile droplet into a porous substrate, the authors established the mechanism of the receding contact line with an apparent contact angle in close proximity to the equilibrium value. This is an intermediate position in the imbibition model assuming a receding contact line between a constant and variable apparent contact angle. For the coupled case of spreading and imbibition, the authors observed that the droplet reached its maximum extent before the contact line started to recede. The authors have hinted on the role of anisotropy affecting the imbibition kinetics but not specifically its impact on the fixed apparent contact angle for larger times.

Ajaev [60] studied the axi-symmetric spreading of a volatile liquid droplet on uniformly heated solid surface. For partial wetting conditions, the contact line is modelled using a microscopically adsorbed film usually referred to as precursor film. A single nonlinear partial differential equation (PDE) tracking the droplet interface was obtained using lubrication-based approach. The author observed competing mechanism of evaporation and capillarity in driving spreading at the latter stages. The contact line pinning dynamics due to evaporation characterized by constant apparent contact angle was well captured by the model. Not much attention is paid in understanding the constant radius mode of evaporation which has been shown to cause pinning on solid substrates.

Zadrazil et al. [61] investigated the spreading, imbibition and solidification dynamics of polyethylene glycol (PEG) melts on porous tablets made of anhydrous sodium carbonate, experimentally and numerically. A commercial instrument, DSA-10 (Kruss GmbH) was used for recording droplet behaviour and sessile droplet technique was utilised for obtaining dynamic radius and contact angle. The flow within the two-dimensional droplet is governed by Navier-Stokes and energy conservation equations in the lubrication limit, with the singularity relieved by precursor film theory. The flow within the porous medium is treated to be Poiseuille type with clear distinction between solidified and fluid phases. Pores are treated to be long, thin and partially saturated with the same liquid as the droplet. A single compact PDE coupling the droplet and

the imbibition interface is obtained. The mathematical model made excellent dynamic radius and contact angle predictions when compared with experimental data. The study assumes uniform porosity and one-dimensional nature of flow in the porous medium which is an ideal case. In addition, contact line pinning observed in the dynamic measurements have not been explained. The pinning nature could be due to irregular pore distribution or the mode of solidification.

Gomba et al. [62] focused on the thermocapillary migration of two-dimensional droplets of partially wetting liquids on non-uniformly heated substrate. The lubrication theory was used to derive an equation to account for the droplet height. The non-zero contact angle was achieved by a finite disjoining pressure term. For small contact angles, the linear increase of the droplet width was attributed to the presence of Marangoni stresses which dominated the effect of disjoining pressure. For larger contact angle, the droplet speed was found to be directly proportional to the temperature gradient and inversely proportional to the viscosity. It was also found that the speed had a linear dependence with radius. The authors assert that the dependence with radius varies with the nature of the fluid. The apparent contact angles at the leading and the rear front was found to have strong relationship with temperature gradient. The contact angle hysteresis was predominant for a very large temperature gradient. The transition regime between small and large contact angles involves complex competing mechanisms between Marangoni and disjoining effects. The authors do not comment on the possibility of contact line pinning based on temperature gradient. For a range of contact angles, it should be possible to observe pinning effect where the values at both ends remain frozen for a time period dictated by the temperature gradient.

Espin et al. [63] developed a lubrication-based mathematical model to understand the phenomena of axi-symmetric droplet spreading and imbibition on permeable substrates. The contact line singularity is relieved using precursor film assumption and disjoining pressure. The imbibition condition is a simplified Darcy's formulation which removes the need for thickness-dependent permeability [57, 58]. Substrate heterogeneity is accounted for by considering an isolated defect in the form of a Gaussian. The model successfully captures the contact line pinning dynamics observed in previously reported experiments. The effective permeability was calculated using scaling factors and the values were in the range reported in the literature. The shortcoming

is that the formulation does not consider the pore size distribution which is a signature of permeable substrates. Different pore sizes can significantly alter the flow behavior which can be seen in the movement of the imbibition front. Wang et al. [2] considered the spreading and imbibition of water droplet on alkaline hydrolyzed melt-blown poly(butylene terephthalate) (PBT) fiber mats. Surface treatment through hydrolysis significantly transformed the wetting properties of the fiber mats and converted them to superhydrophilic. Longer etching times resulted in the loss of fiber-mat capillaries which caused longer imbibition times. This suggests a delicate balance between the time-scales necessary to achieve superhydrophilicity by means of surface treatment. The contact line pinning observed in the dynamic contact angle experiments was captured by the mathematical model [63] in the presence of an isolated defect. The effective permeability was also calculated and found to be in close agreement with the experimental values based on Darcy's law which relates the flow rate as a function of applied pressure. However, no effort is made to correlate the pinning dynamics to the actual size of a defect. The pinning dynamics is expected to differ depending on the strength of a defect and in some cases, for slower imbibition, on the interaction with multiple defects.

1.6 Objectives

The primary goals of this thesis are (i) to understand the role of characteristic parameters in the numerical prediction of dynamic droplet radius and contact angle and (ii) to investigate the phenomena of droplet spreading and imbibition on lab-synthesized pressure-driven microfiltration membranes and commercial track-etched membranes. This was achieved by performing numerical and experimental studies. The research was conducted in two phases as discussed below:

- In the first phase, the role of characteristic parameters (radius and height of droplet) was investigated by using a lubrication-based mathematical model formulated on the basis of precursor film approximation and disjoining pressure. A modified scaling relation for disjoining pressure is proposed which enables the prediction of equilibrium stage with $\pm 5\%$ error.

- In the second phase, droplet dynamics was studied by performing experiments on lab-fabricated and commercial PES membranes. The intrinsic

properties of the membranes was linked to the phenomena of droplet spreading and imbibition. The disjoining pressure was estimated using a theoretical approach and found to have a close match with the numerical prediction. Effective permeability of a membrane was calculated by means of lubrication-based mathematical model and dynamic contact angle measurements whereas hydrodynamic permeability was calculated by the cross-section thickness and the resistance of a membrane. Then, a comparison was made between the two permeabilities.

1.7   Thesis Organization

Chapter 1 lays out the overview along with the primary motivation of the thesis. The concept of wettability is introduced with broad range of applications. The phenomenon of spreading on a solid substrate which is the fundamental characteristic of wettabiity, is discussed in detail along with imbibition in a porous substrate. Since all real solids are heterogeneous in nature, the measured contact angle is not uniform. This non-uniformity of contact angle is understood in terms of hysteresis with either partial or complete wetting conditions. Huh and Scriven's paradox is explained to understand the notion of contact line singularity. The stress singularity at the tri-phase contact line can be relieved using a number of slip models and precursor film theory. A separate section is devoted to the precursor film, its origin and salient features. An in-depth literature review of droplet spreading and imbibition studies considering precursor film assumption with particular emphasis on contact line pinning, is presented.

Chapter 2 focuses on the role of characteristic parameters (radius and height of droplet) in the numerical prediction of droplet radius and contact angle. An existing model developed on the basis of lubrication approximation is used to investigate the effect of characteristic parameters on the spreading of droplets over substrates. Based on two main stages of spreading (initial and equilibrium), characteristic radius and height were first evaluated. The model predictions were then compared with experimental results in literature for both impermeable and permeable substrates. The investigation provides evidence that the choice of characteristic length scales based on either stage enables accurate prediction of the droplet base radius and contact angle. In addition,

a new scaling relation for the prediction of the numerical disjoining pressure, with an error of $\pm 5\%$, is proposed.

Chapter 3 presents the outcome of the experimental and numerical investigation of droplet spreading and imbibition on lab-fabricated and commercial PES microporous membranes. Microporous membranes are permeable substrates primarily used for waste-water treatment and desalination. The hydrophilicity of the membranes is an important factor which affects its flux performance. The membranes are characterized for permeability by filtration test, cross-section thickness by SEM images, surface roughness by AFM data, and hydrophilicity by dynamic contact angle measurements. The choice of membranes of different nominal pore sizes ensures a diverse range of imbibition time scale. The hydrodynamic permeability of these membranes is calculated based on the cross-section thickness and its resistance, which is obtained from filtration test. A lubrication-based mathematical model using precursor film approximation is used to study the behavior of droplet spreading and imbibition on the membrane surface. The theoretical disjoining pressure is also shown to be related to its numerical value obtained from the mathematical model, in the case of apolar and polar interactions. The effective permeability obtained by validating the numerical predictions with contact angle experiments, is then matched to hydrodynamic permeability by introduction of lubrication ratio at the equilibrium stage.

Chapter 4 summarizes the findings of the thesis and the future direction of research along with the contributions in the form of preprints and conference presentations.
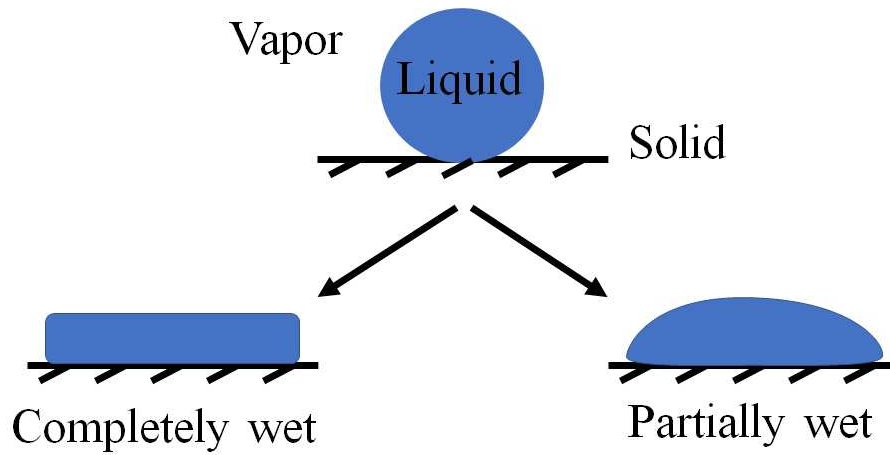
Figure 1.1: Two possible scenarios when droplet interacts with the solid surface.
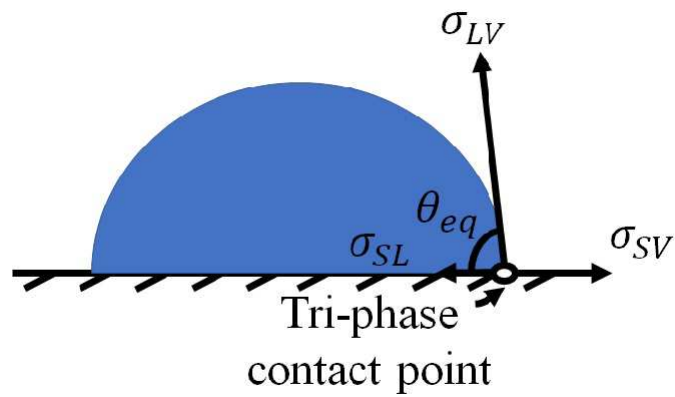
Figure 1.2: Droplet configuration in (quasi-)equilibrium stage highlighting the tri-phase contact point.
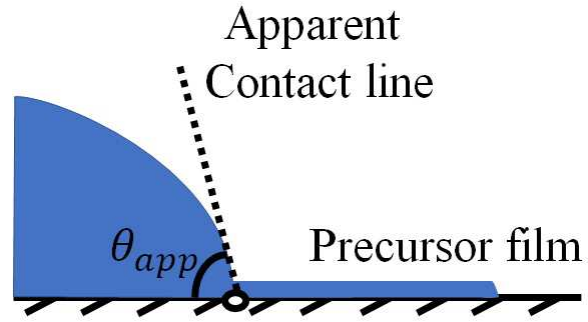
Figure 1.3: The visual representation of the apparent contact line and contact angle in the presence of precursor film.
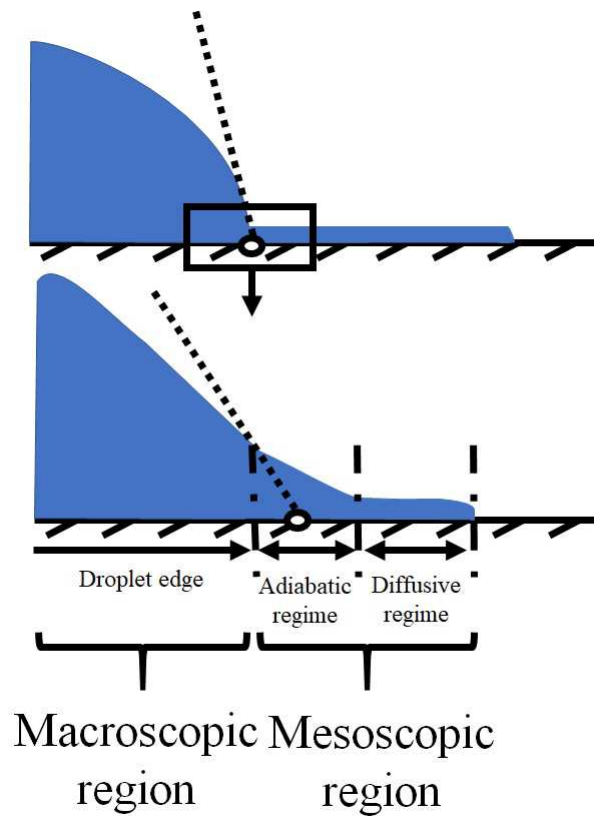
Figure 1.4: A schematic representation of the structure of the precursor film with clear demarcation between the macroscopic and mesoscopic regions.

Chapter 2

Droplet spreading and imbibition: Role of characteristic length scales and modified disjoining pressure

2.1 Introduction

Droplet spreading is ubiquitous in nature and has been exploited in many applications such as microfluidic devices [64], printing processes [65], spray cooling [66], and tissue assays [67]. The spreading of a liquid on a substrate is dictated by physical parameters [68–70], topography [71–73], and chemical heterogeneities [74–76]. The spreading behaviour of a perfectly wetting liquid on a smooth, impermeable substrate is governed by Tanner's law that describes the time evolution of droplet radius ($\sim \text{time}^{1/10}$) and droplet height ($\sim \text{time}^{-1/5}$) [4]. Permeability of the substrate is another pertinent feature which affects the spreading of the droplet [77, 78]. Permeation plays a significant role in the latter stages of spreading which is marked by retraction of the contact line and consequently, complete imbibition of the droplet volume. The characteristics of a perfectly wetting liquid spreading on a dry, permeable substrate fall on two universal curves [79]. However, no such universal behavior has been observed for partially wetting liquids on permeable substrates.

Droplet spreading on a substrate is a classical example of a moving contact line problem. Numerical techniques have been found as a versatile tool to track the interface height in droplet spreading studies. Some of the most commonly used techniques include Molecular Dynamics simulation [80–84], Lattice Boltzmann method [85–87], Volume of Fluid (VoF) [88], and lubrica-

tion based approach [61, 63, 68, 89]. Each of the aforementioned techniques has its pros and cons. For instance, the mesh generation around contact line in VoF is challenging. MD and Lattice Boltzmann are relatively computationally expensive. The lubrication approach is based on the exact tracking of the interface using long wave approximated mass and momentum equations. The scaling factors in the lubrication based approach are radius and height of the droplet. The tri-phase contact line is prone to shear-stress singularity due to the no-slip condition which has been addressed through a number of approaches using lubrication approximation. The most common approach is to use a slip model between the liquid and the solid to relieve the stress singularity. Using this model results in a nonlinear equation which can be solved either asymptotically [89–93] or numerically [68, 94]. A constitutive relation describes the contact line velocity in terms of the apparent contact angle. Although slip model provides accurate results, its main shortcoming, however, lies in the accurate prediction of the proportionality constant and the spreading exponent in the constitutive relation since the spreading exponent varies for different liquid-substrate combinations [71].

Another approach to remove the contact line singularity is precursor film assumption. A precursor film is a microscopic film, moving ahead of the macroscopic edge of the spreading droplet [51, 52]. This enables the velocity field to be single valued at the contact line with a finite viscous force [95]. The contact line region is described by disjoining pressure which consists of attractive and repulsive components of intermolecular forces [61–63]. The precursor film or "primary film" was first observed for the water and acetic acid drops spreading on glass and steel substrates [43]. The thickness of the precursor film was estimated to be few hundreds angstrom using ellipsiometry and interferometry techniques [45], scanning electron microscopy [46], and polarised reflection microscopy [96]. The main challenge of this approach is the sensitivity of the equilibrium contact angle to the disjoining pressure parameter.

Identifying a proper characteristic radius and height is the first step towards development of a predictive model for droplet spreading over substrates. The characteristic values are typically selected at the onset of equilibrium from experimental data [63]. A possible explanation for selecting the equilibrium characteristic values might be related to the experimental measurement and easier evaluation of equilibrium values. However, these studies would have been more interesting if the sensitivity of the results to the selection of other

characteristic values is included. For a partially wetting liquid, the equilibrium contact angle has a finite non-zero value and the equilibrium stage is interpreted to be controlled by disjoining pressure. The disjoining pressure, $\Pi = A\left[\left(\frac{b}{h}\right)^n - \left(\frac{b}{h}\right)^m\right]$ is a combination of repulsive (first term) and attractive (second term) components acting when the droplet height is small and comparable to the precursor film thickness, b, $(n, m) = (3, 2)$, and A is the disjoining pressure parameter. It has been shown that A is inversely proportional to the precursor film thickness. It also depends on the equilibrium contact angle and (n, m) [97]. However, none of the proposed relations in the literature provide a viable A which leads to a better agreement between numerical prediction and experimentally measured contact angle.

The present chapter is aimed at investigating the effect of characteristic length scales (radius and height) on the spreading of partially wetting droplet over both impermeable and permeable substrates. A mathematical model is used to describe the contact line region through precursor film assumption [63]. Using the no-slip condition at the substrate, a nonlinear partial differential equation is derived which describes the spatio-temporal evolution of droplet height based on lubrication approximation. A disjoining pressure model is employed to remove contact line singularity [59, 61, 62]. For imbibition, Poiseuille flow driven by excess liquid pressure is assumed in each unconnected vertical pore which essentially removes the need for thickness-dependent permeability [98]. Normalising factors are defined based on the initial and equilibrium stages of droplet spreading. Using reported experimental data [1–3], the aim is to investigate whether the prediction of droplet base radius and contact angle is influenced by the stage-dependent characteristic radius and height. In addition, the numerical disjoining pressure parameter is predicted based on its theoretical value through different stages of spreading.

2.2   Mathematical Formulation

An axi-symmetric liquid droplet is considered to spread on a smooth, horizontal substrate (Fig. 2.1(a)). The dynamics of droplet spreading depends on the nature of the substrate and is different for impermeable and permeable substrate, as illustrated in Fig. 2.1(b) and Fig. 2.1(c). The droplet is assumed to be an incompressible, Newtonian liquid with constant density ρ, dynamic viscosity, μ and surface tension, σ. Since the droplet is assumed to be

axi-symmetric in nature, the governing equations are considered in cylindrical coordinates.

2.2.1 Governing Equations

To describe the droplet spreading, pressure, p and velocity field, $\mathbf{v} = (u, w)$ is introduced where u and w denote the velocity in radial and vertical directions respectively. The continuity equation and Navier-Stokes equations are as follows:

$$\frac{1}{r}\frac{\partial}{\partial r}(ru) + \frac{\partial w}{\partial z} = 0 \tag{2.1}$$

r-momentum equation:

$$\rho\left(\frac{\partial u}{\partial t} + u\frac{\partial u}{\partial r} + w\frac{\partial u}{\partial z}\right) = -\frac{\partial p}{\partial r} + \rho g_r + \mu\left\{\frac{1}{r}\frac{\partial}{\partial r}\left(r\frac{\partial u}{\partial r}\right) - \frac{u}{r^2} + \frac{\partial^2 u}{\partial z^2}\right\} \tag{2.2}$$

z-momentum equation:

$$\rho\left(\frac{\partial w}{\partial t} + u\frac{\partial w}{\partial r} + w\frac{\partial w}{\partial z}\right) = -\frac{\partial p}{\partial z} + \rho g_z + \mu\left\{\frac{1}{r}\frac{\partial}{\partial r}\left(r\frac{\partial w}{\partial r}\right) + \frac{\partial^2 w}{\partial z^2}\right\} \tag{2.3}$$

where g_r and g_z is the acceleration due to gravity in the r- and z-direction, respectively.

2.2.2 Boundary Conditions

At the liquid-gas interface, $z = h(r, t)$, the kinematic condition is used to relate the velocity field to interface height.

$$w = \frac{\partial h}{\partial t} + u\frac{\partial h}{\partial r} \tag{2.4}$$

The normal and tangential component of interfacial stress balance is as follows:

$$\hat{\mathbf{n}}.\mathbf{T}.\hat{\mathbf{n}} = 2H\sigma - \Pi, \; \hat{\mathbf{t}}.\mathbf{T}.\hat{\mathbf{n}} = t.\nabla\sigma \tag{2.5}$$

where $\mathbf{T} = \mu(\nabla u + \nabla u^T)$ is the viscous stress of the liquid, $\hat{\mathbf{n}}$ and $\hat{\mathbf{t}}$ are unit vector normal and tangential to the liquid-gas interface respectively which are defined as follows:

$$\hat{\mathbf{n}} = \frac{(-\frac{\partial h}{\partial r}, 1)}{\sqrt{1 + (\frac{\partial h}{\partial r})^2}}, \hat{\mathbf{t}} = \frac{(1, \frac{\partial h}{\partial r})}{\sqrt{1 + (\frac{\partial h}{\partial r})^2}} \tag{2.6}$$

The curvature of the substrate is given by

$$2H = -\left(\frac{\partial^2 h}{\partial r^2} + \frac{1}{r}\frac{\partial h}{\partial r}\right) \tag{2.7}$$

A two term disjoining pressure, Π [59, 99] which is used to relieve the stress singularity at the contact line is given by

$$\Pi = A\left[\left(\frac{b}{h}\right)^n - \left(\frac{b}{h}\right)^m\right] \tag{2.8}$$

where $A \geq 0$ is the disjoining pressure parameter and exponents, $(n, m) = (3, 2)$ are constant and b is the precursor film thickness. The choice of exponents (3,2) can be understood from the nature of the function. When compared to the widely used Lennard-Jones potential with exponents (12,6), the depth of the (3,2) potential well is much lesser and the transition from attractive to repulsive nature is smoother. This enables accurate prediction of the contact line region with greater computational efficiency [100]. The value of A is related to the equilibrium contact angle, θ_{eq} as follows [99]:

$$A = \frac{(n-1)(m-1)}{b(n-m)}\sigma(1 - cos\theta_{eq}) \tag{2.9}$$

At the liquid-substrate interface, $z = 0$, the imbibition condition is used:

$$w = -\frac{\kappa}{\mu}p \tag{2.10}$$

where κ is the proportionality constant with units of length and depends on pore diameter, number of pores per unit area, and substrate thickness [98]. No-slip condition is as follows:

$$u = 0 \tag{2.11}$$

The following conditions are imposed for axi-symmetric spreading:

$$\left.\frac{\partial h}{\partial r}\right|_{r=0} = 0, \left.\frac{\partial^3 h}{\partial r^3}\right|_{r=0} = 0 \tag{2.12}$$

26

For droplet volume V_0 to be conserved, following equation is used:

$$\int\limits_0^{r_0} 2\pi r h(r) dr = V_0 + \pi b r_0^2 \tag{2.13}$$

where subscript 0 denotes the initial value of a quantity and πb is the correction factor for precursor film on a circular region with radius equal to the characteristic value.

2.2.3 Scalings

The governing equations and the corresponding boundary conditions are normalized using following factors:

$$r = l\tilde{r}, z = h\tilde{z}, u = u_{sc}\tilde{u}, w = \epsilon u_{sc}\tilde{w}$$

$$t = \frac{l}{u_{sc}}\tilde{t}, p = p_{sc}\tilde{p}, \Pi = p_{sc}\tilde{\Pi} \tag{2.14}$$

where $u_{sc} = \frac{\epsilon^3 \sigma}{3\mu}$ is the characteristic spreading speed, $p_{sc} = \frac{h\sigma}{l^2}$ is the pressure scale, $b = h\tilde{b}$ is the precursor film thickness, and $\epsilon = \frac{h}{l}$ is the lubrication ratio. The effective permeability of the substrate is given by $\kappa = \frac{dh^3}{3l^2}\tilde{\kappa}$ where d is the thickness of the substrate. The non-dimensional quantities are denoted with tilde. The scaling factors are based on the fact that the droplet is spreading under the influence of capillary action. It is also assumed that the viscous forces balance capillary forces. The dominance of capillary pressure at the initial stages is primarily because of larger curvature. As the droplet spreads (and the spreading radius increases), disjoining pressure becomes more dominant, owing to smaller film thickness. Disjoining pressure is long-ranged, attractive and short-ranged, repulsive. The droplet is assumed to be thin, which means the ratio of characteristic height, h, to characteristic radius, l, is much less than unity ($\epsilon \ll 1$). Hence, the lubrication approximation is applied which reduces the governing equations and boundary conditions to:

Continuity equation:

$$\frac{\partial \tilde{w}}{\partial \tilde{z}} + \frac{1}{\tilde{r}}\frac{\partial(\tilde{r}\tilde{u})}{\partial \tilde{r}} = 0, \tag{2.15}$$

r-momentum equation:

$$\frac{\partial^2 \tilde{u}}{\partial \tilde{z}^2} - 3\frac{\partial \tilde{p}}{\partial \tilde{r}} = 0, \tag{2.16}$$

27

z-momentum equation:

$$-\frac{\partial \tilde{p}}{\partial \tilde{z}} - B = 0 \tag{2.17}$$

where $B = \frac{l^2 \rho g}{\sigma}$ is the Bond number.

The kinematic condition at $\tilde{z} = \tilde{h}(\tilde{r}, \tilde{t})$, is as follows:

$$\tilde{w} = \frac{\partial \tilde{h}}{\partial \tilde{t}} + u \frac{\partial \tilde{h}}{\partial \tilde{r}}, \tag{2.18}$$

The normal component of interfacial stress balance can be simplified by considering pressure field across the interface. The tangential component follows directly from the vanishing shear stress condition which in the lubrication limit predicts zero shear stress in the r-z plane. The normal and tangential component of interfacial stress balance is thus written as follows:

$$\tilde{p} = -\left(\frac{\partial^2 \tilde{h}}{\partial \tilde{r}^2} + \frac{1}{\tilde{r}} \frac{\partial \tilde{h}}{\partial \tilde{r}}\right) - \tilde{A}\left[\left(\frac{\tilde{b}}{\tilde{h}}\right)^3 - \left(\frac{\tilde{b}}{\tilde{h}}\right)^2\right], \tag{2.19}$$

$$\frac{\partial \tilde{u}}{\partial \tilde{z}} = 0 \tag{2.20}$$

where $\tilde{A} = \frac{A}{p_{sc}}$.

Imbibition condition at $\tilde{z} = \tilde{b}$ is as follows:

$$\tilde{w} = -\frac{\tilde{\kappa}}{\mu d} \tilde{p} \tag{2.21}$$

No-slip condition at $\tilde{z} = 0$ is as follows:

$$\tilde{u} = 0 \tag{2.22}$$

2.2.4 Numerical Scheme

The non-dimensional time-evolution equation for the droplet height is obtained by integrating eqns.(2.15-2.17) subject to the boundary conditions (2.18-2.22):

$$\frac{\partial \tilde{h}}{\partial \tilde{t}} = \frac{1}{\tilde{r}} \frac{\partial}{\partial \tilde{r}} \left\{ \tilde{r} \tilde{h}^3 \frac{\partial}{\partial \tilde{r}} \left(B\tilde{h} - \tilde{\Pi} - \frac{\partial^2 \tilde{h}}{\partial \tilde{r}^2} - \frac{1}{\tilde{r}} \frac{\partial \tilde{h}}{\partial \tilde{r}} \right) \right\} - \tilde{\kappa} \left\{ B(\tilde{h} - \tilde{b}) - \tilde{\Pi} - \frac{\partial^2 \tilde{h}}{\partial \tilde{r}^2} - \frac{1}{\tilde{r}} \frac{\partial \tilde{h}}{\partial \tilde{r}} \right\} \tag{2.23}$$

The solution of eqn. 2.23 is subject to the following boundary conditions on the domain $0 \le \tilde{r} \le L$:

$$\frac{\partial \tilde{h}}{\partial \tilde{r}}(0, \tilde{t}) = 0, \tilde{h}(L, \tilde{t}) = \tilde{b}, \frac{\partial^3 h}{\partial \tilde{r}^3}(0, \tilde{t}) = 0, \frac{\partial \tilde{h}}{\partial \tilde{r}}(L, \tilde{t}) = 0. \tag{2.24}$$

The initial droplet profile is obtained in the form of a fourth-degree polynomial satisfying the above boundary conditions (2.24) and the volume constraint (2.13). Computational domain length, L is considered to be 4 with 600-700 points per unit length. The spatial derivatives are discretised using second-order central finite difference scheme which converts the PDE into sets of differential algebraic equations (DAE). For the resulting system of DAEs, an adaptive time-step solver, DASSL, is used which is available in SLATEC library (Appendix A-1). The average simulation time is less than one hour, which makes it very computationally inexpensive. The grid independence and validation of the numerical code are presented in Appendix B-1 and C-1 respectively.

The apparent contact angle is found by dividing the dimensional values of droplet height at the axi-symmetric center to the droplet base radius.

$$tan\theta = \frac{h}{r} \tag{2.25}$$

The radius is obtained by finding the distance between the z-axis and the intersection point of the apparent contact line with the r-axis.

2.2.5 Normalising Factors

In order to obtain eqn. 2.23, two normalising factors are used. The first one is based on the radius and height of the droplet at the onset of equilibrium and the second one is described by those values at the initial stage. Based on this definition, the required parameters are calculated using both normalising factors as described below:

a. <u>First normalising factor</u>: Using equilibrium values (l_{eq}, h_{eq}) as normalising factors, the following input parameters are obtained: Normalised initial radius, $\tilde{r}_0 = \frac{l_{in}}{l_{eq}}$; normalised initial height, $\tilde{h}_0 = \frac{h_{in}}{h_{eq}}$; initial volume based on spherical-cap approximation, $V_{in} = \frac{\pi h_{in}(3l_{in}^2 + h_{in}^2)}{6}$; final volume when the droplet ceases to exist on the substrate (assuming spherical-cap), $V_{eq} = \frac{\pi h_{eq}(3l_{eq}^2 + h_{eq}^2)}{6}$; normalised initial volume, $\tilde{V}_0 = \frac{V_{in}}{V_{eq}}$; Bond number, $B_{eq} = \frac{l_{eq}^2 \rho g}{\sigma}$; time $t_{eq} = \frac{h_{eq}^3 \sigma}{3l_{eq}^4 \mu}\tilde{t}$; and lubrication ratio, $\epsilon_{eq} = \frac{h_{eq}}{l_{eq}}$.

b. <u>Second normalising factor</u>: Using initial values (l_{in}, h_{in}) as normalising factors, the following input parameters are found as: $\tilde{r}_0 = \frac{l_{in}}{l_{in}} = 1$; $\tilde{h}_0 = \frac{h_{in}}{h_{in}} = 1$;

$\tilde{V}_0 = \frac{V_{in}}{V_{in}} = 1; \ B_{in} = \frac{l_{in}^2 \rho g}{\sigma}; \ t_{in} = \frac{h_{in}^3 \sigma}{3 l_{in}^4 \mu} \tilde{t}; \text{ and } \epsilon_{in} = \frac{h_{in}}{l_{in}}$

The dimensional time evolution equation for the droplet height is given by

$$3\mu \frac{\partial h}{\partial t} = \frac{1}{r} \frac{\partial}{\partial r} \left[r h^3 \frac{\partial}{\partial r} \left\{ \rho g h - \Pi - \sigma \left(\frac{\partial^2 h}{\partial r^2} + \frac{1}{r} \frac{\partial h}{\partial r} \right) \right\} \right]$$
$$- \kappa \left[\rho g (h - b) - \Pi - \sigma \left(\frac{\partial^2 h}{\partial r^2} + \frac{1}{r} \frac{\partial h}{\partial r} \right) \right] \qquad (2.26)$$

2.3 Results and Discussion

For a small droplet, where the effect of gravity is negligible, the driving force for spreading is capillary pressure. The maximum extent of spreading is dictated by the dominant effect of disjoining pressure over capillary pressure in the later stages. For a smooth, impermeable substrate, a perfectly wetting Newtonian liquid obeys Tanner's law [4]. However, the maximum spreading radius will vary if the liquid partially wets the substrate. Under the combined effect of attractive and repulsive components of intermolecular forces in disjoining pressure, a liquid partially wets the substrate and thus, has a finite non-zero equilibrium contact angle [56]. For smooth permeable substrates, the spreading occurs at two stages: First, the inertial stage where lubrication ratio is much larger than unity. At this stage, the droplet spreads to a maximum radius and stops momentarily. Second, the equilibrium stage which is signified by a decrease in droplet volume due to the imbibition. As a result, the droplet radius decreases and the contact angle remains constant over a particular time before becoming zero. At the equilibrium stage, the lubrication ratio is much less than unity.

A 3-step procedure is followed in order to make comparison of model predictions with experimental data:

(i) A specific value of b which yields $\tilde{b}$ through the scaling is used as a starting point.

(ii) Normalised initial radius ($\tilde{r}_0$) and height ($\tilde{h}_0$) are obtained using both normalising factors. These parameters along with $\tilde{b}$ are utilised to obtain the initial droplet profile for each case. The model parameters used for matching with the experimental values are disjoining pressure parameter, $\tilde{A}$ and non-dimensional imbibition coefficient, $\tilde{\kappa}$. $\tilde{A}$ governs the equilibrium stage of

spreading and its higher values signifies less hydrophilicity or higher equilibrium contact angle. The equilibrium stage is first matched by varying $\tilde{A}$, then $\tilde{\kappa}$ is adjusted so as to match the imbibition time. The value calculated using eqn. 2.9 is used as a starting point for A. Based on scaling (2.14), the non-dimensional quantity, $\tilde{A}$ is obtained. However, the present scaling under-predicts $\tilde{A}$ and results in lower equilibrium contact angle. As a result, many combinations of $(\tilde{A}, \tilde{\kappa})$ are tried for a specific $\tilde{b}$ until good agreement with the experimental results is found. Hence, the current approach in finding $\tilde{A}$ requires extensive numerical study that is not our interest. More discussion follows in section IV where a modification is proposed of eqn. 2.9 for better prediction of A based on the lubrication ratio.

(iii) For both impermeable and permeable substrates, (A, κ) corresponding to each value of b are obtained using the first normalising factor. The simulation is then conducted using these values and the second normalising factor. This approach provides a clear picture on the role of each normalising factor on the numerical predictions.

In Fig. 2.2, the contact angle of squalene drop spreading on glass [1] is compared with the model predictions. There is no change in volume over time since glass is impermeable. The spherical-cap approximation is used for calculating the volume of the droplet. First the initial values are normalised with the equilibrium characteristic values. For a specific b (<1 μm [42]), the initial shape of the droplet is obtained. As can be seen in Fig. 2.2, there is a good agreement between model predictions and experimental data, only at the equilibrium stage of spreading and the model failed in predicting the earlier stages of spreading. Then, using the corresponding (b, A) obtained by the first normalising factor, the simulation is performed based on the second normalising factor. A clear overlap in the numerical prediction highlights the fact that either normalising factor can predict the equilibrium contact angle. The model was further tested for $b = 0.75$ μm and 0.5 μm and a good match was observed (The results are not provided since the behaviour was exactly the same). For each b, the numerical predictions coincided using both normalising factors.

The decrease in contact angle is sharper in numerical simulation compared to the experiments and equilibrium is reached earlier. The difference between numerically predicted results and experiments might be attributed to the substrate roughness. Since any substrate possesses inherent roughness (unless

otherwise specified), one way to delay the onset of equilibrium is to take into account the effect of substrate roughness in the mathematical model. In the presence of roughness, the contact line is pinned and the apparent contact angle increases [101]. The dynamic contact angle measurements on a real surface can be interpreted as summation of numerous small scale pinning effects. The contact line pinning behaviour has been observed in physico-chemical processes ranging from evaporation [102–105] to drying of drops[106, 107], from surfactants [108, 109] to thermo-capillary stresses [110, 111]. However, in the present scenario, no such process is applicable, keeping in mind the conditions under which experiment was performed by the authors [1]. To incorporate roughness in the model, a shape function, $\tilde{z} = \tilde{\gamma}(\tilde{r})$ is introduced in this study. The governing equations remain unchanged in the presence of substrate roughness. However, the kinematic condition and the interfacial stress balance components are evaluated at $\tilde{z} = \tilde{\gamma}(\tilde{r}) + \tilde{h}(\tilde{r}, \tilde{t})$. The imbibition and no-slip conditions also occur at $\tilde{z} = \tilde{\gamma}(\tilde{r}) + \tilde{b}$ and at $\tilde{z} = \tilde{\gamma}(\tilde{r})$ respectively. Based on these modifications, the droplet evolution equation takes the following form:

$$
\frac{\partial \tilde{h}}{\partial \tilde{t}} = \frac{1}{\tilde{r}} \frac{\partial}{\partial \tilde{r}} \left\{ \tilde{r} \tilde{h}^3 \frac{\partial}{\partial \tilde{r}} \left(B(\tilde{h} + \tilde{\gamma}) - \tilde{\Pi} - \frac{\partial^2 (\tilde{h} + \tilde{\gamma})}{\partial \tilde{r}^2} - \frac{1}{\tilde{r}} \frac{\partial (\tilde{h} + \tilde{\gamma})}{\partial \tilde{r}} \right) \right\}
$$
$$
- \tilde{\kappa} \left\{ B(\tilde{h} - \tilde{b}) - \tilde{\Pi} - \frac{\partial^2 (\tilde{h} + \tilde{\gamma})}{\partial \tilde{r}^2} - \frac{1}{\tilde{r}} \frac{\partial (\tilde{h} + \tilde{\gamma})}{\partial \tilde{r}} \right\} \quad (2.27)
$$

There are complicated forms of shape function, $\tilde{\gamma}$, in the literature that are able to imitate a real rough substrate very accurately [112, 113]. However, in this study, the most simplified form of this function, known as Gaussian model [114], is utilised. The Gaussian model of roughness is represented by the following equation:

$$
\tilde{\gamma}(\tilde{r}) = -\tilde{r}_1 exp \left(- \frac{(\tilde{r} - \tilde{r}_{loc})^2}{2\tilde{r}_2^2} \right) \quad (2.28)
$$

where $\tilde{r}_1, \tilde{r}_2 = O(\tilde{b})$ and $\tilde{r}_{loc}$ represents the location of the defect.

For the present simulation, $\tilde{r}_1$ and $\tilde{r}_2$ are selected as 50 $\tilde{b}$ and 5 $\tilde{b}$, respectively. These values were optimized so as to have better prediction when compared with experimental data. To investigate the role of defects on contact line motion, three different configurations are selected, as shown in Fig. 2.3(a). When the defect is placed very close to the initial shape (Defect (i) in Fig. 2.3),

the pinning phenomenon is observed which is represented by no change in radius over a certain time period. If the nature of the defect remains unchanged but is placed much farther from the initial shape (Defect (ii)), pinning persists for comparatively longer period. This is attributed to non-uniform speed of droplet spreading. The characteristic speed of a spreading droplet is much higher at the initial stages and as time passes the spreading front slows down owing to substrate irregularities. Since the height of the droplet also decreases over time, the rate of conversion of the potential energy (owing to greater height in the initial stages) to kinetic energy diminishes which is manifested in the speed of the spreading front. As a result, for a defect placed much farther on the path, the contact line has a tendency to stay pinned for a longer time and thus, the equilibrium is delayed. If there is another identical defect placed at a certain distance from the first defect (Defect (iii)), a staircase-like behaviour is observed marked by a delayed equilibrium. Our preliminary investigations showed that this staircase behaviour depends on the nature, density and spacing of defects. The detailed study of staircase bahviour with the aim of acquiring more realistic replication of a rough substrate is the topic of our ongoing research.

In another study of impermeable substrate, the contact angle of di-n-butyl phthalate (DBP) spreading on poly(ethyleneterephthalate) (PET) is considered [1]. A similar procedure as the previous case is followed and a good agreement with the experimental data is achieved for $b = 0.98$ μm (Fig. 2.4), 0.75 μm, and 0.5 μm. Comparing the model predicted results and experiments show that irrespective to the applied characteristic lengths (for radius and height) and precursor film, b, the equilibrium contact angle is mainly governed by the proper choice of A.

For a permeable substrate, model predictions and experimental measurements of water droplet spreading on a poly(butylene ter-ephthalate) (h-PBT-4) mat are compared in the absence of contact line pinning for $b = 0.98$ μm (Fig. 2.5). In the experimental work, the onset of lubrication phase was reported as $t = 0.117$ s. The corresponding initial height (h_{in}) and radius (l_{in}) of the droplet were 0.79 mm and 2.81 mm, respectively. The equilibrium height (h_{eq}) and radius (l_{eq}) were reported to be 0.159 mm and 2.087 mm, respectively. The initial droplet profile is obtained based on these values. As can be observed in Fig. 2.5, there is an overlap between numerical predictions using either normalising factor for constant (b, A, κ). In both cases, droplet ra-

dius increases at the initial stages followed by a retraction due to permeation which is similar to what is observed in experiments. Using other b values ($b = 0.75$ μm and 0.5 μm), the same results are obtained. This reinforces our hypothesis that using either normalising factors enables accurate prediction of the experimental values, for both permeable and non-permeable substrates. The time lag between the numerical prediction and experimental values is primarily related to the starting point of simulation at $t = 0.117$ s as this marks the onset of lubrication. A possible explanation might be the difference between experimental and numerical initial droplet profile to run the simulation.

To showcase another example of the spreading phenomena on a permeable substrate, the droplet radius and contact angle of silicone oil grade SO300 spreading on unidirectional mat (UDMAT) [3] are compared with the model predictions. The initial and equilibrium height and radius of the droplet were obtained at $t = 0$ and at the onset of equilibrium stage respectively. Using first normalising factor resulted in better agreement with experimental data for $b = 0.98$ μm (Fig. 2.6) and 0.75 μm. When compared to the second normalising factor, there is an offset in prediction which might be due to the droplet profile employed in this case for running simulation.

The significant difference between model prediction of the contact angle (Fig. 2.6(b)) for $t < 2$ s is attributed to large lubrication ratio ($\epsilon \gg 1$) at the inertial stage. The second normalising factor hinges on inertial values which was not measured accurately. Even though dynamic radius and height measurements are exclusively reported, the literature did not provide any proper explanation for the calculation of the contact angle [3].

2.4 Modified scaling for better prediction of Equilibrium contact angle

Theoretically, the disjoining pressure parameter, A_{th} is related to the equilibrium contact angle, θ_{eq} as follows [99]:

$$A_{th} = \frac{(n-1)(m-1)}{b(n-m)}\sigma(1 - cos\theta_{eq}) \; or, \frac{2}{b}\sigma(1 - cos\theta_{eq}) \qquad (2.29)$$

To numerically model the spreading process, it is essential to start with an initial guess of $\tilde{A}$. Since the equilibrium contact angle, θ_{eq}, is known from the dynamic contact angle measurement, it is possible to have an estimate of $\tilde{A}$ ($A = p_{sc}\tilde{A}$).

It is found that the suggested A (from eqn. 2.29) cannot predict the equilibrium contact angle accurately. Hence, the following modification is proposed:

$$A_m = \frac{A_{th}}{\epsilon^n} \qquad (2.30)$$

where n is the exponent to be ascertained for impermeable and permeable substrates.

The role of both normalising factors on the prediction of n for droplet spreading on impermeable and permeable substrate is presented next.

a. First normalising factor:

(i) Impermeable cases: The squalene droplet spreading on glass is considered as an impermeable case. Starting with the first normalising factor, n is varied from 0 to 1.15 until the ratio A_m/A was close to 1, with an error of $\pm 5\%$. According to Fig. 2.7(a), choosing $n = 1.12$ resulted in a better starting guess of $\tilde{A}$ for a particular precursor film thickness. Similarly, for DBP spreading on PET, n is changed from 0 to 1.3 (Fig. 2.8(a)). A choice of $n = 1.24$ has led to a better starting guess of $\tilde{A}$ for each value of precursor film thickness.

(ii) Permeable cases: For water droplet spreading on h-PBT-4 mat, n is obtained to be 0.95, 0.8, 0.7 for $b = 0.98$ μm, 0.75 μm, and 0.5 μm, respectively (Fig. 2.9(a)). Following the similar procedure for SO300 droplet spreading on UDMAT, the value of n is evaluated to be 0.65 with an error within $\pm 5\%$ for $b = 0.98$ μm and 0.75 μm (Fig. 2.10(a)).

b. Second normalising factor:

(i) Impermeable cases: Figs. 2.7(b) and 2.8(b) show that, using second normalising factor the value of n are obtained to be 6.6 and 9.2 for squalene droplet spreading on glass and DBP spreading on PET, respectively. It is noteworthy that in both experiments, no effort was made to precisely track the onset of lubrication. This could be one plausible explanation for such a big variation in the value of n for these impermeable cases.

(ii) Permeable cases: For water droplet spreading on h-PBT-4 mat, the values of $n = 1.9$, 1.6, and 1.4 are obtained for $b = 0.98$ μm, 0.75 μm, and 0.5 μm, respectively (Fig. 2.9(b)). The onset of lubrication was precisely tracked. The second normalising factor yields value of $n = 8.5$ for $b = 0.98$ and 0.75 μm for SO300 spreading on UDMAT.

In summary, first normalising factor yields n between 1.0-1.3 for impermeable and 0.5-1.0 for permeable substrates, thereby leading to a better starting guess for $\tilde{A}$. For second normalising factor, it is essential to precisely track

the initial conditions. Only one experimental study on a permeable substrate meets this criterion [2]. Hence, in the absence of profound evidence, it is difficult to specify a range of n to be used for the second normalising factor.

2.5 Conclusion

Ability of a mathematical model to accurately predict the droplet radius and apparent contact angle is governed by the choice of radius and height at the initial and equilibrium stages of spreading. Using four examples of droplet spreading over impermeable and permeable substrates, it is observed that choosing radius and height in either stage of the spreading process provides similar prediction of the experimentally obtained base radius and equilibrium contact angles. In addition, incorporating the substrate roughness into the model is found to bridge the gap between model predictions and experiments for initial stages of spreading. A modified scaling which relates the theoretical value of the disjoining pressure parameter to its numerical counterpart through the lubrication ratio is also proposed. The lubrication ratio takes different exponents based on the permeability of the substrate. For impermeable and permeable substrates, n was found to be in the range of 1.0-1.3 and 0.5-1.0 respectively. The proposed method greatly simplified the initial guess for the disjoining pressure parameter in the numerical simulation as previously there was no possibility of ascertaining the value. This study has shown that it is always possible to predict the value of the lubrication exponent using the first normalising factor which depends on the equilibrium condition. However, the second normalising factor depends on the initial conditions entirely and thus, without precise tracking of the lubrication ratio it is not feasible to suggest a range of n for impermeable/permeable substrates. Overall, the equilibrium stage characteristic parameters is more appropriate since the modified scaling allows prediction of the numerical disjoining parameter with $\pm5\%$ error. As a future study, more effort is needed for the accurate calculation of the initial droplet profile and shape approximation for volume at each stage of spreading. The hypotheses provided in this work is expected to hold true when the model is extended to include the whole spectrum of spreading, especially the inertial stages when the lubrication ratio is much greater than unity.
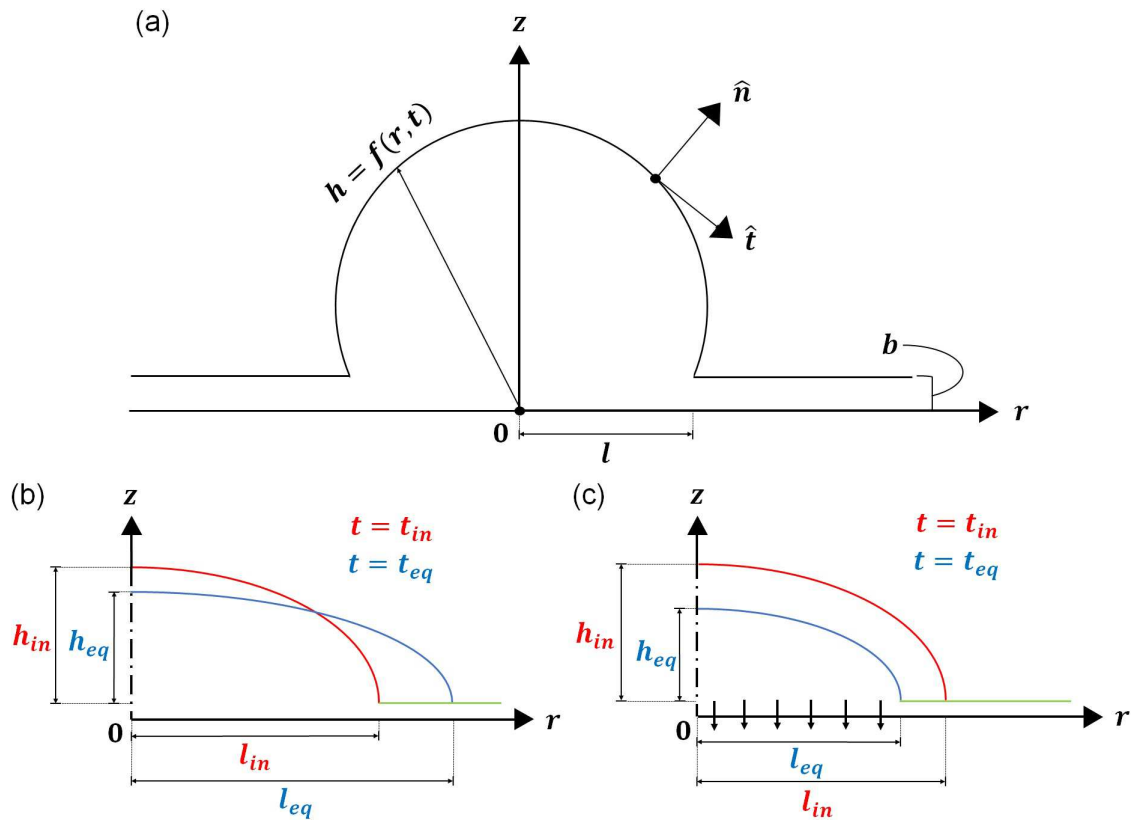
Figure 2.1: (a) Geometrical configuration of an axi-symmetric droplet and different stages of droplet spreading on (b) an impermeable substrate and (c) a permeable substrate. The subscript 'in' and 'eq' denote the initial and equilibrium value of a quantity, respectively.
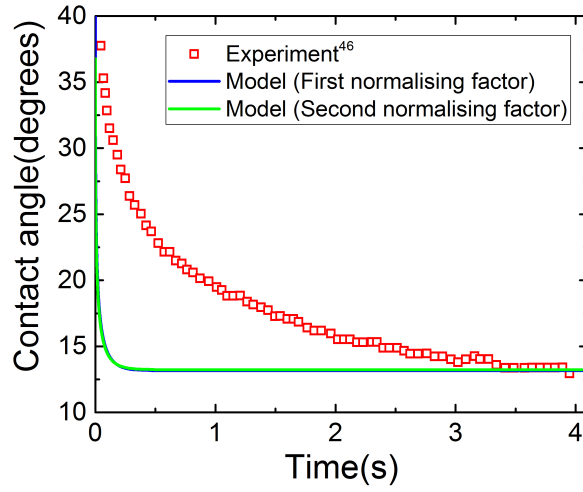
Figure 2.2: Comparison between experimental data and simulation results of contact angle of squalene spreading on glass [1]. The simulation parameters used are: $V_{in} = V_{eq} = 6.046$ μL, $l_{in} = 1.6$ mm, $l_{eq} = 2.548$ mm, $\epsilon_{in} = 0.781$, $\epsilon_{eq} = 0.229$, $B_{in} = 0.702$, $B_{eq} = 1.78$, $b = 0.98$ μm, $A = 8271$ Nm^{-2}.
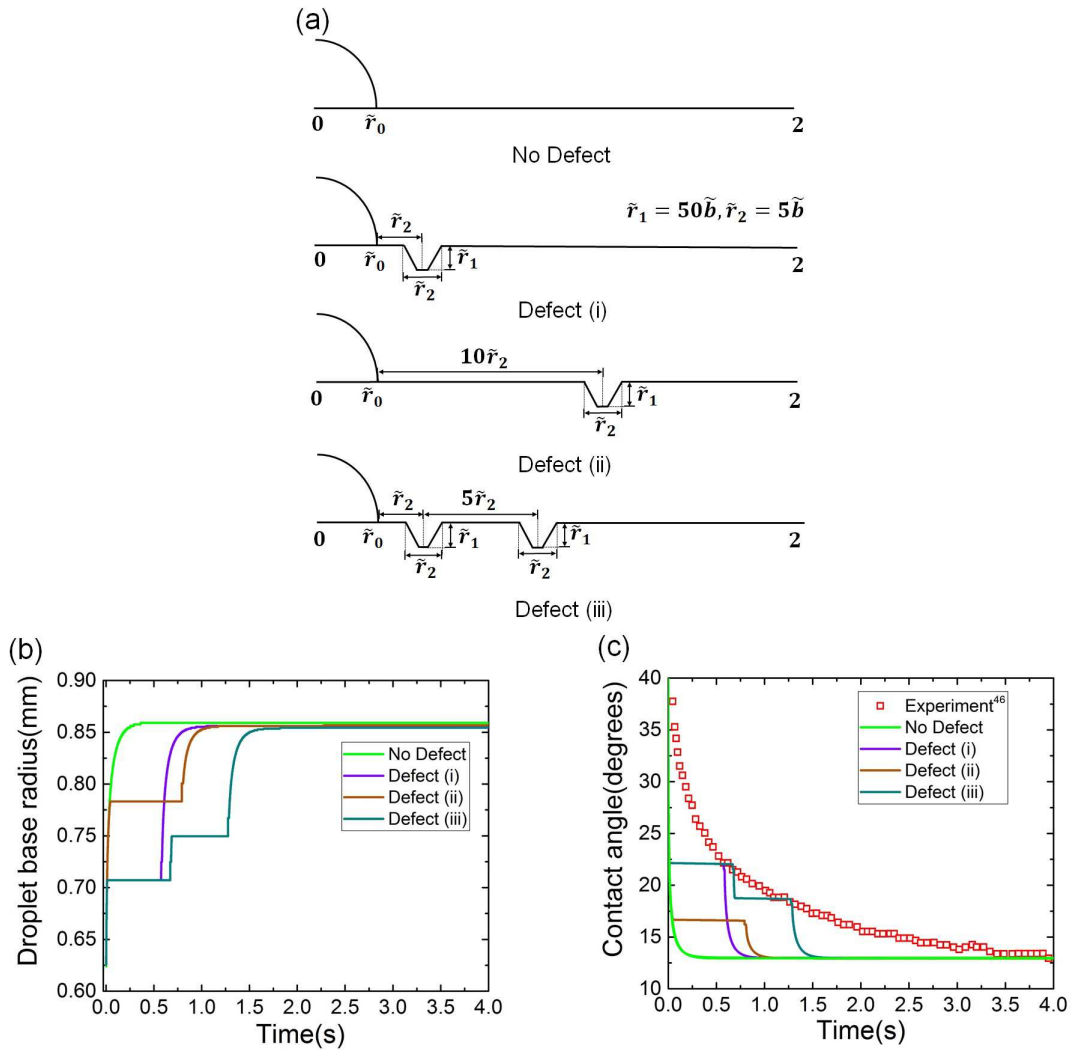
Figure 2.3: (a) The nature of defects considered. Comparison between experimental data and simulation results of (b) droplet base radius, and (c) contact angle of squalene spreading on glass in the presence of substrate roughness [1]. The simulation parameters remain unchanged.
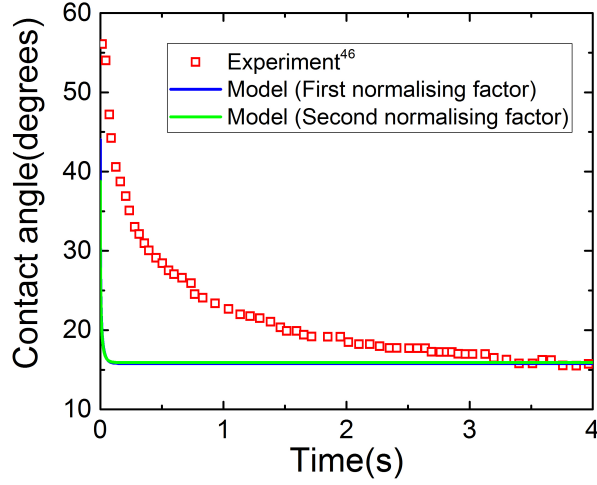
Figure 2.4: Comparison between experimental data and simulation results of contact angle of DBP spreading on PET [1]. The simulation parameters used are: $V_{in} = V_{eq} = 5$ μL, $l_{in} = 1.454$ mm, $l_{eq} = 2.238$ mm, $\epsilon_{in} = 0.839$, $\epsilon_{eq} = 0.277$, $B_{in} = 0.635$, $B_{eq} = 1.504$, $b = 0.98$ μm, $A = 13587.2$ Nm^{-2}.
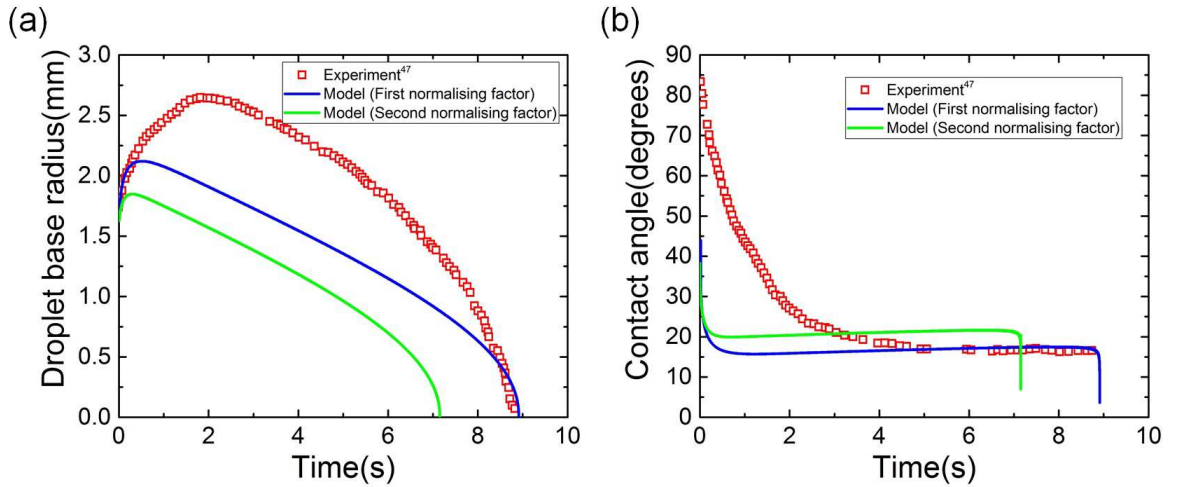
Figure 2.5: Comparison between experimental data and simulation results of (a) droplet base radius, and (b) contact angle of water droplet spreading on a h-PBT-4 mat [2]. The simulation parameters used are: $V_{in} = 10.04$ μL, $V_{eq} = 1.089$ μL, $l_{eq} = 2.81$ mm, $l_{in} = 2.087$ mm, $\epsilon_{in} = 0.281$, $\epsilon_{eq} = 0.076$, $B_{in} = 1.076$, $B_{eq} = 0.594$, $b = 0.98$ μm, $A = 6379.2$ Nm^{-2}, $\kappa/d = 5.076 \times 10^{-8}$.
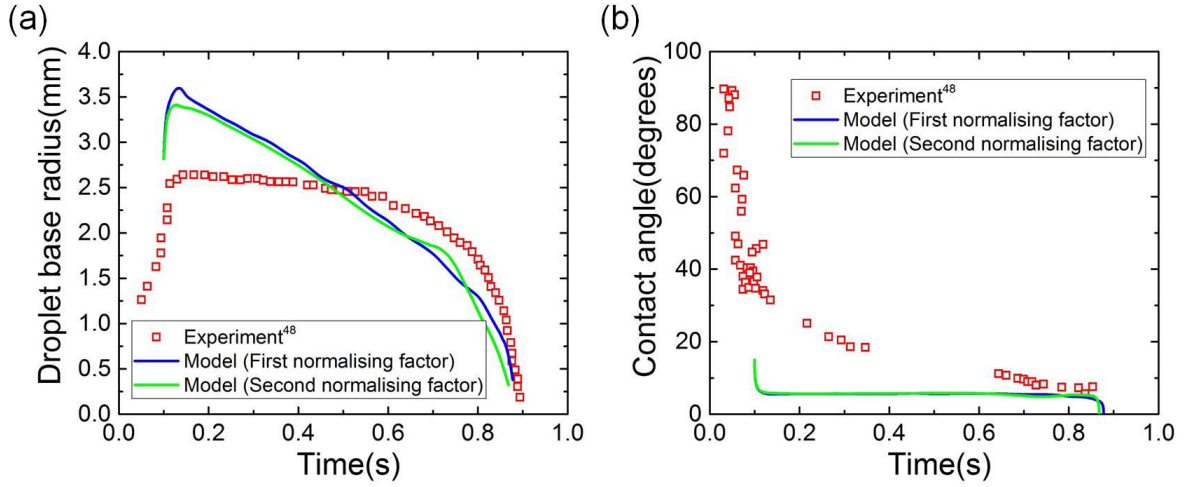
Figure 2.6: Comparison between experimental data and simulation results of (a) droplet base radius, and (b) contact angle of SO300 droplet spreading on UDMAT [3]. The simulation parameters used are: $V_{in} = 7.788$ μL, $V_{eq} = 1.609$ μL, $l_{in} = 1.7$ mm, $l_{eq} = 2.32$ mm, $\epsilon_{in} = 0.82$, $\epsilon_{eq} = 0.082$, $B_{in} = 1.404$, $B_{eq} = 2.615$, $b = 0.98$ μm, $A = 9633$ Nm^{-2}, $\kappa/d = 2.039 \times 10^{-6}$.
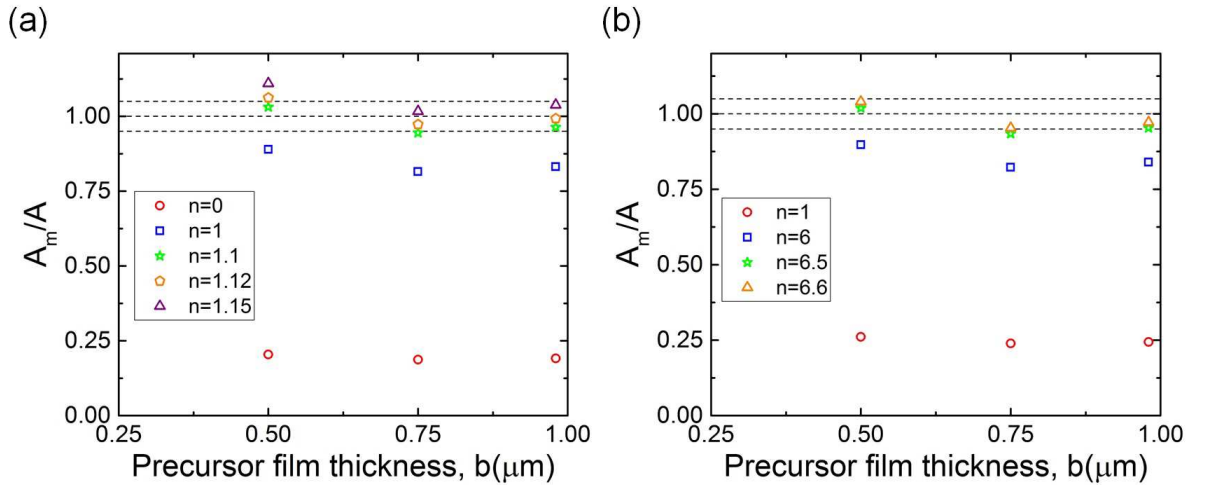
Figure 2.7: Ratio A_m/A for (a) First normalising factor and (b) Second normalising factor of squalene spreading on glass with $\theta_{eq} = 12.88°$ [1].

41
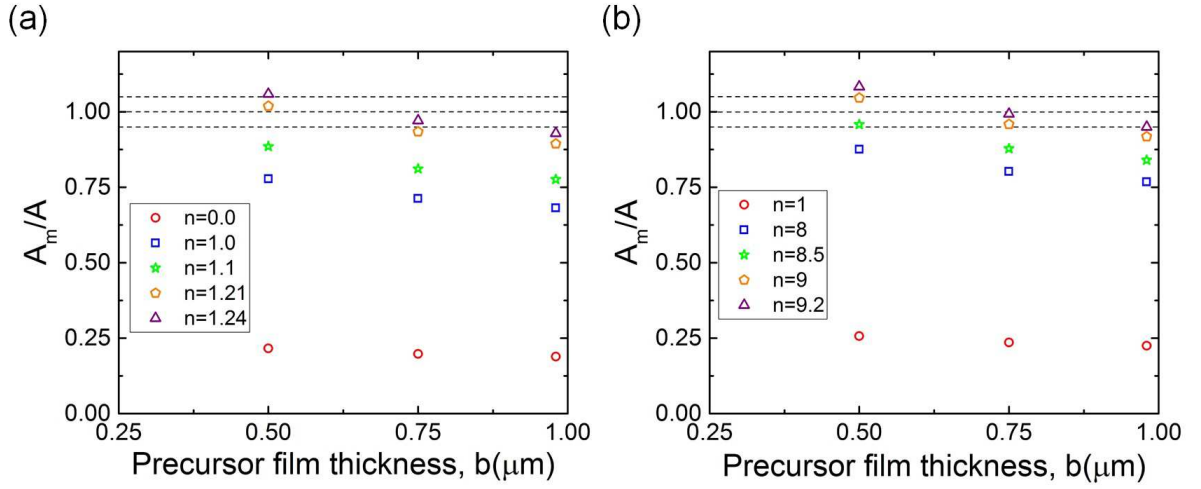
Figure 2.8: Ratio A_m/A for (a) First normalising factor and (b) Second normalising factor of DBP spreading on PET with $\theta_{eq} = 15.569°$ [1].
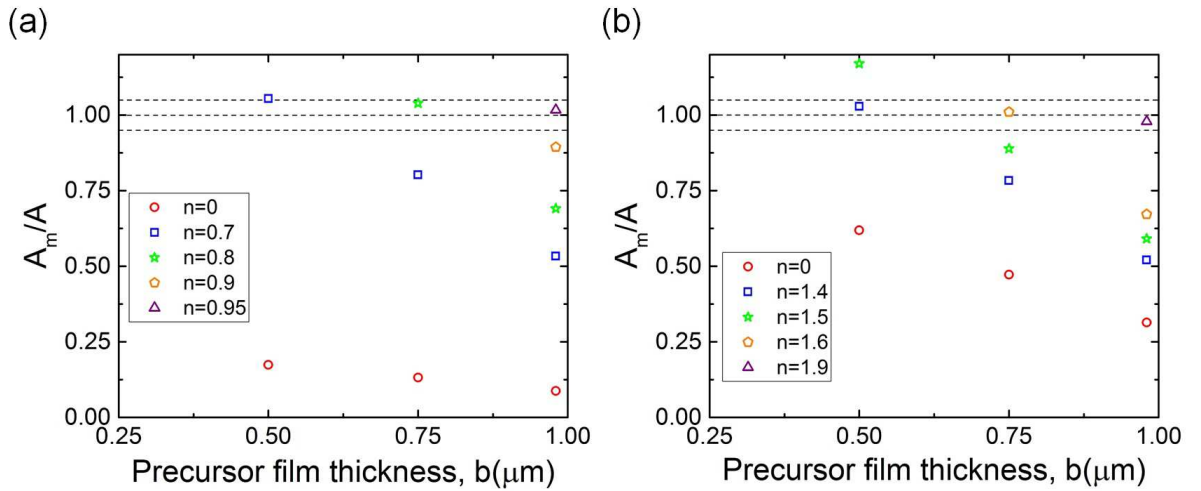
Figure 2.9: Ratio A_m/A for (a) First normalising factor and (b) Second normalising factor of water droplet spreading on a h-PBT4 mat with $\theta_{eq} = 5°$ [2].
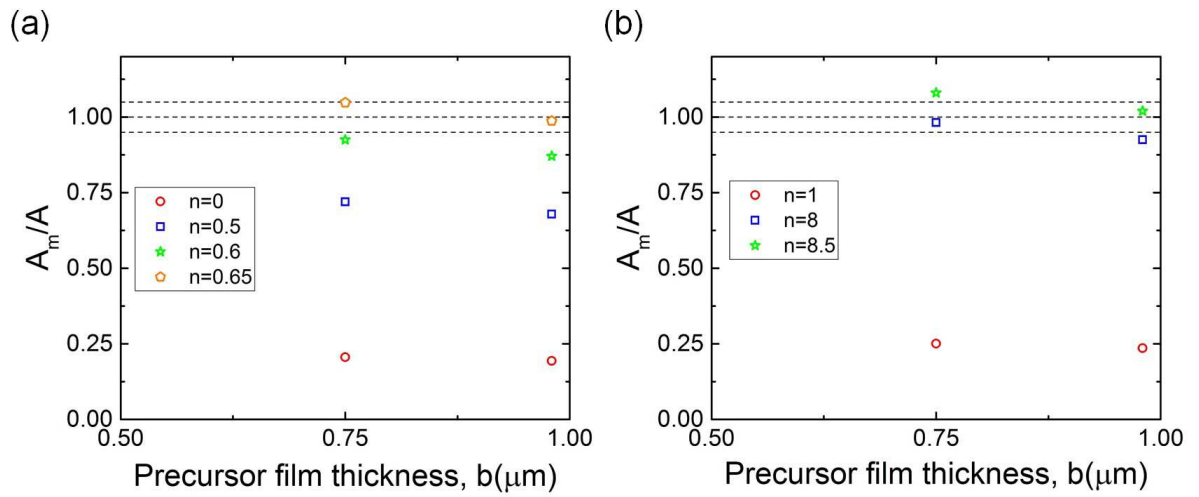
Figure 2.10: Ratio A_m/A for (a) First normalising factor and (b) Second normalising factor of SO300 spreading on UDMAT with $\theta_{eq} = 17°$ [3].

Chapter 3

An experimental and numerical study of droplet spreading and imbibition on microporous membranes

3.1 Introduction

Wetting of permeable substrates is a common phenomenon and is of utmost importance to many applications, ranging from dried blood spot sampling [115] to inkjet printing [116], from membrane filtration [117] to movement of gravity currents in porous media [118], from surface fractality in sedimentary rocks [119] to tear film on contact lens [120]. At equilibrium, the wettability of a substrate is governed by the spreading coefficient, S ($=\sigma_{solid} - (\sigma_{liquid} + \sigma_{solid-liquid})$) where σ is the interfacial tension. Theoretically, the Young-Dupre equation [121] can predict the nature of wettability. Whether a liquid will partially or completely wet a permeable substrate depends exclusively on the inherent surface energy of these substrates [122] and in some cases, topography [?]. A high or low energy substrate will achieve complete or partial wetting, depending on the liquid. Surface topography has been observed to assist or inhibit wetting depending on the scale of defects [32].

Membranes are permeable substrates which are used for a variety of applications such as wastewater treatment [123], desalination [124], in food technology [125], and in pharmaceutical industry [126]. These can be categorised on the basis of driving force of operation: (i) pressure driven involving microfiltration, ultrafiltration, nanofiltration and reverse osmosis, (ii) concentration driven involving pervaporation, forward osmosis and gas separation, (iii) elec-

tric potential gradient involving electrodialysis and electrofiltration, and (iv) temperature gradient involving distillation. It is widely believed that the hydrophilicity of membranes significantly affects its flux performance and the flux increases, in the water based feeds, as the membrane is more hydrophilic [127, 128]. The hydrophilicity of a substrate is measured by the static contact angle. In principle, if the static contact angle is less than 90°, the liquid-substrate combination is considered to be hydrophilic. The extent of a liquid spreading on a substrate depends on its hydrophilicity. The permeability of a substrate is characterized by lower equilibrium contact angle.

The dynamic wettability of a substrate is usually studied by considering a droplet spreading and imbibing on it. This is an example of a moving contact line problem which is studied using many approaches i.e. molecular kinetic theory, Lattice Boltzmann simulation, lubrication based approach [61, 63, 77, 92, 129, 130]. The contact line is prone to shear stress singularity which arises because of the breakdown of single-valuedness of velocity field. The spreading and imbibition of a droplet is considered using molecular kinetic theory and assuming Darcy's law for imbibition [129]. Molecular kinetic theory is valid for the equilibrium condition and describes the macroscopic contact angle by means of molecular characteristics i.e. jump frequency, jump length. In this study, even though the numerical predictions match well with experiments, there is significant difference in imbibition between low surface tension and high surface tension liquids. In another approach [77], Lattice Boltzmann simulation was used to study the absorption at the permeable substrate. This approach involves solving the discretised Boltzmann Equation on a lattice with fluid modelled as particle distribution. No-slip condition is used in the form of bounce-back condition to relieve stress singularity. This study is different from the previous one using molecular kinetic theory in the way the investigation was done at the pore level. Lubrication based approach has been extensively used to track the droplet interface as a function of time. This is achieved by solving a nonlinear partial differential equation (PDE) derived on the basis of Navier-Stokes Equation. In this approach, the contact line singularity may be relieved by using (i) slip models [92, 130] or (ii) precursor film assumption and disjoining pressure [61, 63]. The latter is more computationally efficient because one does not have to track the position of the contact line at every instant.

The primary motivation of this work is to relate the surface property of

membranes i.e. hydrophilicity realized through disjoining pressure to its numerical counterpart and predict the permeability of pressure-driven microporous membranes using dynamic contact angle measurements. The filtration test is performed to characterize permeability of membranes. This test is usually accomplished using either cross-flow setup [131–133] or dead end cell [134, 135]. However, these experimental setups are quite expensive and the test can be time-consuming as well which in turn slows down the membrane development process. The goal is to assess the permeability of a membrane using a droplet spreading and imbibing on the membrane surface. This is followed by comparison with the conventional method of calculating permeability using filtration test.

In the present chapter, the spreading and imbibition dynamics of an axisymmetric droplet on membranes is investigated using the mathematical model based on precursor film assumption [63]. A lubrication based approach is employed to study the evolution of droplet interface with time. The contact line singularity is relieved using precursor film assumption and disjoining pressure. The disjoining pressure is a combination of repulsive and attractive intermolecular forces. The disjoining pressure calculated from experiments is also found to be related to its numerical value in the case of apolar and polar interactions. The imbibition condition is derived from Darcy's law and thus, removes the need for thickness dependent permeability. The characteristic parameters (radius and height of droplet) are selected at the equilibrium stage of the dynamic contact angle measurement. The effective permeability is defined in terms of the non-dimensional imbibition coefficient along with the characteristic parameters at the equilibrium stage. On the other hand, the hydrodynamic permeability is defined in terms of the cross-sectional thickness of the membrane obtained from SEM image and the resistance obtained from the filtration test using dead-end cell. Finally, a comparison is made between the two calculated permeabilities.

3.2 Experiments

3.2.1 Membrane Fabrication

PES (Polyethersulfone, 58 kDa; BASF SE, Ludwigschafen, Germany) membranes were prepared by Phase Inversion method with DMA (Dimethylacetamide, Fisher Chemicals, New Jersey, USA) and water as solvent and non-

solvent, respectively. The additive used was PVP (Polyvinylpyrrolidone, 360 kDa; Sigma-Aldrich, St. Louis, MO, USA). The polymer, additive and solvent were added to a 50 mL beaker with different weight percentage and the solutions were stirred at 100 rpm at room temperature. The solutions were then removed from magnetic stirrer after 24 hours and let static for another 24 hours to let air bubbles disappear. Phase inversion (immersion precipitation) is the most widely used technique for asymmetric porous membrane fabrication, through which the polymer is transformed from a solution to a solid state. A schematic diagram of the phase inversion process is presented in Fig. 3.1(a). The casting solution was cast on a glass support with 400 μm thickness by a film applicator, then the support was immersed into the coagulation bath containing the non-solvent material (de-mineralized water) for 1 hour. The fabrication temperature was based on the coagulation bath temperature at the moment the support was immersed into the bath. During the fabrication process, the coagulation bath is naturally cooled down to room temperature. Two different membranes were fabricated with 10wt.% PES and PVP (1wt.% and 2wt.%), which for brevity will be referred as membrane PES_L1 and PES_L2, respectively.

Spin coating is a process where a thin layer is created on a laboratory glass slide using the casting solution. This thin layer has similar surface property as the fabricated membrane. This technique is primarily used to forgo the effect of permeation. The casting solution is poured in small quantity on a laboratory glass slide. The slide is then placed on the disk of the spin coating system (Spincoat G3P-15, Spin Coating Systems, Indiana, USA). The disk is spun at 4000 rpm for 90 seconds which ensures that the solution has formed a thin layer on the slide.

In addition, two commercial PES membranes (Sterlitech Corporation, USA) with nominal pore size 0.2 μm and 0.03 μm, respectively is used. Again, for brevity, these will be referred as membrane PES_C1 and PES_C2, respectively. The commercial membranes are generally more hydrophilic than the lab-fabricated membranes, owing to surface treatments like UV radiation, oxygen plasma, or ozonization.

3.2.2 Membrane filtration

The flux tests were performed using a dead-end cell device. The test setup is shown in Fig. 3.1(b). The resistance of a microporous membrane is made up

of three major components: the hydrodynamic resistance of the membrane in the absence of foulants, the resistance due to the accumulation of ions at the membrane surface (concentration polarization), and the resistance due to the accumulation of colloids at the membrane surface (cake layer fouling). The hydrodynamic resistance of the membrane itself in the absence of foulants is determined by measuring flow and pressure over time through the membrane using pure water and calculating the pure water flux. Membrane resistance is then calculated using Darcy's law as follows [136–138]:

$$J = \frac{1}{\mu R_m}\Delta p \tag{3.1}$$

where J is the pure water flux through membrane expressed in LMH (L/m^{2}h or m/s), Δp is transmembrane or applied pressure, and μ is dynamic viscosity of the permeate. The flux performance of the membranes as a function of transmembrane pressure is shown in Fig. 3.2.

3.2.3 SEM data

The surface morphology and cross section of the membranes was examined using a Scanning Electron Microscope (SEM, Zeiss Sigma 300 VP). All membranes were coated with gold and imaged at 30,000X magnification. The surface and cross-sectional images of the membranes are shown in Figs. 3.3 and 3.4 respectively.

3.2.4 AFM data

The surface topography of the membranes was examined with Atomic Force Microscopy (AFM, Bruker Dimension Icon, USA). An area of 10 μm x 10 μm of the membranes was scanned three times using tapping-mode at a scanning rate of 1.0 Hz at ambient temperature and humidity. Table 3.1 lists the mean roughness (Ra) and root mean squared roughness (Rq) values of the membranes. The nature of topography of the membranes are shown in Fig. 3.5.

3.2.5 Droplet spreading and imbibition

A commercial instrument (DSA100, KRUSS GmbH, Hamburg, Germany) was used for measuring the droplet radius and dynamic contact angle. A schematic of the experimental setup is presented in Fig. 3.6. A 2μL de-ionized water

Membrane sample	Mean roughness, Ra (nm)	Root mean squared roughness, Rq (nm)
C1	37.1	47.4
C2	61.1	82.1
L1	13.776	3.588
L2	23.334	4.897

Table 3.1: Surface roughness of different membranes

Parameter	Water	Diiodomethane (DIM)	Glycerol
Density of liquid, ρ (kg/m^3)	1000	3306	1260
Dynamic viscosity of liquid, μ (kg/m/s)	0.001	0.0026	0.0014
Surface tension of liquid, σ_L (mN/m)	72.8	50.8	64
Apolar component of surface tension of liquid, σ_L^{LW} (mN/m)	21.8	50.8	34
Acid (electron acceptor) parameter of liquid, σ_L^+ (mN/m)	25.5	0.0	3.92
Base (electron donor) parameter of liquid, σ_L^- (mN/m)	25.5	0.0	57.4

Table 3.2: Properties of different liquids.

droplet was generated using a syringe and deposited on the membrane. The syringe was controlled by a software, ADVANCE, provided with the instrument. A high speed video camera (upto 1000 fps) was used to record the video, the time the droplet detaches from the needle till complete imbibition. The sessile droplet orientation combined with elliptical fitting method and automatic baseline detection was used to generate droplet radius and contact angle as a function of time. The measurements are repeated 3-5 times on each membrane. The droplet radius and contact angle results are presented in Figs. 3.7 and 3.8. The different stages of droplet spreading and imbibition as recorded are shown in Fig. 3.9.

3.3   Mathematical Formulation

An axi-symmetric, incompressible, Newtonian liquid droplet with constant density ρ, dynamic viscosity, μ and surface tension, σ is considered to spread and imbibe on a smooth, horizontal permeable substrate (Fig. 3.10). The governing equations are presented in cylindrical coordinates.

3.3.1   Governing Equations

The pressure, p and velocity field, $\mathbf{v} = (u, w)$ is used to describe the spreading phenomenon. The continuity equation and Navier-Stokes equations are:

$$\frac{1}{r}\frac{\partial}{\partial r}(ru) + \frac{\partial w}{\partial z} = 0 \tag{3.2}$$

r-momentum equation:

$$\rho\left(\frac{\partial u}{\partial t} + u\frac{\partial u}{\partial r} + w\frac{\partial u}{\partial z}\right) = -\frac{\partial p}{\partial r} + \mu\left\{\frac{1}{r}\frac{\partial}{\partial r}\left(r\frac{\partial u}{\partial r}\right) - \frac{u}{r^2} + \frac{\partial^2 u}{\partial z^2}\right\} \tag{3.3}$$

z-momentum equation:

$$\rho\left(\frac{\partial w}{\partial t} + u\frac{\partial w}{\partial r} + w\frac{\partial w}{\partial z}\right) = -\frac{\partial p}{\partial z} + \rho g + \mu\left\{\frac{1}{r}\frac{\partial}{\partial r}\left(r\frac{\partial w}{\partial r}\right) + \frac{\partial^2 w}{\partial z^2}\right\} \tag{3.4}$$

where g is the acceleration due to gravity.

3.3.2   Boundary Conditions

At the liquid-vapor interface, $z = h(r, t)$, the kinematic condition is:

$$w = \frac{\partial h}{\partial t} + u\frac{\partial h}{\partial r} \tag{3.5}$$

50

The normal and tangential component of interfacial stress balance is:

$$\hat{\mathbf{n}}.\mathbf{T}.\hat{\mathbf{n}} = 2H\sigma - \Pi, \ \hat{\mathbf{t}}.\mathbf{T}.\hat{\mathbf{n}} = t.\nabla\sigma \tag{3.6}$$

where $\mathbf{T} = \mu(\nabla u + \nabla u^T)$ is the viscous stress of the liquid, $\hat{\mathbf{n}}$ and $\hat{\mathbf{t}}$ are unit vector normal and tangential to the liquid-vapor interface respectively which are defined as follows:

$$\hat{\mathbf{n}} = \frac{(-\frac{\partial h}{\partial r}, 1)}{\sqrt{1 + (\frac{\partial h}{\partial r})^2}}, \hat{\mathbf{t}} = \frac{(1, \frac{\partial h}{\partial r})}{\sqrt{1 + (\frac{\partial h}{\partial r})^2}} \tag{3.7}$$

The curvature of the substrate, H is given by

$$2H = -(\frac{\partial^2 h}{\partial r^2} + \frac{1}{r}\frac{\partial h}{\partial r}) \tag{3.8}$$

A two-term disjoining pressure, Π [59, 99] takes the following form and is used to alleviate the shear stress singularity.

$$\Pi = A\left[(\frac{b}{h})^n - (\frac{b}{h})^m\right] \tag{3.9}$$

where $A \geq 0$ is the disjoining pressure parameter and exponents, $(n, m) = (3, 2)$ are constant and b is the precursor film thickness. The value of A is associated with the equilibrium contact angle, θ_{eq} [99]:

$$A = \frac{(n-1)(m-1)}{b(n-m)}\sigma(1 - cos\theta_{eq}) \tag{3.10}$$

At the liquid-substrate interface, $z = 0$, the imbibition condition is defined:

$$w = -\frac{\kappa}{\mu}p \tag{3.11}$$

where κ is the proportionality constant with similar property as defined previously [63, 98]. Finally, the no-slip condition is used.

$$u = 0 \tag{3.12}$$

Since the spreading is axi-symmetric in nature, the following conditions are used:

$$\frac{\partial h}{\partial r}\Big|_{r=0} = 0, \frac{\partial^3 h}{\partial r^3}\Big|_{r=0} = 0 \tag{3.13}$$

For droplet volume conservation,

$$\int_0^{r_0} 2\pi r h(r)dr = V_0 + \pi b r_0^2 \tag{3.14}$$

where subscript 0 is used to represent the initial value of a physical quantity and πb is the correction factor for precursor film thickness.

51

3.3.3 Scalings

The governing equations and the corresponding boundary conditions are non-dimensionalized using the following:

$$r = l\tilde{r}, z = h\tilde{z}, u = u_{sc}\tilde{u}, w = \epsilon u_{sc}\tilde{w}$$

$$t = \frac{l}{u_{sc}}\tilde{t}, p = p_{sc}\tilde{p}, \Pi = p_{sc}\tilde{\Pi} \tag{3.15}$$

where $u_{sc} = \frac{\epsilon^3\sigma}{3\mu}$, $p_{sc} = \frac{h\sigma}{l^2}$, $b = h\tilde{b}$, $\epsilon = \frac{h}{l}$, and $\kappa = \frac{dh^3}{3l^2}\tilde{\kappa}$ represent the characteristic spreading speed, the pressure scale, the precursor film thickness, the lubrication ratio, and the effective permeability for thickness, d of the substrate, respectively. Tilde is used to denote the non-dimensional nature of a physical quantity. In the lubrication limit, the governing equations and boundary conditions can be written in the following form:

Continuity equation:

$$\frac{\partial \tilde{w}}{\partial \tilde{z}} + \frac{1}{\tilde{r}}\frac{\partial(\tilde{r}\tilde{u})}{\partial \tilde{r}} = 0, \tag{3.16}$$

r-momentum equation:

$$\frac{\partial^2 \tilde{u}}{\partial \tilde{z}^2} - 3\frac{\partial \tilde{p}}{\partial \tilde{r}} = 0, \tag{3.17}$$

z-momentum equation:

$$-\frac{\partial \tilde{p}}{\partial \tilde{z}} - B = 0 \tag{3.18}$$

where $B(= \frac{l^2\rho g}{\sigma})$ is the Bond number.

At $\tilde{z} = \tilde{h}(\tilde{r}, \tilde{t})$, the kinematic condition is:

$$\tilde{w} = \frac{\partial \tilde{h}}{\partial \tilde{t}} + u\frac{\partial \tilde{h}}{\partial \tilde{r}}, \tag{3.19}$$

The normal and tangential component of interfacial stress balance is:

$$\tilde{p} = -\left(\frac{\partial^2 \tilde{h}}{\partial \tilde{r}^2} + \frac{1}{\tilde{r}}\frac{\partial \tilde{h}}{\partial \tilde{r}}\right) - \tilde{A}\left[\left(\frac{\tilde{b}}{\tilde{h}}\right)^3 - \left(\frac{\tilde{b}}{\tilde{h}}\right)^2\right], \tag{3.20}$$

$$\frac{\partial \tilde{u}}{\partial \tilde{z}} = 0 \tag{3.21}$$

At $\tilde{z} = \tilde{b}$, the imbibition condition is:

$$\tilde{w} = -\frac{\tilde{\kappa}}{\mu d}\tilde{p} \tag{3.22}$$

At $\tilde{z} = 0$, the no-slip condition is:

$$\tilde{u} = 0 \tag{3.23}$$

3.3.4 Evolution Equation

The following non-dimensional time evolution equation of droplet height is obtained from the governing eqns. 3.16-3.18 with the help of boundary conditions (3.19-3.23).

$$\frac{\partial \tilde{h}}{\partial \tilde{t}} = \frac{1}{\tilde{r}}\frac{\partial}{\partial \tilde{r}}\left\{\tilde{r}\tilde{h}^3\frac{\partial}{\partial \tilde{r}}\left(B\tilde{h}-\tilde{\Pi}-\frac{\partial^2 \tilde{h}}{\partial \tilde{r}^2}-\frac{1}{\tilde{r}}\frac{\partial \tilde{h}}{\partial \tilde{r}}\right)\right\} - \tilde{\kappa}\left\{B(\tilde{h}-\tilde{b})-\tilde{\Pi}-\frac{\partial^2 \tilde{h}}{\partial \tilde{r}^2}-\frac{1}{\tilde{r}}\frac{\partial \tilde{h}}{\partial \tilde{r}}\right\}$$
$$(3.24)$$

$$\frac{\partial \tilde{h}}{\partial \tilde{r}}(0,\tilde{t})=0, \tilde{h}(L,\tilde{t})=\tilde{b}, \frac{\partial^3 h}{\partial \tilde{r}^3}(0,\tilde{t})=0, \frac{\partial \tilde{h}}{\partial \tilde{r}}(L,\tilde{t})=0. \qquad (3.25)$$

This nonlinear PDE is solved numerically subject to the boundary conditions (3.25). A fourth-degree polynomial which satisfies the boundary conditions (3.25) is used as the initial droplet profile. The spherical-cap approximation is used to calculate the volume of the droplet. The non-dimensional parameters, r_0 and V_0 are obtained by selecting the dimensional values at the equilibrium stage. The size of the computational domain, L is 4 with 625 points per unit length. The second-order finite difference method is used to discretise the spatial derivatives which converts the equation into sets of differential algebraic equations (DAEs). An adaptive time-step solver, DASSL is used, which is found in SLATEC library. The apparent contact angle is found by calculating the maximum slope of the interface at each time step.

3.4   Results and discussion

In order to make comparison with experimental data, the characteristic parameters, (l,h) are selected at the initial and at the onset of equilibrium stage. The normalising factors based on equilibrium stage is comparatively more appropriate since the disjoining pressure parameter is accurately predictable [139]. The precursor film thickness is considered to be less than <1 μm. The modified disjoining pressure, A is calculated theoretically using the relation (3.10) and based on scaling relation, the disjoining pressure parameter, $\tilde{A}$ is obtained. This enables prediction of the equilibrium stage of the process with an accuracy of 95%. The non-dimensional imbibition coefficient, $\tilde{\kappa}$ is varied so as to match the trend from experiments. The effective permeability, κ is calculated on the basis of scaling relation.

3.4.1 Apolar interaction: Verification of disjoining pressure in the case of spreading

In the mathematical model employed, the disjoining pressure is used to account for the repulsive and attractive interactions of the liquid with the substrate. Also, it is feasible to predict the nature of interaction through the spreading coefficient, S which explicitly defines the interfacial tension of each component in the system with respect to the other.

Consider the spreading of diiodomethane (DIM) on a laboratory glass slide (Fig. 3.11). DIM is known to possess only apolar component. Air is apolar in nature and glass is a polar molecule. For the sake of simplicity, the first step is to neglect polar interactions which is possible only when the liquid and one of the bounding media are completely apolar [140]. Thus, the spreading of DIM on glass slide can be considered to be an apolar interaction. The primary equation of the most widely used Fowkes' surface energy theory [141] is

$$(\sigma_L^{LW})^{1/2}(\sigma_S^{LW})^{1/2} + (\sigma_L^{P})^{1/2}(\sigma_S^{P})^{1/2} = \sigma_L(\frac{1+cos\theta}{2}) \qquad (3.26)$$

where the subscripts L and S denote liquid and solid phase respectively, superscripts LW and P indicate apolar, Lifshitz-van der Waals' component and polar component of spreading coefficient respectively, and θ represents the contact angle between the liquid and the solid. In the absence of polar interactions, eqn. 3.26 reduces to

$$\sigma_S^{LW} = \sigma_L(\frac{1+cos\theta}{2})^2 \qquad (3.27)$$

The apolar, Lifshitz-van der Waals' component of spreading coefficient is defined as

$$S^{LW} = \sigma_S^{LW} - (\sigma_{SL}^{LW} + \sigma_L^{LW}) \qquad (3.28)$$

The well known Fowkes' combining rule is given by

$$\sigma_{ij}^{LW} = [(\sigma_i^{LW})^{1/2} - (\sigma_j^{LW})^{1/2}]^2 \qquad (3.29)$$

Using eqn. 3.29, the spreading coefficient may be rewritten as

$$S^{LW} = 2(\sigma_L^{LW})^{1/2}((\sigma_S^{LW})^{1/2} - (\sigma_L^{LW})^{1/2}) \qquad (3.30)$$

b (nm)	$\tilde{b}$ (-)	$\tilde{A}$ (-)	Π (N/m^2)	Ratio= $\left\|\frac{\Pi}{\phi^{LW}}\right\|$
424	0.001	$\frac{1}{\tilde{b}}$	-0.0585	0.94
212	0.0005	$\frac{0.95}{\tilde{b}}$	-0.0284	0.457
84.8	0.0002	$\frac{0.78}{\tilde{b}}$	-0.00929	0.149

Table 3.3: A comparison of the experimental and numerical disjoining pressure for DIM spreading on laboratory glass slide.

The energy per unit volume i.e. disjoining pressure of the film is expressed as

$$\phi^{LW} = -2S^{LW}\left(\frac{d_0^2}{h^3}\right) \tag{3.31}$$

where d_0=0.158 nm is the equilibrium distance because of extremely short-range Born repulsion and h is the liquid thickness at equilibrium.

In the present case, the volume of DIM used is 1 μL. The equilibrium contact angle is 45^0. From eqns. 3.27 and 3.30, $\sigma_S^{LW}=$ 37 mN/m and $S^{LW}=$ -14.891 mN/m, respectively. At the equilibrium stage, using spherical cap approximation, the radius and height of the droplet is 1.2 mm and 0.424 mm respectively. This yields $\phi^{LW} = 0.06217$ N/m^2. Based on the characteristic values, p_{sc} is found to be 14.958 N/m^2. From Fig. 3.12, it is evident that the mathematical model based on precursor film approximation is able to predict the dynamic radius and contact angle for different $\tilde{b}$.

Table 3.3 lists precursor film thickness along with other non-dimensional constants obtained to predict the equilibrium behavior. There occurs qualitative agreement between the theoretically calculated ϕ^{LW} and the numerical value, Π. For smaller values of precursor film thickness, the mathematical model tends to underestimate the disjoining pressure. The apparent mismatch in sign of disjoining pressure suggests a possible reversal of its nature which the mathematical model is unable to perceive.

3.4.2 Polar interaction: Verification of disjoining pressure in the case of spreading

Consider the spreading of water droplet on spin-coated composition of membrane L2 (Fig. 3.13). This liquid-substrate combination is a perfect example of polar interaction since water is a polar liquid and the L2 composition has well-defined polarity. Spin-coating is a common technique used to understand the hydrophilic nature of membranes since it negates the effect of permeation.

For polar interactions, it is necessary to establish the acid and base component of interfacial tension of solid. This can be accomplished with the help of van Oss theory. The primary equation of van Oss theory [142] is

$$(\sigma_L^{LW})^{1/2}(\sigma_S^{LW})^{1/2} + (\sigma_L^-)^{1/2}(\sigma_S^+)^{1/2} + (\sigma_L^+)^{1/2}(\sigma_S^-)^{1/2} = \sigma_L(\frac{1+cos\theta}{2}) \quad (3.32)$$

where the quantities with superscript $+, -$ denote the acid and base component of interfacial tensions, respectively.

The first step is to calculate the apolar component of interfacial tension of solid, σ_S^{LW} by setting $\sigma_S^+ = \sigma_S^- = 0$. This yields

$$\sigma_S^{LW} = \sigma_L(\frac{1+cos\theta}{2})^2 \quad (3.33)$$

DIM is used since it only possesses apolar component. From Table 3.4, the equilibrium contact angle of DIM spreading on L2 coating is 23.14°. This yields $\sigma_S^{LW} = 46.8$ mN/m.

The next step is to determine the acid and base components of the interfacial tension of solid. In order to determine the acid component, glycerol is used because it has a strong base component. The primary equation in this case reduces to

$$(\sigma_L^{LW})^{1/2}(\sigma_S^{LW})^{1/2} + (\sigma_L^-)^{1/2}(\sigma_S^+)^{1/2} = \sigma_L(\frac{1+cos\theta}{2}) \quad (3.34)$$

From Table 3.4, using the equilibrium contact angle of glycerol on L2 coating, yields $\sigma_S^+ = 2.129$ mN/m.

The last step is to calculate the base component of interfacial tension of L2 coating. The primary equation in this case reduces to

$$(\sigma_L^{LW})^{1/2}(\sigma_S^{LW})^{1/2} + (\sigma_L^+)^{1/2}(\sigma_S^-)^{1/2} = \sigma_L(\frac{1+cos\theta}{2}) \quad (3.35)$$

For this purpose, considering the equilibrium contact angle of water spreading on L2 coating (Table 3.4), yields $\sigma_S^- = 26.304$ mN/m.

The apolar component of spreading coefficient, S^{LW} can be calculated using eqn. 3.33. The polar component of interfacial tension of solid due to acid-base interactions is given by

$$\sigma_S^P = 2(\sigma_S^+\sigma_S^-)^{1/2} \quad (3.36)$$

Liquid used	Equilibrium contact angle, θ
DIM	23.14°
Glycerol	53.68°
Water	52.65°

Table 3.4: Equilibrium contact angle of various liquids used on L2 coating for determining its interfacial tension.

The polar component of spreading coefficient, S^P is defined as

$$S^P = \sigma_S^P - (\sigma_{SL}^P + \sigma_L^P) \tag{3.37}$$

where $\sigma_{SL}^P = 2[(\sigma_S^+)^{1/2}\text{-}(\sigma_L^+)^{1/2}] \, [(\sigma_S^-)^{1/2}\text{-}(\sigma_L^-)^{1/2}]$ and $\sigma_L^P = 51.0$ mN/m (for water).

The disjoining pressure is a combination of apolar and polar components [140].

$$\phi^{LW+P} = \phi^{LW} + \phi^P = -2S^{LW}(\frac{d_0^2}{h^3}) - \frac{S^P}{l}exp(\frac{d_0 - h}{l}) \tag{3.38}$$

where $l(=1\ nm)$ is the correlation length for water.

For water droplet spreading on L2 coating, S^{LW}=20.282 mN/m, S^P=37.059 mN/m, and ϕ^{LW+P}=-0.0306 mN/m^2.

The mathematical model accurately predicts the dynamic droplet radius and contact angle (Fig. 3.14). Based on the simulation parameters, $p_{sc} = 44.307$ N/m^2 and $\tilde{A} = \frac{1.5}{\tilde{b}}$. This yields Π = -0.1754 N/m^2. The ratio $\frac{\Pi}{\phi^{LW+P}} = 5.732$ which falls within one order-of-magnitude. Thus, for polar interactions, the mathematical model predicts the theoretical disjoining pressure quite accurately.

3.4.3 Preliminary Results of Membrane Morphology and Characterization

SEM analysis is an important technique for microscopic observation of the membrane morphology. It provides information about various structural elements such as thickness, presence of dense skin layer, symmetric/asymmetry in the structure and length as well as width of macrovoids. Cross-sectional analysis by SEM images is carried out to obtain qualitative information regarding morphology of the fabricated and commercial membranes. The surface and cross-sectionl SEM images are shown in Figs. 3.3 and 3.4 respectively. In

the case of lab-fabricated membranes, due to high mutual affinity of DMA for water, instantaneous demixing happened during phase inversion, resulting in formation of finger type macropores [143].

The flux results have been illustrated in Fig. 3.2. These results were obtained using dead-end cell device at different transmembrane pressures for each membrane. The results show that pressure increase results in flux increase. For the lab-fabricated membranes, increasing PVP decreases the porosity of the membranes. For the commercial membranes, the flux values are higher for PES_C1 compared to PES_C2. This is because the predominant pore size is 0.2 μm in PES_C1 compared to 0.03 μm in PES_C2. In general, a membrane consists of a distribution of pore sizes.

The results for contact angle of de-ionized water droplets on membranes are presented in Figs. 3.7 and 3.8. In general, lower contact angle indicates more hydrophilic membrane surface [144, 145]. For the lab-fabricated membranes, dynamic contact angle measurements indicate that increasing PVP percentage increases hydrophilicity of the membranes. However, it was observed that the water droplets penetrated through the membrane more slowly by increasing the PVP percentage. Thus, the global effect through filtration test is realized by a droplet locally. The spreading and imbibition phenomena of water droplet on the membrane surface was observed in the following stages (Fig. 3.9): (i) The lubrication approximation is valid at $t = 0$. The droplet spreads momentarily, (ii) The spreading is halted and the contact line is pinned. The droplet volume begins to shrink at $t = 18$ s, (iii) The contact line retraction begins marking the onset of equilibrium at $t = 30$ s, and (iv) The droplet vanishes completely, therefore it is completely imbibed by the membrane.

3.4.4 Comparison with experiments in case of spreading and imbibition

The droplet spreads to an extent and stops. The volume begins to shrink with no movement of the contact line. This is referred as contact line pinning. Due to continuous imbibition of the droplet, the contact line eventually retracts and thus, marks the onset of equilibrium stage. Contact line pinning can arise because of physico-chemical interactions or substrate topography or both. The mechanism of spreading and imbibition on the membranes can be explained as follows: The droplet detaches from the needle due to the surface energy of the membrane. As a result, the droplet hits the surface with a very small

Weber number. This means that the deformation due to gravity upon hitting the surface of the membrane is negligible. The initial stage is dominated by spreading which depends on the hydrophilic nature of the liquid-substrate combination. For the present cases, it is evident that spreading happens only for a very short period of time. During spreading, the contact line is mobile and this reduces the droplet height. Post-spreading regime is dictated by imbibition which is observed when the contact line is pinned. The volume of the droplet shrinks with time, followed by complete retraction of the contact line. The retraction of the contact line is non-uniform, signifying the fact that the surface topography is influential (Fig. 3.9).

Contact line pinning is reproduced by introduction of a defect [63]. In order to accurately assess the impact of defects on the pinning behaviour, the nonlinear evolution equation is modified and it takes the following form:

$$\frac{\partial \tilde{h}}{\partial \tilde{t}} = \frac{1}{\tilde{r}} \frac{\partial}{\partial \tilde{r}} \left\{ \tilde{r} \tilde{h}^3 \frac{\partial}{\partial \tilde{r}} \left(B(\tilde{h} + \tilde{\gamma}) - \tilde{\Pi} - \frac{\partial^2 (\tilde{h} + \tilde{\gamma})}{\partial \tilde{r}^2} - \frac{1}{\tilde{r}} \frac{\partial (\tilde{h} + \tilde{\gamma})}{\partial \tilde{r}} \right) \right\}$$
$$- \tilde{\kappa} \left\{ B(\tilde{h} - \tilde{b}) - \tilde{\Pi} - \frac{\partial^2 (\tilde{h} + \tilde{\gamma})}{\partial \tilde{r}^2} - \frac{1}{\tilde{r}} \frac{\partial (\tilde{h} + \tilde{\gamma})}{\partial \tilde{r}} \right\} \quad (3.39)$$

where $\tilde{\gamma}$ is a shape function.

A defect in the form of a Gaussian shape function, is considered. The following equation describes the defect:

$$\tilde{\gamma}(\tilde{r}) = -\tilde{r}_1 exp \left(- \frac{(\tilde{r} - \tilde{r}_{loc})^2}{2 \tilde{r}_2^2} \right) \quad (3.40)$$

where $\tilde{r}_{loc}$ denotes the location of the defect. The apparent contact angle in the presence of defects is calculated using the relation [63]:

$$tan(\theta) = \frac{\tilde{h}_{\tilde{r}}}{1 + (\tilde{h}_{\tilde{r}} + \tilde{\gamma}_{\tilde{r}}) \tilde{\gamma}_{\tilde{r}}} \quad (3.41)$$

In Fig. 3.11, a comparison is made between experimental data and numerical predictions of water droplet spreading and imbibition on membrane PES_C1. The characteristic values selected at the onset of equilibrium stage are $l = 1.4$ mm and $h = 0.07$ mm. The value $\tilde{b} = 0.004$ is chosen, consistent with previous studies [63, 99]. In order to match the equilibrium stage, $\tilde{A}(= \frac{0.4}{\tilde{b}})$ is obtained. The simulation was first performed only in the presence of imbibition. Later, a Gaussian defect ($\tilde{r}_1 = 10 \ \tilde{b}$, $\tilde{r}_2 = 10 \ \tilde{b}$) was placed at

$\tilde{r}_{loc} = 1.22$, without changing the imbibition coefficient, $\tilde{\kappa}$. It is evident that a single defect very accurately reproduces the pinning behavior in both the dynamic radius and contact angle behavior. Pinning is usually interpreted as a constant radius regime with linear decrease in contact angle. In addition, the presence of a defect also decreases the imbibition time. This happens because a defect halts the movement of the contact line. This causes the volume of the droplet to decrease rapidly. At a certain instant, the movement restarts but is not prolonged due to lack of enough volume.

The efficacy of the mathematical model to predict the pinning behavior was tested for a extensive range of imbibition time scale. In Fig. 3.12, the contact line is pinned for a longer duration (one order-of-magnitude longer) compared to Fig. 3.11. This is because the nominal pore size is only 0.03 μm in the latter case compared to 0.2 μm in the former. The smaller pore size and porosity of membrane PES_C2 ensures that the droplet stays longer on the surface. The numerical predictions match well with experimental data in the presence of a single defect.

The pinning time is further enhanced (two order-of-magnitude) when the droplet spreads and is imbibed by lab-fabricated membranes, PES_L1 and PES_L2. The significant increase in pinning time is because of less porosity of these membranes compared to the commercial ones. The extent of porosity can be inferred from the filtration test (Fig. 3.2). In both the cases (Figs. 3.13 and 3.14), the numerical predictions have an excellent agreement with experimental data in the presence of a single defect.

In the all the cases shown, the pinning behavior was reproduced using the mathematical model by assuming defect dimensions of the order of 1 μm. On the other hand, AFM surface roughness values of each membrane is of the order of 10 nm (see Table 3.1). This mismatch between the theoretical value of the Gaussian parameters used and the averaged value of surface roughness obtained from AFM data is because of the larger droplet volume chosen to study spreading and imbibition. A smaller droplet volume ($\sim n$L or lower) would ensure that the maximum spreading radius is close to the average roughness value (Ra). This can possibly provide detailed information about the role of substrate topography on the movement of the contact line and help to achieve better objectivity on the real cause of pinning.

Membrane sample	Imbibition time (s)	Effective permeability, κ (m^2)	Hydrodynamic permeability, $\frac{d}{R_m}$ (m^2)	Permeability ratio, $\kappa/\frac{d}{R_m}$
C1	0.3	10^{-11}	2.463x10^{-15}	4060.089
C2	5	5.489x10^{-13}	5.1x10^{-16}	1076.274
L1	30	1.628x10^{-13}	1.682x10^{-15}	96.789
L2	50	9.832x10^{-14}	4.076x10^{-16}	241.21

Table 3.5: The values of different permeabilities of each membrane sample.

3.4.5 Effective and Hydrodynamic Permeability

Using Darcy's law, the flux (J) through a membrane is directly proportional to the transmembrane pressure (Δp).

$$J \propto \Delta p \Rightarrow J = \frac{1}{\mu R_m}\Delta p \tag{3.42}$$

where R_m is the intrinsic resistance of the membrane during filtration. The intrinsic resistance of a membrane depends on the pore size distribution. The lesser the porosity, the less is the flux which implies higher intrinsic resistance.

The droplet imbibition condition on a permeable substrate is given by eqn. 3.11.

Since the direction of membrane flux is the same as imbibition, from eqns. 3.11 and 3.42, we have

$$\kappa = \frac{d}{R_m} \tag{3.43}$$

Thus, the effective permeability is related to the intrinsic resistance of the membrane through its cross-sectional thickness.

The effective permeability is calculated based on scalings after varying the non-dimensional imbibition coefficient ($\tilde{\kappa}$) until good agreement is found with experimental data. The cross-sectional thickness of the membrane (d) is obtained from SEM images. The intrinsic resistance of the membrane is given by the slope of the flux curve with respect to transmembrane pressure. Table 3.5 presents effective and hydrodynamic permeabilities of the membranes and a permeability ratio is calculated to understand the relative difference of each permeability.

The permeability ratio decreases as the imbibition time increases. The effective permeability studied through droplet spreading and imbibition has a linear nature. In other words, the smaller the imbibition time scale, the higher

Membrane sample	Permeability ratio, $\kappa / \frac{d}{R_m}$	Corrected Permeability ratio, $\epsilon^n \kappa / \frac{d}{R_m}$
C1	4060.089	0.478 (n=3)
C2	1076.274	0.475 (n=2)
L1	96.789	0.968 (n=1)
L2	241.21	2.25 (n=1)

Table 3.6: The values of different permeabilities of each membrane sample based on the correction factor.

the effective permeability. However, the nature of hydrodynamic permeability is quite complex. As is evident from the values, the relationship is nonlinear with respect to the imbibition time scale. The hydrodynamic permeability strongly depends on the transmembrane pressure, cross-sectional thickness, distribution of pore sizes and porosity.

In order to ensure that the permeability ratio falls within one order-of-magnitude based on the imbibition time scale, a correction factor is proposed on the calculation of effective permeability.

$$\epsilon^n \kappa = \frac{d}{R_m} \tag{3.44}$$

where $\epsilon = \frac{h}{l}$ is the lubrication ratio at the equilibrium stage and n is an integer. The choice of a lubrication ratio is quite critical for accurate prediction of droplet radius and contact angle.

For membranes PES_L1 and PES_L2, the imbibition time scale is of the order of 10 s. From Figs. 3.13 and 3.14, the lubrication ratio, ϵ is 0.01 and 0.00933, respectively. Choosing n=1 ensures that the permeability ratio is 0.968 and 2.25, respectively which is within an order-of-magnitude. Similarly, for PES_C2 and PES_C1 where the imbibition time scale is of the order of 1 s and 0.1 s respectively, choosing n=2 and n=3 yields permeability ratio as 0.475 and 0.478, respectively. This has been summarized in Table 3.6.

In conclusion, for an initial droplet volume (in the present case, 2 μL), the mathematical model can accurately predict the hydrodynamic permeability as long as the imbibition time scale is slow. It is expected that the correction factor would vanish for much slower time scale. For faster imbibition dynamics, the amplification of the effective permeability is poor because of the dependence of hydrodynamic permeability on the bulk. The apparent disconnect between the local nature (effective permeability) and the global nature (hy-

drodynamic permeability) can be understood in terms of the role of pressure. The capillary pressure experienced by a droplet on the membrane surface is much smaller compared to the external pressure which is utilized to obtain the resistance of the membrane.

3.5 Conclusion

The phenomena of droplet spreading and imbibition on microporous membranes was investigated using dynamic contact angle measurements and a mathematical model based on precursor film approximation. The theoretical disjoining pressure was also found to be related to its numerical value in the case of apolar and polar interactions. The effective permeability calculated from droplet imbibition was compared to its hydrodynamic permeability obtained from filtration test. A correction factor dependent on the imbibition time scale was proposed to bridge the gap between the two permeabilities.

This is a first study to highlight the ability of the mathematical model to relate the theoretical disjoining pressure to its numerical counterpart and capture the imbibition dynamics across a range of time scales. Even though the model underpredicts the disjoining pressure for apolar interactions, it offers qualitative agreement. The model accurately captures the pinning behavior for different imbibition time scales with the introduction of a Gaussian defect. However, the computationally estimated size of a defect is of the order of 1 μm which is much higher than the AFM surface roughness values. To input the AFM roughness value, the spreading and imbibition needs to be studied for much smaller droplet volumes, say of the order of 1 nL. This would provide more insight on the role of surface topography on the movement of the contact line. It would be worthwhile to study the imbibition dynamics on track-etched membranes. The specialty of track-etched membranes is that the pores are well defined capillaries with fixed dimensions. Thus, controlled pore distribution and smaller droplet volume can provide answer to the question: How topography causes pinning on permeable substrates?
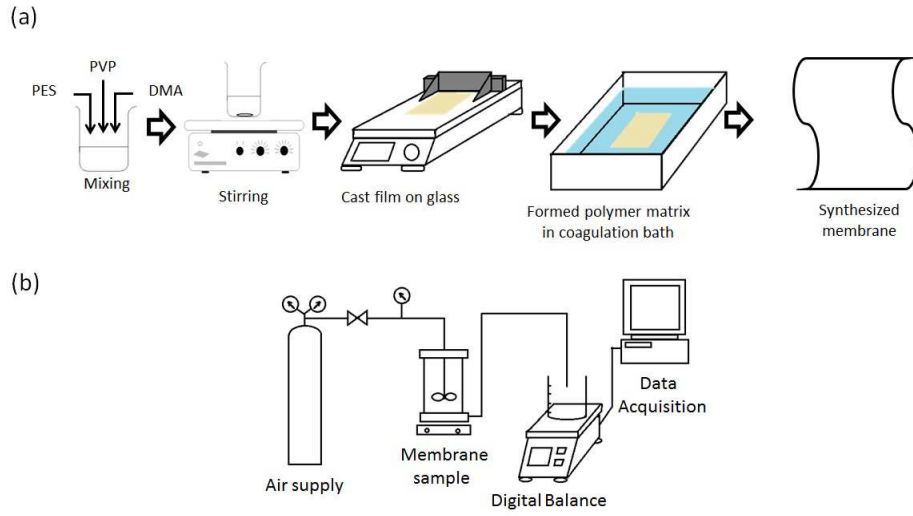
Figure 3.1: A schematic diagram of the (a) phase inversion process for fabrication of membranes and (b) test setup for filtration test of membranes.
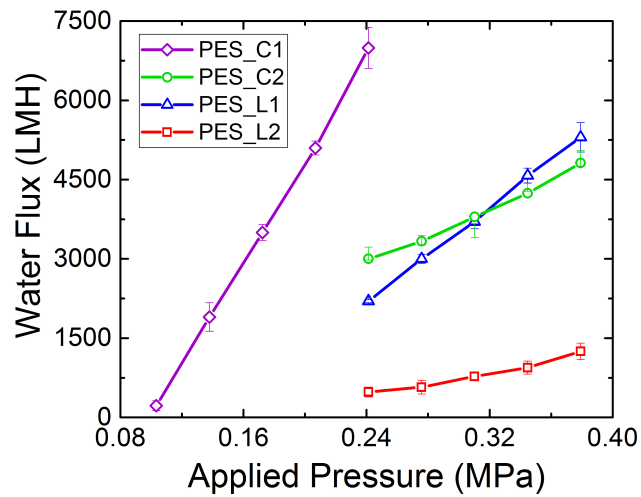
Figure 3.2: The flux performance of membranes as a function of transmembrane pressure.
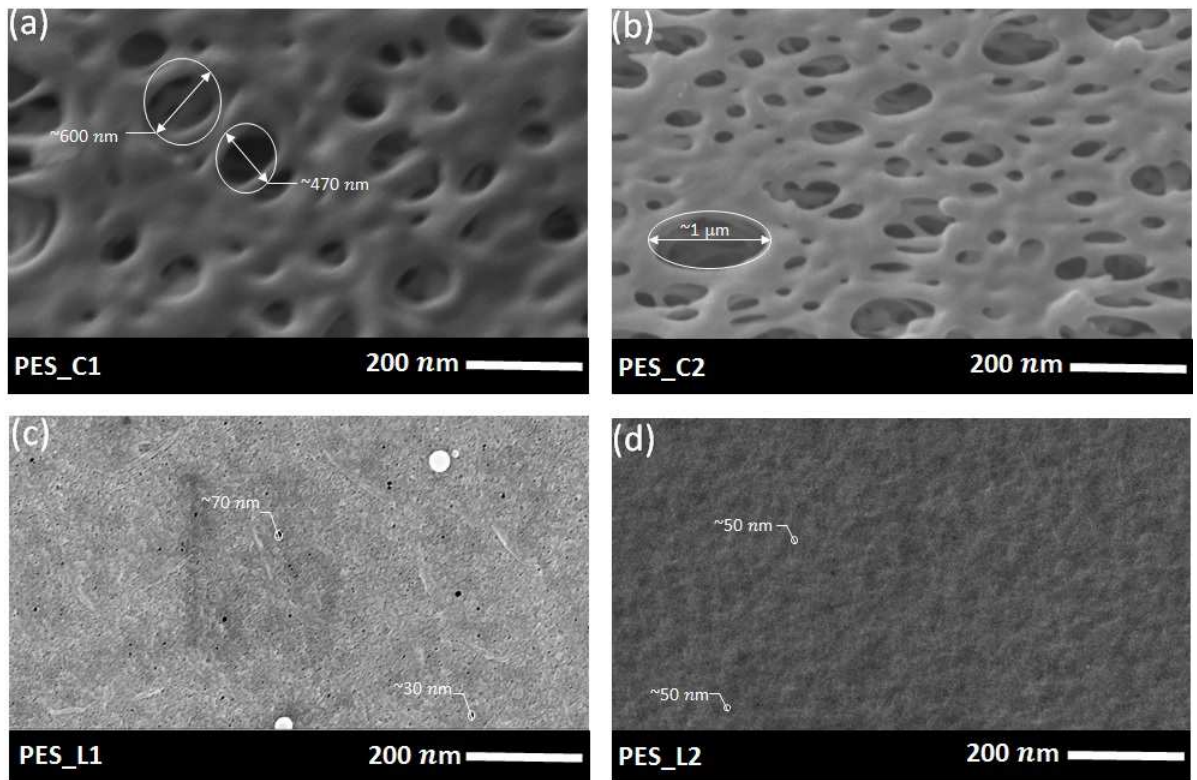
Figure 3.3: Surface SEM images of (a) PES_C1, (b) PES_C2, (c) PES_L1, and (d) PES_L2 membranes.
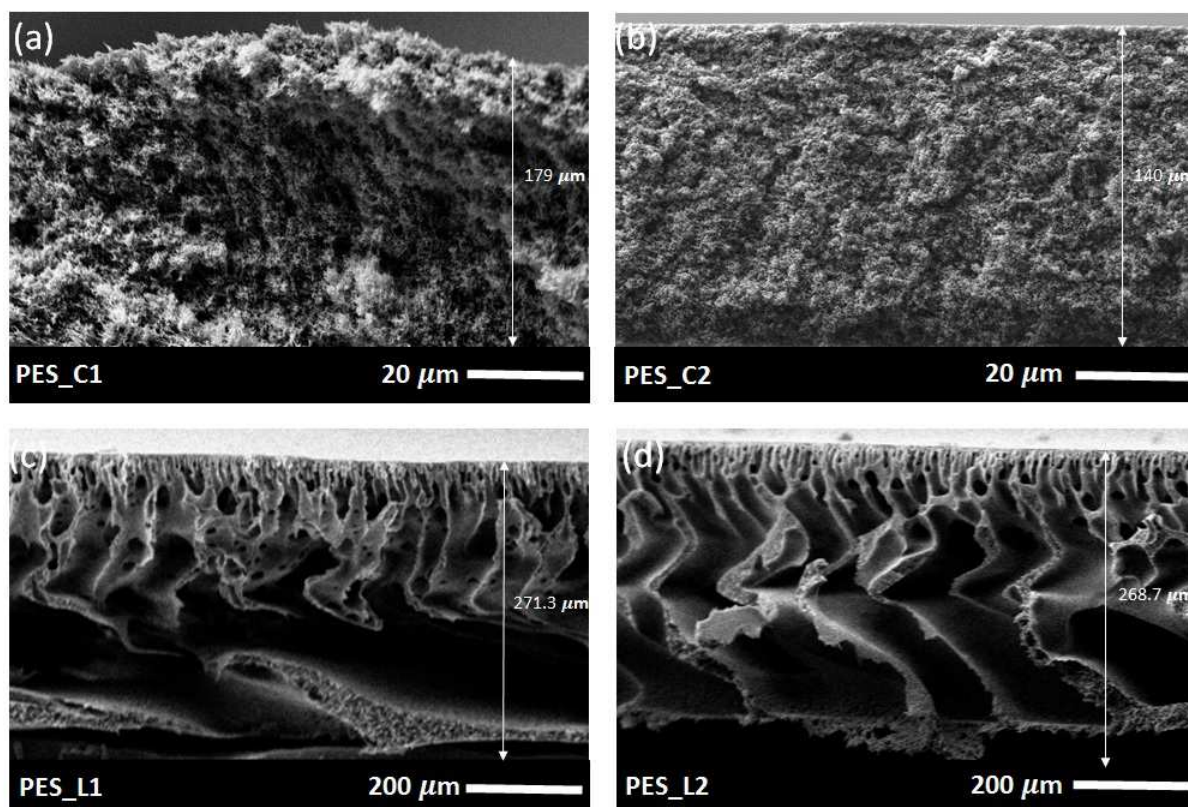
Figure 3.4: Cross-sectional SEM images of (a) PES_C1, (b) PES_C2, (c) PES_L1, and (d) PES_L2 membranes.
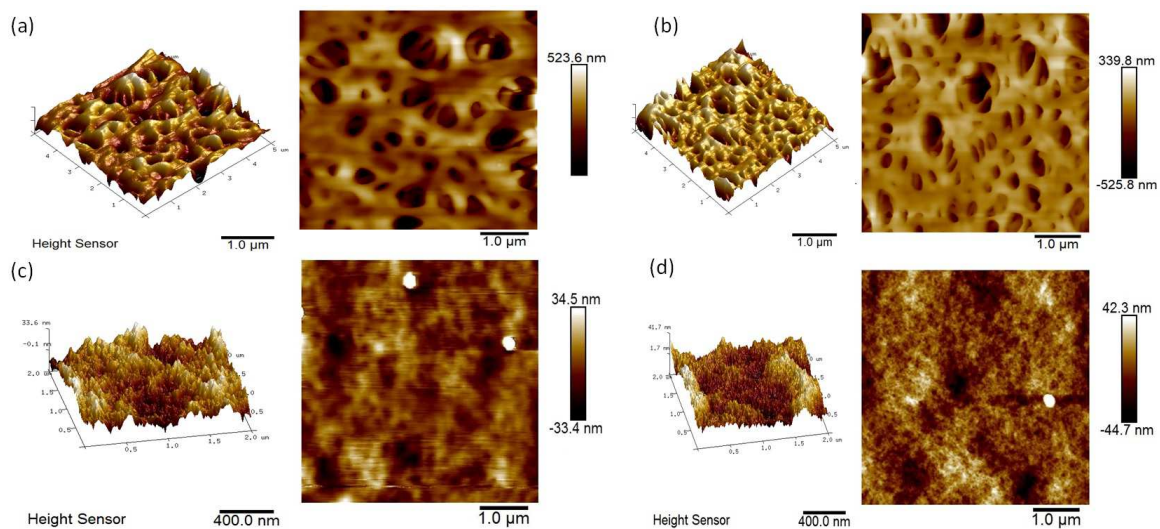
Figure 3.5: AFM surface roughness images of (a) PES_C1, (b) PES_C2, (c) PES_L1, and (d) PES_L2 membranes.
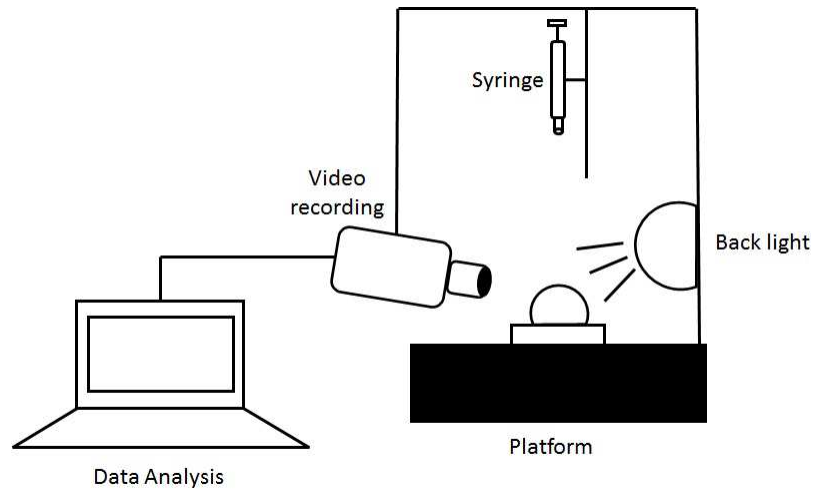
Figure 3.6: A schematic diagram of the commercial instrument, DSA100 used for measuring dynamic droplet radius and contact angle on impermeable/permeable substrate.
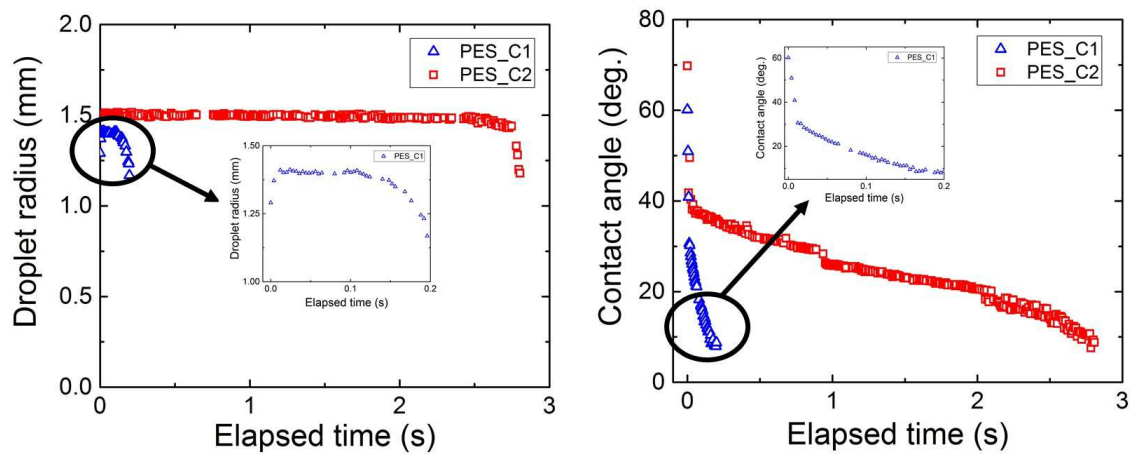
Figure 3.7: Dynamic radius and contact angle measurements of de-ionized water droplet spreading and imbibition on PES_C1 and PES_C2 membranes.
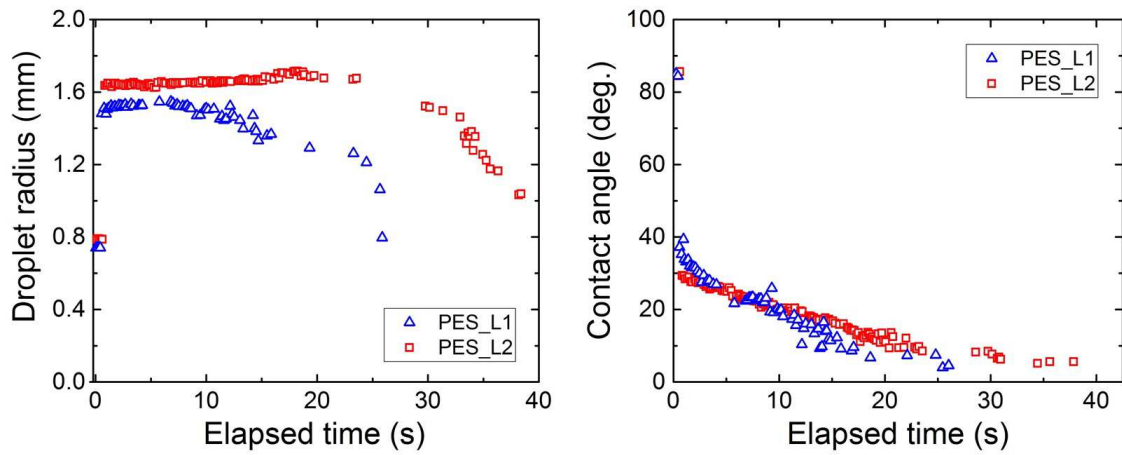
Figure 3.8: Dynamic radius and contact angle measurements of de-ionized water droplet spreading and imbibition on PES_L1 and PES_L2 membranes.
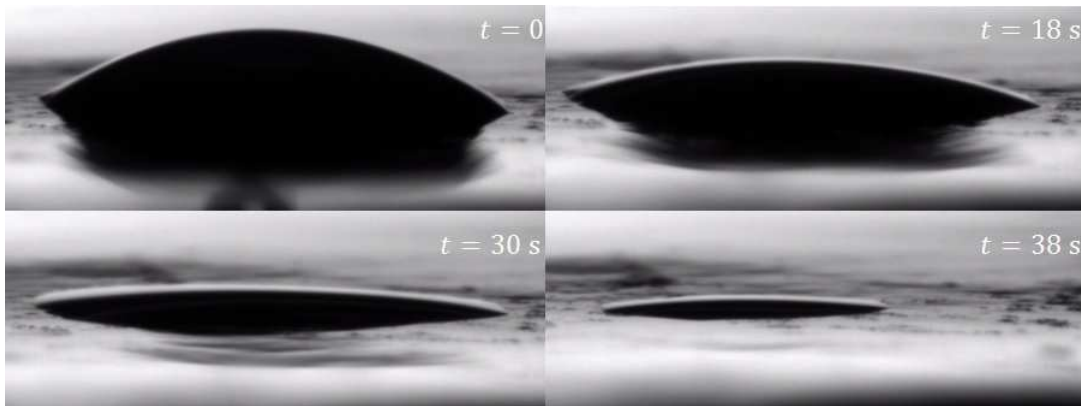
Figure 3.9: Different stages of droplet spreading and imbibition on PES_L2 membrane.
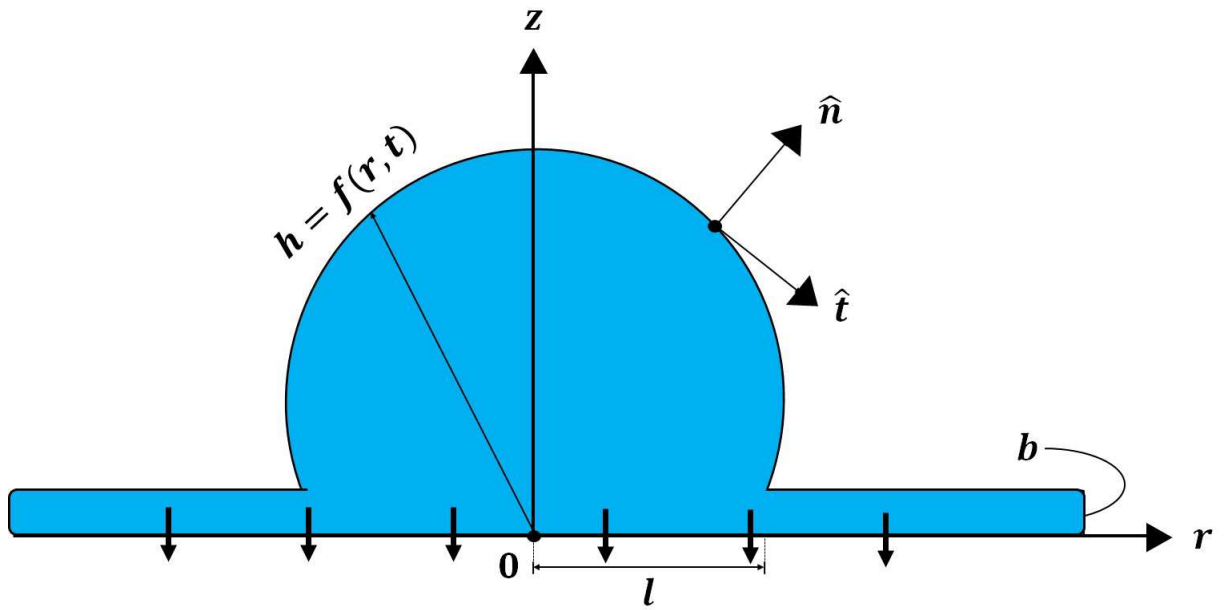
Figure 3.10: An axi-symmetric droplet on a permeable substrate.
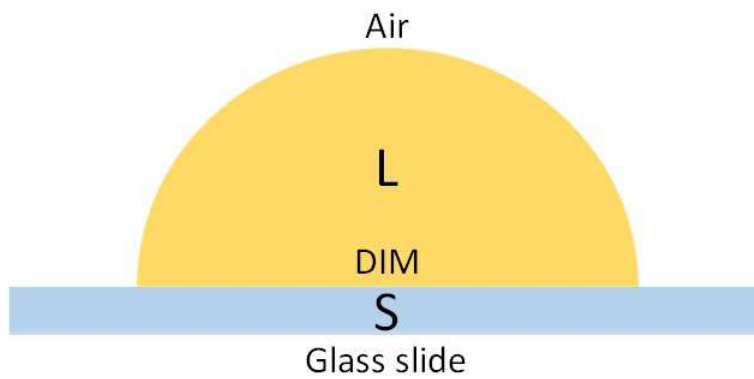
Figure 3.11: Diiodomethane (DIM) spreading on laboratory glass slide.
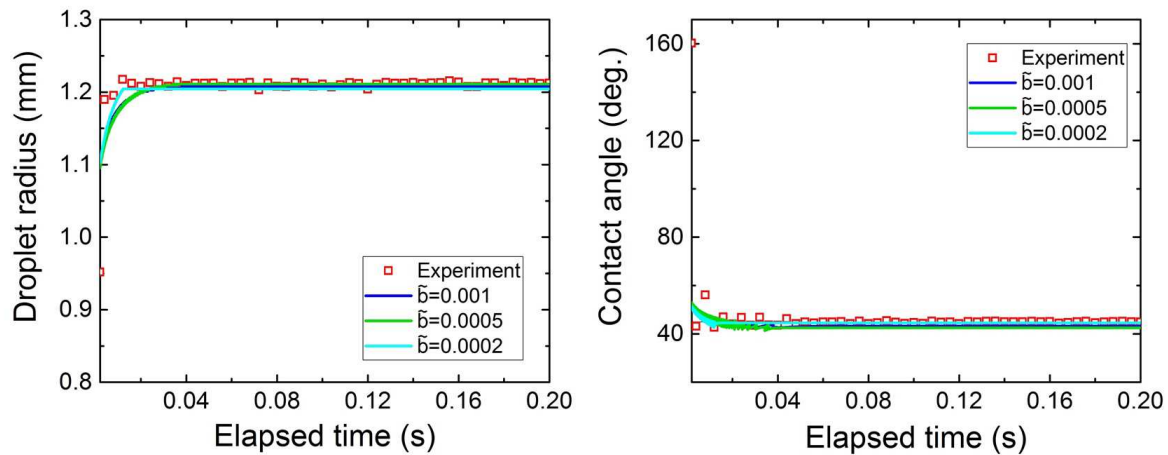
Figure 3.12: Dynamic radius and contact angle of DIM spreading on glass slide. The simulation parameters are: V=1.0 μL, l=1.2 mm, B=0.919, ϵ=0.353, and b=424, 212, 84.8 nm.
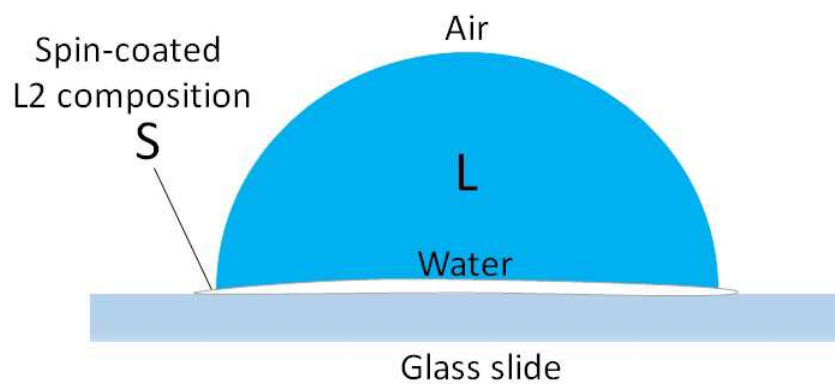
Figure 3.13: Water droplet spreading on spin-coated L2 composition.
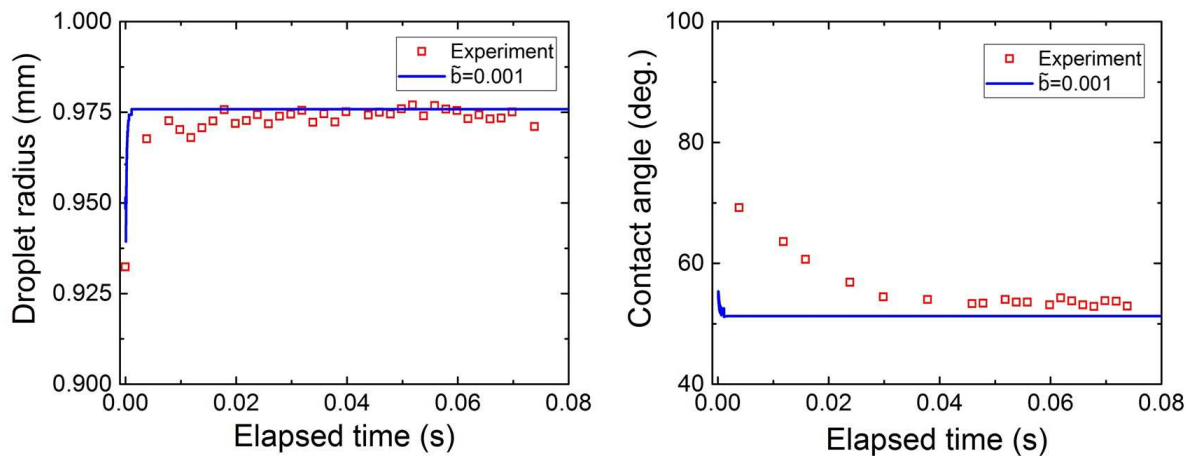
Figure 3.14: Dynamic radius and contact angle of water droplet spreading on L2 coating. The simulation parameters are: V=1.0 μL, l=0.98 mm, B=0.131, ϵ=0.603, and b=591 nm.
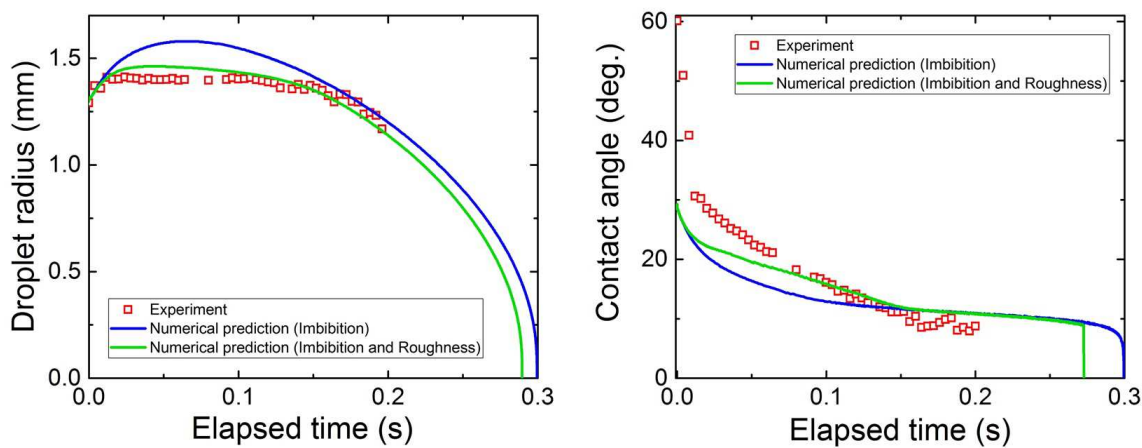
Figure 3.15: Dynamic radius and contact angle of water droplet spreading and imbibition on membrane PES_C1. The simulation parameters are: V=0.213 μL, l=1.4 mm, B=0.267, ϵ=0.049, b276 nm, and κ=10^{-11} m^2.

71
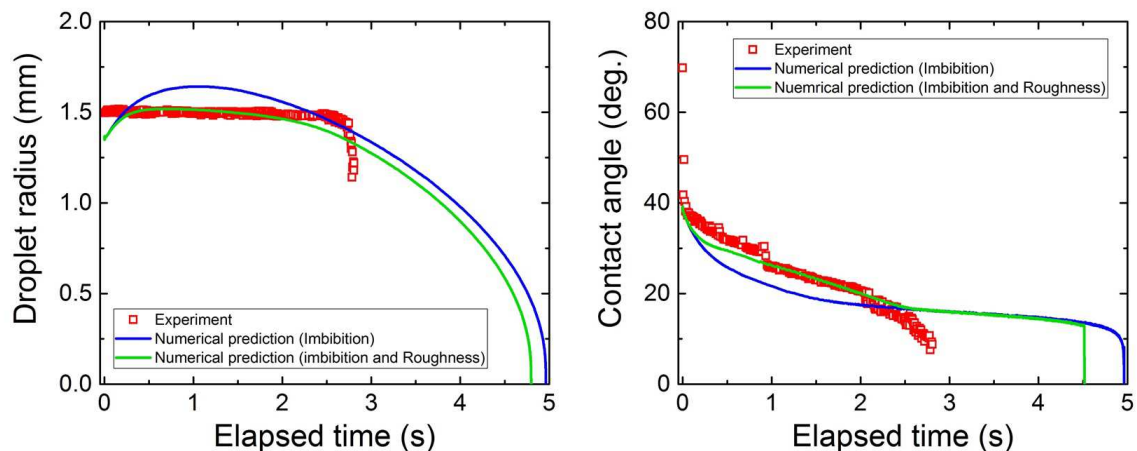
Figure 3.16: Dynamic radius and contact angle of water droplet spreading and imbibition on membrane PES_C2. The simulation parameters are: V=0.079 μL, l=1.35 mm, B=0.248, ϵ=0.021, b=111 nm, and κ=5.489x10^{-13} m^2.
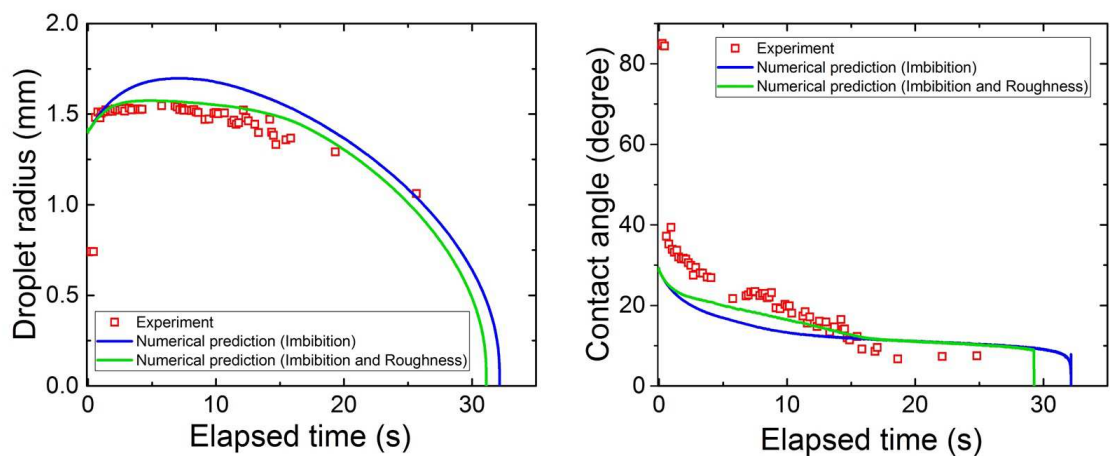
Figure 3.17: Dynamic radius and contact angle of water droplet spreading and imbibition on membrane PES_L1. The simulation parameters are: V=0.053 μL, l=1.5 mm, B=0.307, ϵ=0.01, b=60 nm, and κ=1.628x10^{-13} m^2.
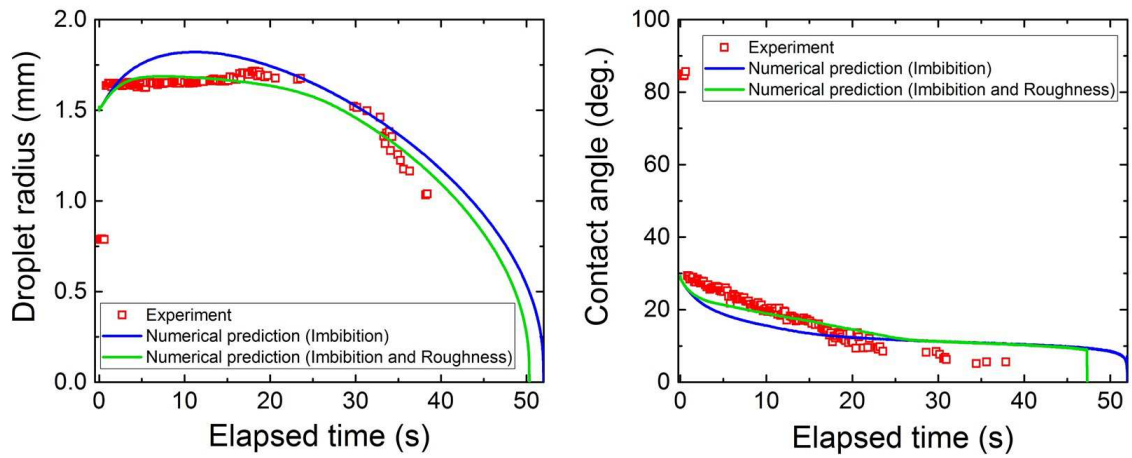
Figure 3.18: Dynamic radius and contact angle of water droplet spreading and imbibition on membrane PES_L2. The simulation parameters are: V=0.05 μL, l=1.5 mm, B=0.307, ϵ=0.00933, b=56 nm, and κ=9.832x10^{-14} m^2.

Chapter 4

Conclusions and Future Work

4.1 Conclusions

The thesis is based on the premise of understanding a fundamental phenomena in depth and trying to explain the nature with respect to an application. The phenomena under investigation are the spreading and imbibition of a thin droplet on rough, permeable substrates. The application in focus are the rough, permeable microfiltration membranes fabricated using phase inversion process as well as the commercial membranes. The precursor film based mathematical model makes prediction of droplet radius and contact angle as a function of time. Both these physical quantities are obtained directly from contact angle measurements. The pinning dynamics is captured by surface profile parameters which are not obtained from any experiment or characterization test. This is because the surface roughness values reported by AFM data is too small to initiate pinning for millimetric droplets. The actual cause of pinning is a combination of physico-chemical interactions. In the case of permeation, hydrodynamic resistance is obtained independently from filtration test. The effective permeability is a derived quantity since it depends on the radius and height of droplet at any given stage as well as the cross-section thickness of the substrate (obtained from SEM). The hydrodynamic permeability defined is also a derived quantity because of its dependence on cross-section thickness of the substrate and hydrodynamic resistance which is obtained directly from filtration tests. The goal is to link the intrinsic properties of the membranes to the phenomena of droplet spreading and imbibition.

The first part of the thesis deals with the importance of different characteristic parameters in the numerical prediction of experimental data. Droplet spread-

ing and imbibition on the impermeable and permeable substrate is studied using a mathematical model based on lubrication approximation. The time evolution equation of droplet height is derived using Stokes' equations. The kinematic boundary condition along with a normal and tangential component of interfacial stress balance are used. The contact line singularity is relieved using precursor film assumption and disjoining pressure. The equilibrium stage is controlled by the disjoining pressure term. The no-slip condition is used to close the system of equations. The imbibition condition is given by Darcy's law which removes the need for thickness dependent permeability. The resulting nonlinear partial differential equation (PDE) is solved numerically using finite difference scheme of second order accuracy. Since the spreading and imbibition phenomena of a droplet is largely dependent on the initial and equilibrium stages, it was important to figure out how the choice of characteristic parameters i.e. radius and height of droplet based on these two stages affected the numerical prediction. Using experimental data available in literature, two sets of normalizing factors based on initial and equilibrium stages were studied. The investigation revealed that either set of normalizing factors lead to the same prediction of droplet radius and contact angle when compared to experiments, provided the dimensional values of precursor film thickness, disjoining pressure and imbibition coefficient are kept constant. However, a significant gap was observed in the prediction of the equilibrium contact angle using the two normalizing factors. To bridge this gap, a modified scaling relation is proposed which enables the prediction of the equilibrium stage with 5% error. This scaling relation is comparatively more appropriate for the equilibrium set of normalizing factors since there is ambiguity in the definition of the initial stage. Thus, an explanation is provided on why equilibrium set of normalizing factors should always be used when making a comparison with experimental data.

The second part of the thesis focuses on experimental and numerical studies of droplet spreading and imbibition on lab-fabricated and commercial PES membranes. The membranes are characterized in terms of permeability by filtration test, cross-section thickness using SEM images, surface roughness using AFM, and hydrophilicity using dynamic contact angle measurement. For both apolar (DIM on a glass slide) and polar interactions (Water on spin-coated PES membrane), the estimation of disjoining pressure is verified using

theory and the lubrication based mathematical model. The hydrodynamic permeability of the membranes is calculated on the basis of its thickness and hydrodynamic resistance, which is the slope of the filtration curve. The effective permeability is calculated by the droplet spreading and imbibition on the surface of the membranes. The developed model based on lubrication approximation in the previous part is employed to calculate effective permeability. The set of normalizing factors based on equilibrium stage is utilized to make a comparison with droplet radius and contact angle measurements. The effective and hydrodynamic permeabilities are shown to match reasonably when the former relation is tweaked by the introduction of lubrication ratio at the equilibrium stage. The mathematical model successfully captures the pinning behaviour across a range of imbibition time scale with the introduction of a single Gaussian defect.

4.2 Future Work

Some of the future studies which can be undertaken as continuation of this work are as follows:

- The contact line pinning observed in the experiments is attributed to micrometric defects on the surface of membranes. However, it is not quite clear how these defects influence the movement of the contact line. In order to understand the physics of contact line movement due to surface topography, it is essential to do experiments targetted at capturing the pinning effect. The question worth asking is: How different topographical features affect the spreading and imbibition of millimetric droplets? For this purpose, different fabrication techniques like micro and nano-patterning can be exploited to cast features with size ranging from nanometers to few micrometers. To begin with, the features can be patterned on solid PDMS substrate. The contact angle measurements can be performed on PDMS substrate, with droplet volumes ranging $0.2-2$ μL. Some optical techniques can also be used to precisely track the movement of the contact line. This will provide more insight on the role of different features on the contact line pinning. To extend the analysis to permeable substrates, similar fabrication techniques can be used on membranes with varying degree of porosity and hydrophilicity. It is also worth mentioning here that the correlation between hydrophilicity

and porosity is not well understood. Hence, it is important to distinguish between the two before setting out to understand the pinning behaviour on permeable substrates. In order to minimize the role of evaporation, it is necessary to perform the contact angle measurements on membranes with very high permeability. The staircase behaviour observed in our previous investigation was primarily due to slow imbibition. The imbibition was slow but not slow enough for evaporation to be dominant. This will throw light on the influence of porosity on the contact line dynamics. However, it is essential to keep hydrophilicity same for the substrates. To accomplish this, some degree of bulk modification of the membranes will be needed which will only affect its porosity. In order to comprehend the role of hydrophilicity on contact line dynamics, it would be necessary to modify the surface properties of the membrane, keeping the porosity unchanged. This in-depth study comprising of solid and permeable substrates with different nature of surface and bulk modifications will revolutionize the outlook on topography-controlled free surface flows.

- The equilibrium stage dependent characteristic parameters are appropriate for numerical predictions with experimental data. The investigation was carried out for the impermeable and permeable substrates, in the absence of contact line pinning. In the presence of defects, the contact line is pinned and the apparent contact angle increases. It would be worthwhile to investigate how the equilibrium contact angle is influenced by the addition of topographical features for both impermeable and permeable substrates. The equilibrium stage is controlled by the disjoining pressure term which is a combination of repulsive and attractive intermolecular forces. A modification of the theoretical disjoining pressure parameter, based on the lubrication ratio was proposed in our investigation. This modification might depend on the nature of topography. As a result, the disjoining pressure parameter will depend on two length scales: one of the droplet and another of the surface topography, thus making it more a realistic prediction of the equilibrium stage. The modification of the disjoining pressure in the form of two different length scales can be derived from first principles. This would lead to corrected Young-Laplace equation, as a function of droplet and topography length scales.

- The imbibition condition incorporated in the mathematical model is based on the simplified Darcy's model. This does not take into account the role of capillary forces in the movement of the imbibition front. It also neglects the pore distribution which varies from one membrane to another. The properties of the permeable substrate is lumped into the imbibition coefficient. To understand the effect of porosity on imbibition dynamics, it is necessary to perform pore network simulations. This can be accomplished by modelling the porous medium as a separate entity but coupled to the equations governing the flow on the top surface of the membrane. Capillary forces can be taken into account which will provide better interpretation of the permeability of the substrate.

- The contact line pinning in our investigations has been attributed to surface topography. However, pinning effect can be captured by physico-chemical processes like evaporation and thermo-capillary stresses. This can be achieved by introducing a new governing equation in the form of energy conservation and boundary condition in the form of energy balance. For evaporation, the surface tension acting at the liquid-vapor interface is considered to be constant. On the other hand, the effect of thermo-capillarity is studied by considering surface tension as a function of temperature. Each of these processes can be studied in conjunction with substrate topography to understand the relative importance of these process to substrate topography in dictating pinning behaviour.

4.3 List of contributions

The following is a list of contributions from this thesis in the form of preprints and conference presentations.

4.3.1 Preprints

Ref. [139] -Debanik Bhattacharjee, Hadi Nazaripoor, and Mohtada Sadrzadeh. Droplet spreading: Role of characteristic length scales and modified disjoining pressure. arXiv preprint arXiv:1707.09392, 2017.

4.3.2 Conference presentations

-Debanik Bhattacharjee, Babak Soltannia, Hadi Nazaripoor, Mohtada Sadrzadeh. Effect of surface roughness on membrane wettability. Complex Motion in Fluids Summer School, DAMTP, University of Cambridge, 2017.

Ref. [146] -Debanik Bhattacharjee, Hadi Nazaripoor, and Mohtada Sadrzadeh. The role of characteristic parameters in the numerical prediction of droplet radius and contact angle. Bulletin of the American Physical Society, 2017.

Ref. [147] -Debanik Bhattacharjee, Babak Soltannia, Hadi Nazaripoor, and Mohtada Sadrzadeh. Effect of surface roughness on contact line dynamics of a thin droplet. Bulletin of the American Physical Society, 2017.

References

[1] Michel J De Ruijter, Joël De Coninck, TD Blake, A Clarke, and A Rankin. Contact angle relaxation during the spreading of partially wetting drops. *Langmuir*, 13(26):7293–7298, 1997.

[2] Zaifei Wang, Leonardo Espín, Frank S Bates, Satish Kumar, and Christopher W Macosko. Water droplet spreading and imbibition on superhydrophilic poly (butylene terephthalate) melt-blown fiber mats. *Chem. Eng. Sci.*, 146:104–114, 2016.

[3] Sathish M Kumar and Abhijit P Deshpande. Dynamics of drop spreading on fibrous porous media. *Colloids Surf., A*, 277(1):157–163, 2006.

[4] LH Tanner. The spreading of silicone oil drops on horizontal surfaces. *J. Phys. D: Appl. Phys.*, 12(9):1473, 1979.

[5] Allan Rosenberg, Roberta Williams, and George Cohen. Interaction forces involved in wetting of human skin. *Journal of pharmaceutical sciences*, 62(6):920–922, 1973.

[6] Alexander T Barrows, Andrew J Pearson, Chan Kyu Kwak, Alan DF Dunbar, Alastair R Buckley, and David G Lidzey. Efficient planar heterojunction mixed-halide perovskite solar cells deposited via spray-deposition. *Energy & Environmental Science*, 7(9):2944–2950, 2014.

[7] Dan Soltman, Ben Smith, Hongki Kang, SJS Morris, and Vivek Subramanian. Methodology for inkjet printing of partially wetting films. *Langmuir*, 26(19):15686–15693, 2010.

[8] Liangliang Cao, Andrew K Jones, Vinod K Sikka, Jianzhong Wu, and Di Gao. Anti-icing superhydrophobic coatings. *Langmuir*, 25(21):12444–12448, 2009.

[9] Norman R Morrow et al. Wettability and its effect on oil recovery. *Journal of Petroleum Technology*, 42(12):1–476, 1990.

[10] Thomas Young. An essay on the cohesion of fluids. *Philosophical Transactions of the Royal Society of London*, 95:65–87, 1805.

[11] Malcolm E Schrader. Young-dupre revisited. *Langmuir*, 11(9):3585–3589, 1995.

[12] Pierre-Gilles De Gennes. Wetting: statics and dynamics. *Reviews of modern physics*, 57(3):827, 1985.

[13] H Hervet and P-G De Gennes. Dynamique du mouillage: films précurseurs sur solides. *Comptes-rendus des séances de l'Académie des sciences. Série 2, Mécanique-physique, chimie, sciences de l'univers, sciences de la terre*, 299(9):499–503, 1984.

[14] P Levinson, AM Cazabat, MA Cohen Stuart, F Heslot, and S Nicolet. The spreading of macroscopic droplets. *Revue de Physique Appliquee*, 23(6):1009–1016, 1988.

[15] Benzhong Zhao, Christopher W MacMinn, and Ruben Juanes. Wettability control on multiphase flow in patterned microfluidics. *Proceedings of the National Academy of Sciences*, 113(37):10251–10256, 2016.

[16] VM Starov, SA Zhdanov, SR Kosvintsev, VD Sobolev, and MG Velarde. Spreading of liquid drops over porous substrates. *Advances in Colloid and Interface Science*, 104(1):123–158, 2003.

[17] ABD Cassie and S Baxter. Wettability of porous surfaces. *Transactions of the Faraday society*, 40:546–551, 1944.

[18] Daniel Bonn, Jens Eggers, Joseph Indekeu, Jacques Meunier, and Etienne Rolley. Wetting and spreading. *Reviews of modern physics*, 81(2):739, 2009.

[19] Robert N Wenzel. Resistance of solid surfaces to wetting by water. *Industrial & Engineering Chemistry*, 28(8):988–994, 1936.

[20] AM Cazabat and MA Cohen Stuart. Dynamics of wetting: effects of surface roughness. *The Journal of Physical Chemistry*, 90(22):5845–5849, 1986.

[21] Meirav Apel-Paz and Abraham Marmur. Spreading of liquids on rough surfaces. *Colloids and Surfaces A: Physicochemical and Engineering Aspects*, 146(1):273–279, 1999.

[22] J Bico, C Tordeux, and D Quéré. Rough wetting. *EPL (Europhysics Letters)*, 55(2):214, 2001.

[23] Deniz Ertaş and Mehran Kardar. Critical dynamics of contact line depinning. *Physical Review E*, 49(4):R2532, 1994.

[24] Elie Raphael and Pierre-Gilles de Gennes. Dynamics of wetting with nonideal surfaces. the single defect problem. *The Journal of Chemical Physics*, 90(12):7577–7584, 1989.

[25] S Moulinet, C Guthmann, and E Rolley. Roughness and dynamics of a contact line of a viscous fluid on a disordered substrate. *The European Physical Journal E: Soft Matter and Biological Physics*, 8(4):437–443, 2002.

[26] Alexis Prevost, Etienne Rolley, and Claude Guthmann. Dynamics of a helium-4 meniscus on a strongly disordered cesium substrate. *Physical Review B*, 65(6):064517, 2002.

[27] EL Decker and S Garoff. Contact line structure and dynamics on surfaces with contact angle hysteresis. *Langmuir*, 13(23):6321–6332, 1997.

[28] JF Joanny and Pierre-Gilles De Gennes. A model for contact angle hysteresis. In *Simple Views on Condensed Matter*, pages 457–467. World Scientific, 2003.

[29] C Huh and SG Mason. Effects of surface roughness on wetting (theoretical). *Journal of colloid and interface science*, 60(1):11–38, 1977.

[30] TD Blake and JM Haynes. Kinetics of liquidliquid displacement. *Journal of colloid and interface science*, 30(3):421–423, 1969.

[31] Mathieu Delmas, Marc Monthioux, and Thierry Ondarçuhu. Contact angle hysteresis at the nanometer scale. *Physical review letters*, 106(13):136102, 2011.

[32] Melanie Ramiasa, John Ralston, Renate Fetzer, and Rossen Sedev. The influence of topography on dynamic wetting. *Advances in colloid and interface science*, 206:275–293, 2014.

[33] Chun Huh and LE Scriven. Hydrodynamic model of steady movement of a solid/liquid/fluid contact line. *Journal of Colloid and Interface Science*, 35(1):85–101, 1971.

[34] Peter A Thompson and Sandra M Troian. A general boundary condition for liquid flow at solid surfaces. *Nature*, 389(6649):360–362, 1997.

[35] Yulii D Shikhmurzaev. Moving contact lines in liquid/liquid/solid systems. *Journal of Fluid Mechanics*, 334:211–249, 1997.

[36] LM Hocking. A moving fluid interface on a rough surface. *Journal of Fluid Mechanics*, 76(4):801–817, 1976.

[37] Peter C Wayner Jr. Spreading of a liquid film with a finite contact angle by the evaporation/condensation process. *Langmuir*, 9(1):294–299, 1993.

[38] VA Gorodtsov. Spreading of a film of nonlinearly viscous liquid over a horizontal smooth solid surface. *Journal of Engineering Physics and Thermophysics*, 57(2):879–884, 1989.

[39] Pierre Seppecher. Moving contact lines in the cahn-hilliard theory. *International journal of engineering science*, 34(9):977–992, 1996.

[40] MH Eres, LW Schwartz, and RV Roy. Fingering phenomena for driven coating films. *Physics of Fluids*, 12(6):1278–1295, 2000.

[41] Arezki Boudaoud. Non-newtonian thin films with normal stresses: dynamics and spreading. *The European Physical Journal E: Soft Matter and Biological Physics*, 22(2):107–109, 2007.

[42] Mihail Nicolae Popescu, G Oshanin, S Dietrich, and AM Cazabat. Precursor films in wetting phenomena. *J. Phys.: Condens. Matter*, 24(24):243102, 2012.

[43] W Bate Hardy. Iii. the spreading of fluids on glass. *The London, Edinburgh, and Dublin Philosophical Magazine and Journal of Science*, 38(223):49–55, 1919.

[44] D. H. Bangham and Z. Saweris. The behaviour of liquid drops and adsorbed films at cleavage surfaces of mica. *Trans. Faraday Soc.*, 34:554–570, 1938.

[45] Willard D Bascom, Robert L Cottington, and Curtis R Singleterry. Dynamic surface phenomena in the spontaneous spreading of oils on solids. ACS Publications, 1964.

[46] W Radigan, H Ghiradella, HL Frisch, H Schonhorn, and TK Kwei. Kinetics of spreading of glass on fernico metal. *J. Colloid Interface Sci.*, 49(2):241–248, 1974.

[47] BV Derjaguin and NV Churaev. Structural component of disjoining pressure. *Journal of Colloid and Interface Science*, 49(2):249–255, 1974.

[48] JF Joanny and P-G De Gennes. Upward creep of a wetting fluid: a scaling analysis. *Journal de Physique*, 47(1):121–127, 1986.

[49] Anne-Marie Cazabat. How does a droplet spread? *Contemporary Physics*, 28(4):347–364, 1987.

[50] D Ausserré, AM Picard, and L Léger. Existence and role of the precursor film in the spreading of polymer liquids. *Physical review letters*, 57(21):2671, 1986.

[51] L Leger, M Erman, AM Guinet-Picard, D Ausserre, and C Strazielle. Precursor film profiles of spreading liquid drops. *Physical review letters*, 60(23):2390, 1988.

[52] H Pirouz Kavehpour, Ben Ovryn, and Gareth H McKinley. Microscopic and macroscopic structure of the precursor layer in spreading viscous drops. *Physical review letters*, 91(19):196104, 2003.

[53] Michel J De Ruijter, Joël De Coninck, and G Oshanin. Droplet spreading: partial wetting regime revisited. *Langmuir*, 15(6):2209–2216, 1999.

[54] Jens Eggers and Howard A Stone. Characteristic lengths at moving contact lines for a perfectly wetting fluid: the influence of speed on the dynamic contact angle. *Journal of Fluid Mechanics*, 505:309–321, 2004.

[55] N Savva and S Kalliadasis. Dynamics of moving contact lines: A comparison between slip and precursor film models. *EPL (Europhysics Letters)*, 94(6):64004, 2011.

[56] KB Glasner. Spreading of droplets under the influence of intermolecular forces. *Phys Fluids*, 15(7):1837–1842, 2003.

[57] SH Davis and LM Hocking. Spreading and imbibition of viscous liquid on a porous base. *Physics of fluids*, 11(1):48–57, 1999.

[58] SH Davis and LM Hocking. Spreading and imbibition of viscous liquid on a porous base. ii. *Physics of fluids*, 12(7):1646–1655, 2000.

[59] N Alleborn and H Raszillier. Spreading and sorption of a droplet on a porous substrate. *Chem. Eng. Sci.*, 59(10):2071–2088, 2004.

[60] Vladimir S Ajaev. Spreading of thin volatile liquid droplets on uniformly heated surfaces. *Journal of Fluid Mechanics*, 528:279–296, 2005.

[61] A Zadražil, F Stepanek, and OK Matar. Droplet spreading, imbibition and solidification on porous media. *J. Fluid Mech.*, 562:1–33, 2006.

[62] Juan M Gomba and George M Homsy. Regimes of thermocapillary migration of droplets under partial wetting conditions. *J. Fluid Mech.*, 647:125–142, 2010.

[63] Leonardo Espín and Satish Kumar. Droplet spreading and absorption on rough, permeable substrates. *Journal of Fluid Mechanics*, 784:465–486, 2015.

[64] Kihwan Choi, Alphonsus H.C. Ng, Ryan Fobel, and Aaron R. Wheeler. Digital microfluidics. *Annu. Rev. Anal. Chem.*, 5(1):413–440, 2012.

[65] Minxuan Kuang, Libin Wang, and Yanlin Song. Controllable printing droplets for high-resolution patterns. *Adv. Mater.*, 26(40):6950–6958, 2014.

[66] Noha A. Mousa, Mais J. Jebrail, Hao Yang, Mohamed Abdelgawad, Pavel Metalnikov, Jian Chen, Aaron R. Wheeler, and Robert F. Casper. Droplet-scale estrogen assays in breast tissue, blood, and serum. *Sci. Transl. Med.*, 1(1):1ra2–1ra2, 2009.

[67] W. Jia and H.-H. Qiu. Experimental investigation of droplet dynamics and heat transfer in spray cooling. *Exp. Therm Fluid Sci.*, 27(7):829 – 838, 2003.

[68] Steven W. Benintendi and Marc K. Smith. The spreading of a non-isothermal liquid droplet. *Phys. Fluids*, 11(5):982–989, 1999.

[69] N.M. Kovalchuk, A. Trybala, and V.M. Starov. Evaporation of sessile droplets. *Curr. Opin. Colloid Interface Sci.*, 19(4):336 – 342, 2014.

[70] H. Yildirim Erbil and R. Alsan Meric. Evaporation of sessile drops on polymer surfaces: ellipsoidal cap geometry. *J. Phys. Chem. B*, 101(35):6867–6873, 1997.

[71] Glen McHale, Michael I Newton, and Neil J Shirtcliffe. Dynamic wetting and spreading and the role of topography. *J. Phys.: Condens. Matter*, 21(46):464122, 2009.

[72] Laurent Courbin, Etienne Denieul, Emilie Dressaire, Marcus Roper, Armand Ajdari, and Howard A Stone. Imbibition by polygonal spreading on microdecorated surfaces. *Nat Mater*, 6(9):661–664, 2007.

[73] N. Savva and S. Kalliadasis. Influence of gravity on the spreading of two-dimensional droplets over topographical substrates. *J. Eng. Math.*, 73(1):3–16, 2012.

[74] Hedieh Modaressi and Gil Garnier. Mechanism of wetting and absorption of water droplets on sized paper: effects of chemical and physical heterogeneity. *Langmuir*, 18(3):642–649, 2002.

[75] O Bliznyuk, E Vereshchagina, E Stefan Kooij, and Bene Poelsema. Scaling of anisotropic droplet shapes on chemically stripe-patterned surfaces. *Phys Rev E*, 79(4):041601, 2009.

[76] Stephan Herminghaus, Martin Brinkmann, and Ralf Seemann. Wetting and dewetting of complex surface geometries. *Annu. Rev. Mater. Res.*, 38(1):101–121, 2008.

[77] X Frank and Patrick Perre. Droplet spreading on a porous surface: A lattice boltzmann study. *Phys. Fluids*, 24(4):042101, 2012.

[78] James M Acton, Herbert E Huppert, and M Grae Worster. Two-dimensional viscous gravity currents flowing over a deep porous medium. *J. Fluid Mech.*, 440:359–380, 2001.

[79] Victor M. Starov. Surfactant solutions and porous substrates: spreading and imbibition. *Adv. Colloid Interface Sci.*, 111(12):3 – 27, 2004.

[80] Gang He and NG Hadjiconstantinou. A molecular view of tanner's law: molecular dynamics simulations of droplet spreading. *J. Fluid Mech.*, 497:123–132, 2003.

[81] Michel J De Ruijter, TD Blake, and Joël De Coninck. Dynamic wetting studied by molecular modeling simulations of droplet spreading. *Langmuir*, 15(22):7836–7847, 1999.

[82] FH Song, BQ Li, and C Liu. Molecular dynamics simulation of nanosized water droplet spreading in an electric field. *Langmuir*, 29(13):4266–4274, 2013.

[83] Nahid Sedighi, Sohail Murad, and Suresh K Aggarwal. Molecular dynamics simulations of nanodroplet spreading on solid surfaces, effect of droplet size. *Fluid Dynamics Research*, 42(3):035501, 2010.

[84] Nahid Sedighi, Sohail Murad, and Suresh K Aggarwal. Molecular dynamics simulations of spontaneous spreading of a nanodroplet on solid surfaces. *Fluid Dynamics Research*, 43(1):015507, 2010.

[85] P Raiskinmäki, A Koponen, J Merikoski, and J Timonen. Spreading dynamics of three-dimensional droplets by the lattice-boltzmann method. *Comput. Mater. Sci.*, 18(1):7–12, 2000.

[86] Elham Attar and Carolin Körner. Lattice boltzmann method for dynamic wetting problems. *J Colloid Interface Sci*, 335(1):84–93, 2009.

[87] A Dupuis and Julia M Yeomans. Lattice boltzmann modelling of droplets on chemically heterogeneous surfaces. *Future Generation Computer Systems*, 20(6):993–1001, 2004.

[88] Alejandro M Briones, Jamie S Ervin, Shawn A Putnam, Larry W Byrd, and Lois Gschwender. Micrometer-sized water droplet impingement dynamics and evaporation on a flat dry surface. *Langmuir*, 26(16):13272–13286, 2010.

[89] Peter Ehrhard and Stephen H Davis. Non-isothermal spreading of liquid drops on horizontal plates. *J. Fluid Mech.*, 229:365–388, 1991.

[90] Harvey P Greenspan. On the motion of a small viscous droplet that wets a surface. *J. Fluid Mech.*, 84(01):125–143, 1978.

[91] RG Cox. The dynamics of the spreading of liquids on a solid surface. part 1. viscous flow. *J. Fluid Mech.*, 168:169–194, 1986.

[92] Patrick J Haley and Michael J Miksis. The effect of the contact line on droplet spreading. *J Fluid Mech*, 223:57–81, 1991.

[93] JB Bostwick. Spreading and bistability of droplets on differentially heated substrates. *J. Fluid Mech.*, 725:566–587, 2013.

[94] Marc K Smith. Thermocapillary migration of a two-dimensional liquid droplet on a solid surface. *J. Fluid Mech.*, 294:209–230, 1995.

[95] A Hoang and HP Kavehpour. Dynamics of nanoscale precursor film near a moving contact line of spreading drops. *Physical review letters*, 106(25):254501, 2011.

[96] Helen Ghiradella, William Radigan, and HL Frisch. Electrical resistivity changes in spreading liquid films. *J. Colloid Interface Sci.*, 51(3):522–526, 1975.

[97] Leonard W Schwartz. Hysteretic effects in droplet motions on heterogeneous substrates: direct numerical simulation. *Langmuir*, 14(12):3440–3453, 1998.

[98] SH Davis and LM Hocking. Spreading and imbibition of viscous liquid on a porous base. *Physics of fluids*, 11(1):48–57, 1999.

[99] LW Schwartz, D Roux, and JJ Cooper-White. On the shapes of droplets that are sliding on a vertical wall. *Physica D*, 209(1):236–244, 2005.

[100] Leonard W Schwartz and Richard R Eley. Simulation of droplet motion on low-energy and heterogeneous surfaces. *Journal of Colloid and Interface Science*, 202(1):173–188, 1998.

[101] Aurélie Lafuma and David Quéré. Superhydrophobic states. *Nat Mater*, 2(7):457–460, 2003.

[102] Hua Hu and Ronald G Larson. Analysis of the microfluid flow in an evaporating sessile droplet. *Langmuir*, 21(9):3963–3971, 2005.

[103] Guillaume Berteloot, C-T Pham, A Daerr, François Lequeux, and Laurent Limat. Evaporation-induced flow near a contact line: Consequences on coating and contact angle. *EPL (Europhysics Letters)*, 83(1):14003, 2008.

[104] Feng-Chao Wang and Heng-An Wu. Pinning and depinning mechanism of the contact line during evaporation of nano-droplets sessile on textured surfaces. *Soft Matter*, 9(24):5703–5709, 2013.

[105] Hua Hu and Ronald G. Larson. Evaporation of a sessile droplet on a substrate. *The Journal of Physical Chemistry B*, 106(6):1334–1344, 2002.

[106] Robert D Deegan, Olgica Bakajin, Todd F Dupont, Greg Huber, et al. Capillary flow as the cause of ring stains from dried liquid drops. *Nature*, 389(6653):827, 1997.

[107] Robert D Deegan. Pattern formation in drying drops. *Physical review E*, 61(1):475, 2000.

[108] GD Nadkarni and S Garoff. Reproducibility of contact line motion on surfaces exhibiting contact angle hysteresis. *Langmuir*, 10(5):1618–1623, 1994.

[109] Bryan B Sauer and Thomas E Carney. Dynamic contact angle measurements on glass fibers: influence of fiber diameter on hysteresis and contact line pinning. *Langmuir*, 6(5):1002–1007, 1990.

[110] Michael F Schatz and G Paul Neitzel. Experiments on thermocapillary instabilities. *Annual Review of Fluid Mechanics*, 33(1):93–127, 2001.

[111] Tanja Cuk, Sandra M Troian, Cheong Min Hong, and Sigurd Wagner. Using convective flow splitting for the direct printing of fine copper lines. *MRS Online Proceedings Library Archive*, 624, 2000.

[112] TS Chow. Wetting of rough surfaces. *J. Phys.: Condens. Matter*, 10(27):L445, 1998.

[113] Nikos Savva, Serafim Kalliadasis, and Grigorios A Pavliotis. Two-dimensional droplet spreading over random topographical substrates. *Phys Rev Lett*, 104(8):084501, 2010.

[114] Stephan Herminghaus. Wetting, spreading, and adsorption on randomly rough surfaces. *Eur. Phys. J. E*, 35(6):1–10, 2012.

[115] Tzu Chieh Chao, Omid Arjmandi-Tash, Diganta B Das, and Victor M Starov. Spreading of blood drops over dry porous substrate: Complete wetting case. *Journal of colloid and interface science*, 446:218–225, 2015.

[116] Niklas Sandler, Anni Määttänen, Petri Ihalainen, Leif Kronberg, Axel Meierjohann, Tapani Viitala, and Jouko Peltonen. Inkjet printing of drug substances and use of porous substrates-towards individualized dosing. *Journal of pharmaceutical sciences*, 100(8):3386–3395, 2011.

[117] R Wang, HY Zhang, PHM Feron, and DT Liang. Influence of membrane wetting on co 2 capture in microporous hollow fiber membrane contactors. *Separation and Purification Technology*, 46(1):33–40, 2005.

[118] Madeleine J Golding, Herbert E Huppert, and Jerome A Neufeld. The effects of capillary forces on the axisymmetric propagation of two-phase, constant-flux gravity currents in porous media. *Physics of Fluids*, 25(3):036602, 2013.

[119] EM Schlueter, RW Zimmerman, PA Witherspoon, and NGW Cook. The fractal dimension of pores in sedimentary rocks and its influence on permeability. *Engineering Geology*, 48(3-4):199–215, 1997.

[120] Longfei Li, RJ Braun, KL Maki, WD Henshaw, and Peter Ewen King-Smith. Tear film dynamics with evaporation, wetting, and time-dependent flux boundary condition on an eye-shaped domain. *Physics of Fluids*, 26(5):052101, 2014.

[121] Pierre-Gilles De Gennes, Françoise Brochard-Wyart, and David Quéré. *Capillarity and wetting phenomena: drops, bubbles, pearls, waves.* Springer Science & Business Media, 2013.

[122] F Heslot, AM Cazabat, P Levinson, and N Fraysse. Experiments on wetting on the scale of nanometers: Influence of the surface energy. *Physical review letters*, 65(5):599, 1990.

[123] Bart Van der Bruggen, Carlo Vandecasteele, Tim Van Gestel, Wim Doyen, and Roger Leysen. A review of pressure-driven membrane processes in wastewater treatment and drinking water production. *Environmental Progress & Sustainable Energy*, 22(1):46–56, 2003.

[124] Efrem Curcio and Enrico Drioli. Membranes for desalination. In *Seawater Desalination*, pages 41–75. Springer, 2009.

[125] David Farr. High pressure technology in the food industry. *Trends in Food Science & Technology*, 1:14–16, 1990.

[126] Yeomin Yoon, Paul Westerhoff, Shane A Snyder, Eric C Wert, and Jaekyung Yoon. Removal of endocrine disrupting compounds and pharmaceuticals by nanofiltration and ultrafiltration membranes. *Desalination*, 202(1):16–23, 2007.

[127] Ming-Liang Luo, Jian-Qing Zhao, Wu Tang, and Chun-Sheng Pu. Hydrophilic modification of poly (ether sulfone) ultrafiltration membrane surface by self-assembly of tio 2 nanoparticles. *Applied Surface Science*, 249(1):76–84, 2005.

[128] Young Wang, Jae-Hong Kim, Kwang-Ho Choo, Yoon-Sik Lee, and Chung-Hak Lee. Hydrophilic modification of polypropylene microfiltration membranes by ozone-induced graft polymerization. *Journal of Membrane Science*, 169(2):269–276, 2000.

[129] A Clarke, TD Blake, K Carruthers, and A Woodward. Spreading and imbibition of liquid droplets on porous surfaces. *Langmuir*, 18(8):2980–2984, 2002.

[130] David N Sibley, Nikos Savva, and Serafim Kalliadasis. Slip or not slip? a methodical examination of the interface formation model using two-dimensional droplet spreading on a horizontal planar substrate as a prototype system. *Physics of Fluids*, 24(8):082105, 2012.

[131] Mohtada Sadrzadeh, Javad Hajinasiri, Subir Bhattacharjee, and David Pernitsky. Nanofiltration of oil sands boiler feed water: Effect of ph on water flux and organic and dissolved solid rejection. *Separation and Purification Technology*, 141:339–353, 2015.

[132] Behnam Khorshidi, Javad Hajinasiri, Guibin Ma, Subir Bhattacharjee, and Mohtada Sadrzadeh. Thermally resistant and electrically conductive pes/ito nanocomposite membrane. *Journal of Membrane Science*, 500:151–160, 2016.

[133] Emily N Tummons, Volodymyr V Tarabara, Jia Wei Chew, and Anthony G Fane. Behavior of oil droplets at the membrane surface during crossflow microfiltration of oil–water emulsions. *Journal of Membrane Science*, 500:211–224, 2016.

[134] JD Winans, KJP Smith, TR Gaborski, JA Roussie, and JL McGrath. Membrane capacity and fouling mechanisms for ultrathin nanomembranes in dead-end filtration. *Journal of Membrane Science*, 499:282–289, 2016.

[135] Søren Lorenzen, Kristian Keiding, and Morten L Christensen. The effect of particle surface charge density on filter cake properties during dead-end filtration. *Chemical Engineering Science*, 163:155–166, 2017.

[136] Wenshan Guo, Huu-Hao Ngo, and Jianxin Li. A mini-review on membrane fouling. *Bioresource technology*, 122:27–34, 2012.

[137] J Mulder. *Basic principles of membrane technology*. Springer Science & Business Media, 2012.

[138] Runnan Zhang, Yanan Liu, Mingrui He, Yanlei Su, Xueting Zhao, Menachem Elimelech, and Zhongyi Jiang. Antifouling membranes for sustainable water purification: strategies and mechanisms. *Chemical Society Reviews*, 45(21):5888–5924, 2016.

[139] Debanik Bhattacharjee, Hadi Nazaripoor, and Mohtada Sadrzadeh. Droplet spreading: Role of characteristic length scales and modified disjoining pressure. *arXiv preprint arXiv:1707.09392*, 2017.

[140] Ashutosh Sharma. Relationship of thin film stability and morphology to macroscopic parameters of wetting in the apolar and polar systems. *Langmuir*, 9(3):861–869, 1993.

[141] Frederick M Fowkes. Attractive forces at interfaces. *Industrial & Engineering Chemistry*, 56(12):40–52, 1964.

[142] CJ Van Oss, RJ Good, and MK Chaudhury. The role of van der waals forces and hydrogen bonds in hydrophobic interactions between biopolymers and low energy surfaces. *Journal of colloid and Interface Science*, 111(2):378–390, 1986.

[143] B Chakrabarty, AK Ghoshal, and MK Purkait. Effect of molecular weight of peg on membrane morphology and transport properties. *Journal of Membrane Science*, 309(1):209–221, 2008.

[144] Babak Soltannia and Dan Sameoto. Strong, reversible underwater adhesion via gecko-inspired hydrophobic fibers. *ACS applied materials & interfaces*, 6(24):21995–22003, 2014.

[145] Behnam Khorshidi, Babak Soltannia, Thomas Thundat, and Mohtada Sadrzadeh. Synthesis of thin film composite polyamide membranes: Effect of monohydric and polyhydric alcohol additives in aqueous solution. *Journal of Membrane Science*, 523:336–345, 2017.

[146] Debanik Bhattacharjee, Hadi Nazaripoor, and Mohtada Sadrzadeh. The role of characteristic parameters in the numerical prediction of droplet radius and contact angle. *Bulletin of the American Physical Society*, 2017.

[147] Debanik Bhattacharjee, Babak Soltannia, Hadi Nazaripoor, and Mohtada Sadrzadeh. Effect of surface roughness on contact line dynamics of a thin droplet. *Bulletin of the American Physical Society*, 2017.

[148] Linda R Petzold. Description of dassl: a differential/algebraic system solver. Technical report, Sandia National Labs., Livermore, CA (USA), 1982.

[149] Roy Leonard Brown and Charles William Gear. Documentation for dfasub: a program for the solution of simultaneous implicit differential and nonlinear equations. Technical report, Illinois Univ., Urbana (USA). Dept. of Computer Science, 1973.

[150] WH Vandevender and KH Haskell. The slatec mathematical subroutine library. *ACM SIGNUM Newsletter*, 17(3):16–21, 1982.

Appendix

A-1 Differential algebraic solver-DASSL

Subroutine DASSL was employed to solved a system of differential algebraic equations which has the form of $F(t, y, y') = 0$. The solver was developed by Linda R. Petzold at Computing and Mathematics Research Division in Lawrence Livermore National Laboratory, CA. USA [148]. This subroutine uses the backward differentiation formula (BDF) to approximate the time derivative and employs the predictor-corrector method [149] with Newton's method to solve the system of equations. At every step, the value for time step and the order of BDF may vary from one to five depending on the nature of solution.

Note: In this work the DASSL is called in a time loop. The subroutine uses adaptive time step to obtain the data for the time period specified by the user.

The DASSL is generally defined as:

$$SUBROUTINE\ DDASSL(RES, NEQ, T, Y, YPRIME, TOUT, INFO,$$
$$RTOL, ATOL, IDID, RWORK, LRW, IWORK, LIW, RPAR, IPAR, JAC)$$

The following information needs to be provided in order to run DASSL:

- RES: This is an external subroutine which contains the DAE system. All the FD discretized equations and the boundary condition are defined in RES.

- NEQ: This specifies the total number of equations which should be solved. In this study it is equal to $NRP \times NYP$

- T: This indicates the current value of the independent variable (time).

- Y: This is the array of size NEQ which contains the current value of the dependent variable (droplet interface height, H). At initial stage, this array is provided by user but at later stages, it becomes a solution from the previous step.

- YPRIME: This is the array of size NEQ which contains the derivatives of the dependent variable (droplet interface height, H). At initial stage, this

array is provided by user but at later stages, it is a solution of DASSL from the previous step.

- TOUT: This is the value at which the user wants to get the solution of Y.

- INFO: This is an integer array which is defined in DASSL so that user can choose regarding the solution of DAE such as initialization, accuracy etc [150].

- RTOL and ATOL: These are the relative and absolute error tolerance, respectively which are necessary for the accuracy of the solution.

- IDID: This is the parameter which DASSL utilizes to identify the warnings and errors caused.

- RWORK and IWORK: These are working arrays and contain information about the solution procedure such as RWORK(7) provides the last successful stepsize used in solver and IWORK(8) provides the order of kth used on the last step [150].

- LIW and LRW: These are inputs directly based on the requirements of the DASSL solver [150].

- RPAR and IPAR: These are real and integer parameter arrays respectively which can be used for communication between the main program and the external subroutine, RES.

B-1 Grid Independence

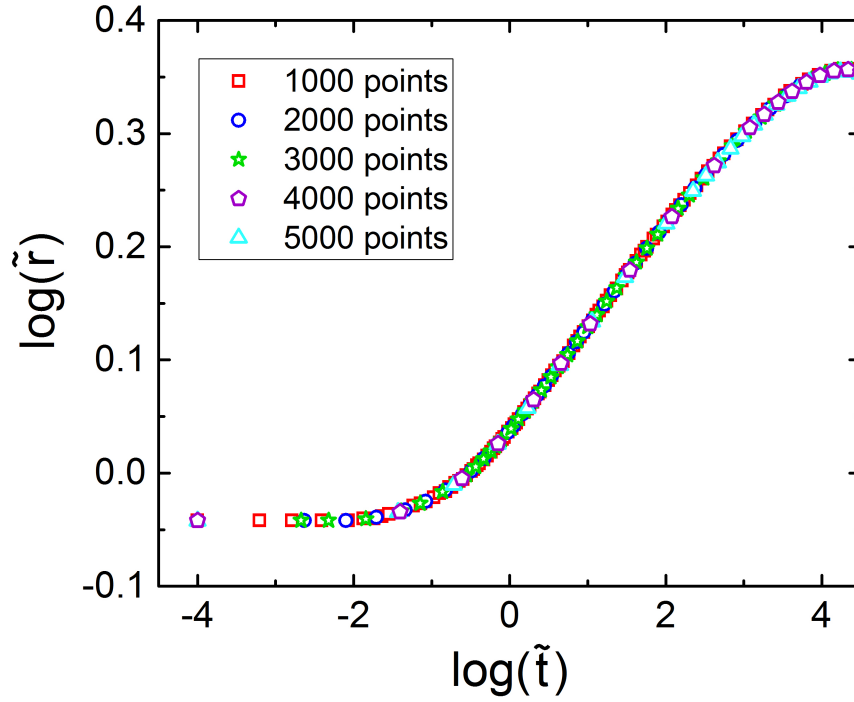Figure B-1: The logarithmic dependence of droplet radius with time for different number of grid points.
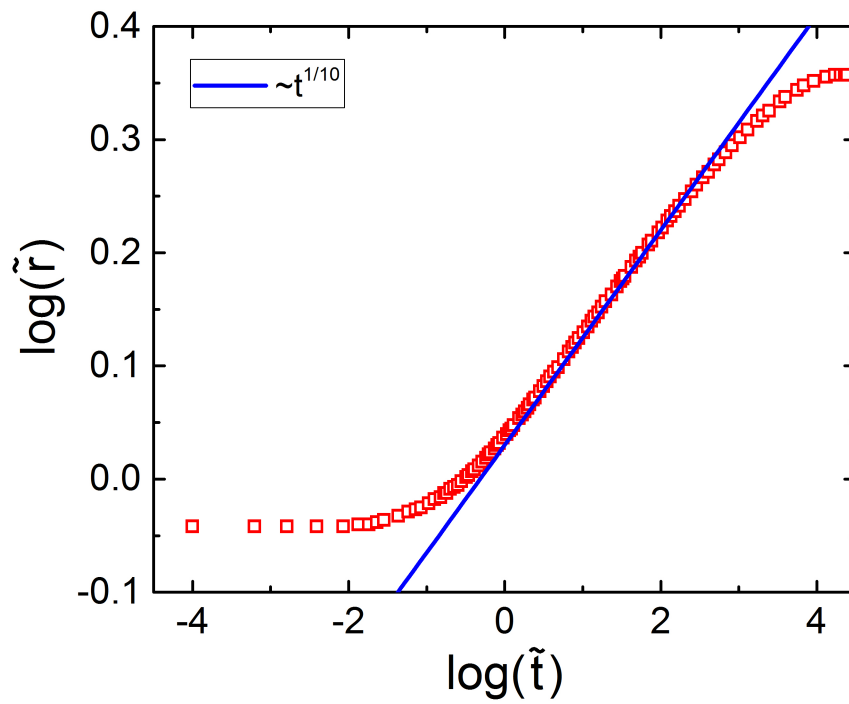
C-1   Validation of the numerical code

Figure C-2: Validation of the numerical code with Tanner's law [4]($r \sim t^{0.1}$).